UNIVERSITY OF OKLAHOMA

GRADUATE COLLEGE

OBSERVATIONS AND SIMULATIONS OF MOISTURE CHANGES OCCURRING AROUND SUNSET AT THE ARM CLIMATE RESEARCH FACILITY

A DISSERTATION

SUBMITTED TO THE GRADUATE FACULTY

in partial fulfillment of the requirements for the

Degree of

DOCTOR OF PHILOSOPHY

By

WILLIAM G. BLUMBERG
Norman, Oklahoma
2018

OBSERVATIONS AND SIMULATIONS OF MOISTURE CHANGES OCCURRING AROUND SUNSET AT THE ARM CLIMATE RESEARCH FACILITY

A DISSERTATION APPROVED FOR THE
SCHOOL OF METEOROLOGY

BY

Dr. Steven Cavallo, Chair

Dr. David D. Turner, Co-Chair

Dr. Jeff Basara

Dr. Alan Shapiro

Dr. Andrew Fagg

Acknowledgements

While I could spend pages explaining my thanks to the various individuals who have helped me get to where I am today, I will have to refer you, the reader to my Master's thesis acknowledgements. Many important people are listed there. If I forget you here, I ask for your forgiveness. I am only human. But if you care enough to ask about how you helped, I will strive to tell you how you came to nourish my invisible essential.

First, I'd like to thank my committee for their guidance, patience, and support over the past four years. Finding my way throughout this process was difficult and long, and I am grateful for your constant encouragement and advice. Steven Cavallo's lessons in the proposal and scientific process was invaluable to my understanding of what is expected from a scientist. Steven also took up the mantle of being my regular in-person contact when Dave Turner needed to make a move to support his family. I appreciate the constant encouragement and discussions about synoptic meteorology, the land-surface, and teaching strategies with Jeff Basara. The challenges issued by Alan Shapiro throughout my research forced me to reach deeply into my mental bag of datasets, and for that I now have a much more diverse tool set to answer problems than I did when I started. He still needs to write a recipe book. Lastly, Dave Turner has provided me with nearly seven years of patient and supportive guidance that is branded into my mind forever. I'm not sure I could have found a better match for an advisor if I tried. Your efforts have made me a more capable scientist who can

now ask focused science questions, make contributions to the science, and recognize places for growth in myself and others. Thank you for watching out for me, especially at the end of this journey!

There are a number of other individuals who have helped me either by providing resources for this dissertation and/or intellectual guidance. These include Jidong Gao for providing his 2D-VAR code and Patrick Skinner for his discussions on the NEWS-e model and how this research can be used in the context of the Warn-on-Forecast project. For their contributions towards the SHARPpy project, I must thank the talented minds at SPC: Patrick Marsh, Rich Thompson, John Hart, Ryan Jewell, and Bryan Smith. Much appreciation goes to Ariel Cohen for his efforts to bring an exciting class to SoM students and his insight on the challenges inherent in the operational community. The students and scientists within the BLISS and AAARG groups also provided a variety of insights for me into the scientific process. Daphne LaDue provided regular encouragement and support throughout the whole process. I also extend a thanks to Tim Wagner, Tim Bonin, Jimmy Correia Jr., Jason Knievel, and Stan Trier. Tim Wagner provided extensive guidance on all aspects of life and academia, and I am grateful for his friendship, our lively conversations, and the fun we've had exploring the Plains. Tim Bonin's 2015 paper gave me the foundation to pass my general exam, and for that I am indebted to his contribution to the science. Jimmy's incredible talent for generating fantastic ideas for meteorologists showed up time and time again in our conversations, and serves as an inspiration to many students, myself included. Lastly, I must thank Stan Trier and Jason Knievel for our conversations in San Diego during the summer 2017 AMS Mesoscale Conference. Stan's perspective on how observations and numerical simulations can be used to further scientific knowledge was invaluable in

balancing this observation-heavy scientist. Jason's conversation with me helped start the process of writing this dissertation when the phrase "starting to write" seemed too abstract and daunting.

I also must thank the support and administrative staff from the ARM, NSSL, SoM and CIMMS organizations. Christine Reed was an invaluable resource for solving the various problems that arose during my research and teaching. I also must include the IT professionals of the ARM, SoM, and NSSL organizations who helped me with the numerous difficulties I had with computer systems. Special thanks also go to the CIMMS, SoM, and NSSL administrative staff, who numerous times patiently helped this young, ADHD scientist get the proper paperwork in. The fine folks at CIMMS supported my research for three years of my PhD and helped fund both the various journal articles and research that came from my work. I am grateful for that opportunity.

I often learn by teaching, and there are three individuals who have graciously let me pass on the wisdom I have learned during this process. First, I acknowledge Kelton Halbert (and his family), who consistently encouraged me throughout this process and had the inspiration to pick up the SHARPpy project, which ended up being a career defining moment for us. I am proud of the person you have become and the ideals you defend. Second, Matthew Bolton. Your work on disabilities and weather has really taken off, and I am thrilled to have been a co-instigator for what is a significant portion of your career. Lastly, Sean Ernst for his friendship, insight, and stunningly persuasive arguments for why I should let a stray cat into my life. While there were certainly times I wanted to strangle my cat, his presence gave me a fun new hobby and kept the apartment from becoming too lonely while I puttered away writing this dissertation. These three people poured back into me their own

perspective and knowledge, and I am proud to have them as colleagues, students, and friends. I cannot wait to see what more they do in the future. I should especially mention the 2018 spring METR 2011 lab class. They helped keep my sanity in the final stages of writing by giving me an outlet for my desire to challenge students in new and inspirational ways.

I cannot end these acknowledgements without thanking many of my friends who supported me in more ways than I can count. I want to especially point out my close friends and neighbors Andrew Mackenzie, Tim Supinie, Heather Supinie, DJ Gagne, and Cathy Bolene. They consistently provided thoughtful and care-filled guidance in both the professional and personal aspects of my life. You are a key part of my roots in Norman, and I cherish the incredible adventures we have gone on. I am thankful for the friendship of Nathan Dahl, Brittany Dahl, and Burkely Gallo. Those who have left Norman have also provided much joy, such as Bryan Trachier, Jason Godwin, Andrew Ryan, Curtis Riganti, and Charlotte Lunday. My Maryland friends were especially important in providing me fun and laughter outside of world of meteorology. These people include Nick Quizon, Simon Shtipelman, Sasha Kotliarova, Mike Dowdy, and Gioia Mia. You all have been supportive through the ups and downs of this process. I'm not sure where I'd be without that.

Finally, I need to thank my family. My parents, sisters, cousins, and grandparents were key to my success. You loved me into being when I was little and that continues to this day. My parents, Mark and Traci were always there for me and helped listen to my frustrations. My sisters, Rachel and Sarah were also there for me in more ways than one, and their loving relationship and quirky personalities gave me many much needed laughs. My trips down to Fort Worth to see my relatives and their families allowed me to decompress many times. My

grandmother, Martha Blumberg cheered me on (sometimes anxiously) at every single milestone of this journey. She and my grandfather, Bill Anderle (and Lyn) were an inspiration for much of this journey with their individual stories of severe weather in north Texas. I'd like to mention my cousins Gabrielle, Joe, Aaron, and Amber and their kids: Will, Raye, Abby, Ava, and Adalyn as they also helped me have fun and remember what it's like to be a kid. Thank you all for helping me step away from the work regularly whether through late night movies, trips overseas, or just a phone call. Your support was never failing, and I will appreciate that more and more as I step away from this chapter of my life.

Table of Contents

Acknowledgements **iv**

List Of Tables **xi**

List Of Figures **xiii**

Abstract **xxi**

1 Introduction **1**

2 Background **6**
2.1 Overview of Ingredients Present during the AET 7
2.2 Studies on Moisture Changes During the AET 11
2.3 Turbulence Decay during the AET 15

3 Research Questions and Hypotheses **18**

4 ARM Instrumentation, Algorithms, and Simulations **22**
4.1 Surface-Based In-Situ Observations 26
4.1.1 Surface MET 26
4.1.2 ECOR and EBBR Systems 26
4.1.3 Sky Type Detection 30
4.2 Remote Sensors 31
4.2.1 Microwave Radiometers 32
4.2.2 The Atmospheric Emitted Radiance Interferometer . . . 35
4.2.3 Raman Lidar 36
4.2.4 Doppler Lidar 40
4.3 Retrieval Algorithms 42
4.3.1 Optimal Estimation 43
4.4 LASSO 45
4.4.1 Simulation Forcing Datasets 48

5 Verification of AERIoe Retrievals **52**
5.1 Retrieval Accuracy and Information Content 55
5.2 Verification of AERIoe Convection Indices 63
5.2.1 SHARPpy 64
5.2.2 Comparison of Convection Indices 66
5.2.3 Uncertainty of Convection Indices 69

6 Lateral Evolution of Moisture **75**
6.1 The Oklahoma Mesonet 76
6.2 2D-VAR 80
6.3 Monthly Changes in Moisture 85
6.4 Spatial Changes in Moisture 87
6.5 Analysis of AET q_v Maxima 95

7 Vertical Evolution of Moisture **109**
7.1 AET Cases from ARM Site 110
7.2 Identifying the Evening Transition 113
7.3 AET Example Cases 116
7.4 Composite Plots and Discussion 128

8 Processes Affecting Moisture during the AET **135**
8.1 Experiment Setup and Methods 138
8.2 Gradients in q_v and Momentum Across the WWB Border 143
8.3 Profiles of q_v Advection 149
8.4 LES Results 151
8.5 SGP Summer AET Conceptual Model 160

9 Conclusions and Future Work **165**
9.1 Future Work 169

Reference List **174**

Appendix: Glossary **198**

List Of Tables

2.1 Chronological list of studies found during the literature review on deep, moist convection and the Afternoon to Evening Transition (AET). Each study is categorized by which ingredients for convection they focus on. 9

4.1 A summary of the surface-based, in-situ observations used in this study. Δt represents the temporal sampling frequency, while z indicates the height of the observation. For each Atmospheric Radiation Measurement (ARM) dataset used, a reference is included to the ARM documentation. 27

4.2 Active (A) and passive (P) remote sensing instruments used in this study. λ_R and λ_T correspond to the instrument receiver and transmitter wavelengths. Δt and Δz are the temporal sampling frequency and the vertical grid spacing from the profiling instruments. The final column indicates the variables retrieved from each instrument. 33

4.3 The LES ARM Symbiotic Simulation and Observation (LASSO) model suite configuration. In the large-scale forcing and microphysics categories the various options for the runs are listed. . . 49

5.1 Observations utilized in the Atmospheric Emitted Radiance Interfereometer (AERI)oe $\mathbf{y}$ vector for this study. The noise values for the AERI channels are listed in (Turner and Löhnert 2014; Blumberg et al. 2015). 1-σ errors for the Raman lidar are derived directly from Poisson statistics from the detected photon counts. 54

5.2 The verification statistics for different median thermodynamic indices: convective inhibition (CIN) (J/kg), convective available potential energy (CAPE) (J/kg), B_{min} (°C), LI_5 (°C), and B_{min} height (km). Shown are the number of data points n, bias, 1-σ standard deviation (STD) of the error, and the Normalized STD (NSTD). NSTD is the ratio of STD to the 1-sigma STD calculated using all the radiosonde indices for that index. Only profiles where the radiosonde parcel being evaluated had a $CAPE > 100$ J/kg and a $CIN > -800$ J/kg were used in the CIN comparisons to ensure that the radiosonde had a nonzero value of CIN and CAPE. Caption is reproduced from Blumberg et al. (2017b). . . 68

6.1 Variables reported by the Oklahoma Mesonet instruments by height z. The errors column represents the $1-\sigma$ errors for the 5-minute observations. Soil moisture is reported every 30 minutes. 77
6.2 Total number of AET cases available for analysis in each Winter Wheat Belt (WWB)-relative category. 103

7.1 The 31 individual cases analyzed from data collected at the Southern Great Plains (SGP) ARM site. Δq_v is the size of the jump over time in g/kg and was estimated from the surface-met time series. The depth Δz of the q_v jump is listed in km and was estimated from the AERIoe retrievals. The start time of the jump (t_{start}), the end time (t_{end}) and the evening transition (ET) time (t_{ET}) are listed in hours relative to local sunset. The last column represents the tendency in water vapor using Δq_v and $\Delta t = t_{end} - t_{start}$. The final rows represents the average (μ) and 1-σ standard deviation of the data in the columns. 111

8.1 The configuration of each member of the 12-member System for Atmospheric Modeling (SAM) ensemble used in analyzing the 8-18-2016 and 7-20-2016 cases. The columns indicate the member ID number, the model core, the dataset for the large-scale forcing, the scale of the large-scale forcing, the surface forcing dataset, and the microphysics package. Asterisks indicate the multi-scale data assimilation (MSDA) forcing dataset that included the assimilation of the ARM RWP wind profiles. 153

List Of Figures

1.1 An isolated supercell thunderstorm in southwestern Oklahoma around sunset on March 30, 2008. Throughout the supercell's life cycle, the author observed a significant intensification of the storm's inflow beginning around sunset and continuing into the nighttime hours. 3

1.2 The various time frames that encompass the afternoon-to-evening transition time period applied to a time series of sensible heat flux obtained in Northern Oklahoma at the ARM SGP Central Facility (36° 36′ 18″ N, 97° 29′ 6″ W). The figure starts at 2017-06-17 12 UTC and ends on 2017-06-18 05 UTC. 6 o'clock local time occurs at 23 UTC, at the beginning of the AET. 4

4.1 A map of the ARM Central Facility site and the location of the key ARM instruments used in this dissertation. Image provided by Dave Turner. 25

4.2 Bias (solid line) and 1-σ standard deviation (dashed line) of Raman lidar (RLID) derived temperature (A, n=144) profiles and water vapor mixing ratio (B, n=287) profiles. 40

5.1 Sample AERI spectra from Blumberg et al. (2017b) with portions of the spectra used in the AERIoe retrieval highlighted in orange, green, and red colors. (b) The residuals between the observed AERI spectra and the spectra calculated using the LBLRTM for a sample retrieved profile. The red lines in (b) indicate the AERI $1-\sigma$ observational error assumed in AERIoe. Here, 1 RU = 1 $mW\,/\,(m^2\,sr\,cm^{-1})$ 54

5.2 Plots showing the cumulative degrees of freedom of signal (DFS) on the left and the vertical resolution (right) from the AERIoe-retrievals. Blue indicates the statistics for the water vapor profile, while the red indicates the statistics for the temperature profile. The shaded area indicates the 25-75th percentile of the statistic, and the solid line represents the median value (n=182). 56

5.3 Bias (solid) and standard deviation (dashed; STD) for AERIoe-retrieved temperature (red) and water vapor (blue) compared to the profiles obtained from co-located radiosonde launches (n=182). 57

5.4 Bias (solid) and standard deviation (dashed) for profiles input into AERIoe. The profiles included are the Raman lidar water vapor profile (green), the Raman lidar temperature profile (red), and the RAP temperature profile (magenta) (n=182). 58

5.5 A comparison between precipitable water vapor (PWV) derived from radiosondes (PWV_{RAOB}) and MWRRET PWV_{MWRRET}. Plots A and B are the difference and the percent error for the two PWV estimates, respectively. Each point indicates a 23 UTC RAOB and MWRRET comparison. The x-axis indicates the difference between the RAOB and MWRRET PWV values. (n=350). 59
5.6 Taylor plots for the AERIoe-retrieved temperature (red) and water vapor (blue) compared to the profiles obtained from co-located radiosonde launches. Portions of the vertical profile used in this analysis are between the surface and 2 km AGL (n=182). 62
5.7 An example of the different lifting routines in SHARPpy. The profile is from the ARM site and was launched on May 20th, 2013 at 11:31 UTC. Red represents the temperature trace, green the dewpoint trace, and dashed red the virtual temperature trace. In the legend are the different parcel traces (RDJ; Davies-Jones (2008) and WOBUS; Doswell (1987)) along with the speed in seconds. 71
5.8 Error plots for thermodynamic indices (a, f, k) CAPE (J/kg), (b, g, l) CIN (J/kg), (c, h, m) B_{min} (°C), (d, i, n) LI_5 (°C), and (e, j, o) B_{min} height (km) for the (top) SB, (middle) ML, and (bottom) MU parcels. The y-axis represents the difference between the AERI and radiosonde index, while the x-axis represents AERI index value. Individual points indicate a single AERI-radiosonde comparison. The light gray shading in these plots represents the area where invalid bias values exist because of a lower or upper bound on the range of valid index values (for example, CAPE is nonnegative) (n=231). 72
5.9 The impact of instrument random error on the calculation of the $CAPE$, CIN, B_{min}, and LI_5 indices using (a)–(d) AERI and (e)–(h) radiosonde profiles with $CAPE > 250$ (J/kg). The IQR of the index distribution is on the y axis, while the median value of the index is on the x axis. The points are colored by the type of parcel used to calculate the index (MU parcel: blue; ML parcel: red; SB parcel: yellow). Thick lines indicate the line of best fit to qualitatively show the trends for illustration purposes. Caption and figure are reproduced from Blumberg et al. (2017b). 73
5.10 An comparison of the correlation matrices derived from the error covariance matrices for the AERIoe retrieval (left) and a co-located radiosonde (right). 74

6.1 Distribution of AET cases from the Oklahoma Mesonet between 1994-2014 (n=3822). 78

6.2 The AET cloud classification algorithm using the Oklahoma Mesonet SRAD variable showing the thresholds for clear (blue), scattered (green), and overcast (red) for the months of March-August. Average difference between the daytime theoretical and observed insolation is on the x-axis while the natural logarithm of the standard deviation of those differences is on the y-axis. 80
6.3 A map of the Oklahoma Mesonet observations (black points), the Delaunay triangulation using those data points (black lines), the gradient observations (blue dots), and the 2D-VAR grid (red lines) using a grid spacing of $\Delta x = 12$ km. 82
6.4 Figures showing the dependency of 2D-VAR accuracy on the Ψ parameter. The accuracy is measured by computing the 1-sigma standard deviation using the difference between the truth grid and the analyzed 2D-VAR grid. The top plot shows the accuracy for the q_v scalar field, the middle plot for the horizontal gradient of q_v, and the bottom plot for the water vapor advection. The thick line indicates the median standard deviation, while the thinner lines indicates the 25th to 75th percentile of the standard deviation metric. 84
6.5 This distribution of changes of water vapor relative to the value three hours prior to sunset (Δq_v) for the Medford, OK Mesonet station. The distribution is identified by the red lines (the median), the orange lines (the 25-75 percentile) and the black lines (the 10-90th percentiles). Data is also broken up by month to illustrate how the distribution changes with the season with spring months in the left column and summer months on the right. . . 86
6.6 Monthly averages of Moderate Resolution Imaging Spectroradiometer (MODIS)-derived Normalized Difference Vegetation Index (NDVI) for Oklahoma and the Texas Panhandle from 2007 for the months of March through August. Black lines indicate the boundaries of the WWB from McPherson et al. (2004). . . . 89
6.7 Spatial changes in moisture relative to the moisture value 3-hours prior to sunset using March 2D-VAR analyses (n=503; 1998-2014). Rows correspond to the 25th, 50th, and 75th percentile changes of the water vapor, while columns refer to the time of the map in sunset relative time (SRT). The black lines indicate the outline of the winter wheat belt from McPherson et al. (2004). 90
6.8 Similar to Figure 6.7, but using April analyses (n=503; 1998-2014). 91
6.9 Similar to Figure 6.7, but using May analyses (n=540; 1998-2014). 92
6.10 Similar to Figure 6.7, but using June analyses (n=522; 1998-2014). 93
6.11 Similar to Figure 6.7, but using July analyses (n=510; 1998-2014). 93
6.12 Similar to Figure 6.7, but using August analyses (n=510; 1998-2014). 94

6.13 Groups of Mesonet sites relative to the winter wheat belt (WWB) used in McPherson et al. (2004). W-WWB and E-WWB refer to the sites west (blue) and east (red) of the WWB (green). The outline of the WWB from McPherson et al. (2004) is included in the map in the dark black outline. 96
6.14 Bootstrapped probability density functions describing when q_v typically reaches a maxima in the AET time period. Individual panels show the PDFs of WWB-relative group for the months of March through August. The three thick lines indicate the mean PDFs for each group and follow the coloring scheme outlined in Figure 6.13 where blue is W-WWB sites, red is E-WWB sites, and green is WWB sites. Shading represents the 95% confidence intervals calculated via bootstrapping. 104
6.15 Similar to Figure 6.14, but for the 500-mb lifted index LI_5. . . . 105
6.16 Similar to Figure 6.14, but for the surface virtual temperature T_v. 106
6.17 Plots illustrating how the probability of a q_v maxima prior to sunset is dependent upon fractional water index (FWI), time of year, and WWB-region. Solid lines depict the probability of the q_v maximum occurring within an hour and a half prior to sunset. Each panel indicates a WWB-region and the x-axis indicates each month. Blue indicates the category where the $FWI > 0.85$ while red indicates the category when $FWI < 0.85$. Error bars indicate the 95% confidence interval (CI) of those probabilities, computed by bootstrapping. Green dots indicate months where differences between the two distributions are statistically significant at the 95% CI. The dashed lines indicates the number of samples available for bootstrapping, while the horizontal solid gray line indicates the minimum number of samples for bootstrapping (500). 107
6.18 Similar to Figure 6.17, but for the dependency on surface wind instead of FWI. Red indicates cases where the average surface wind was less than 5 m/s, while blue were cases when the average surface wind was greater than 5 m/s. 107
6.19 Similar to Figure 6.14, but with two exceptions. First, the PDFs shown are only using AET cases from the WWB category. Second, instead of WWB categories, the colors correspond to different cloud cover categories from the cloud detection algorithm described in Section 6.1. For the different PDFs, magenta indicates clear skies, orange indicates scattered skies, and green indicates cloudy skies. 108

7.1 A comparison of the times of the evening transition (ET) relative to sunset observed by the ECOR and EBBR instruments for the 31 cases described in Table 7.1. Individual points are colored by the value of the meridional wind measured by the ECOR at the time of the ECOR's ET. 114
7.2 Time by height cross sections showing the evolution of water vapor mixing ratio from the AERIoe retrievals of the first six cases in Table 7.1. The vertical solid and dashed lines indicate the time of the ET and sunset, respectively. The y-axis is height above ground level and the x-axis is in sunset relative time, with 0 being the local sunset time (SRT). In the top left of each plot indicates the time of the afternoon transition (afternoon transition (AT)) and the evening transition (ET) in hours sunset relative time (SRT). 115
7.3 As in Figure 7.2, but for vertical velocity variance ($\overline{w'^2}$) from the Doppler lidar (DLID). The black contours indicate lines of constant mixing ratio (every 1 g/kg) from AERIoe smoothed by a 2D Gaussian smoother ($\sigma = 1.5$) to illustrate the moisture evolution relative to the turbulence decay. The topmost contour in each plot indicates the 8 g/kg line. $\overline{w'^2}$ is only shown if the signal to noise ratio is above 1 $m^2\,s^{-2}$ 122
7.4 As in Figure 7.3, but for the meridional wind obtained from the DLID. 123
7.5 As in Figure 7.3, but for the zonal wind obtained from the DLID. 124
7.6 As in Figure 7.3, but for CAPE computed by lifting the parcels from every data point in the profile. Places where no contours exist (white) indicates absolutely stable parcels. 125
7.7 The difference between observed CAPE (Figure 7.6) and CAPE computed holding the water vapor profile 5 hours prior to sunset constant throughout the next 8 hours. Green indicates locations where changes in q_v contributed to an increase in CAPE despite changes to the temperature profile. 126
7.8 As in Figure 7.6, but for CIN. 127

7.9 Composite plots showing the average evolution of variables during the AET using the 31 AET cases listed in Table 7.1. A and B indicate the potential temperature and q_v profiles from the AERIoe retrievals. C and D show the zonal and meridional winds from the DLID. E and F show the variance and skewness of vertical velocity from the DLID. Skewness is reported as unitless from the DLID. G and H show the average sensible and latent heat fluxes from the ECOR dataset and the bulk wind difference (BWD) between 0 and 500-m from the MET and DLID wind observations. 133
7.10 Similar to Figure 7.9 but showing the average evolution of CAPE and CIN (A, B), and the average evolution of CAPE and CIN assuming that the water vapor profile at the beginning of the observed period (-5 hours prior to sunset) did not change for the entire 8 hour period shown (C, D). 134

8.1 Composite 2D-VAR analyses from the Oklahoma Mesonet data (Chapter 6) showing how the distribution of moisture advection and moisture gradient magnitudes evolve throughout May AETs in Oklahoma. The top and middle rows indicate the 75% and 25% percentiles of moisture advection, respectively. The bottom row shows the median moisture gradient magnitude. The columns indicate time in sunset relative time (SRT) and the bold black lines denote the boundaries of the WWB. 137
8.2 Similar to Figure 8.1, but for the month of June. 138
8.3 Selected ARM observation sites used in understanding the processes relevant to q_v jumps occurring in the 2016-2017 SGP dataset analyzed in the last chapter. C1 indicates the location of the ARM SGP Central Facility, while E37, E32, and E39 are the ARM extended facilities surrounding the C1 site. Black arrows and distances indicate the distances calculated between the different sites. These site locations are overlaid on the MODIS Rolling Average 8-Day NDVI dataset for May 31st, 2017 to illustrate the distribution of the sites relative to healthy vegetation and the eastern WWB boundary. The boundaries of the WWB can be roughly found in Figure 6.6. 142
8.4 The 850-mb wind speed and zonal component wind speed for the 33 summertime cases. Each point represents the wind observed from the 23 UTC radiosonde launched during each case. 144

8.5 Two plots denoting the average wind and moisture conditions across the WWB using 31 cases from the summertime. The top plot shows the average C1 wind component tangent (v_{C1-E39}) to the C1-E39 WWB cross section while the bottom plot shows the average horizontal q_v gradient ($\nabla_h q_v$). Hatching on the lower plot indicates the times and heights when the $1 - \sigma\ \nabla_h q_v$ indicates a positive value across the WWB, suggesting that the distribution of $\nabla_h q_v$ is shifted towards positive values at these times. 147
8.6 Estimates of the water vapor advection term at the C1 site generated by combining various average estimates of ∇q_v and v_{C1-E39} from Figure 8.5. 148
8.7 Average q_v advection from the same 31 cases used in Figure 8.5. Advection was calculated using the C1-E39-E37 triangle and Equation 8.1. 151
8.8 A map of the Southern Great Plains area with various sizes representing the large-scale forcing of the area. All forcing areas are centered around the ARM SGP Central Facility site. Solid black contours denote the boundaries of the WWB from McPherson et al. (2004). 154
8.9 Horizontal q_v large-scale advection from the six forcing datasets used in the LASSO ensemble. The forcing shown is for the 2016-08-18 LASSO runs. The top two rows indicate the MSDA 150 and 75 km forcing with and without the ARM RWP data assimilated. The bottom row is the European Center for Mid-Range Forecasts (ECMWF) 114 and 16 km forcing. 155
8.10 Similar to Figure 8.9, but for the 2016-07-20 case. 156
8.11 Average contributions from the local tendency of water vapor (1st row) the turbulent moisture flux convergence (2nd row), large-scale vertical advection (3rd row), and large-scale horizontal advection (4th row) for the two cases (08-18-2016, left) and (07-20-2016, right) using the SAM ensemble. The local tendency of q_v is computed by performing finite differencing on the 10-minute q_v output (forward and backwards near the edges, central everywhere else.) 159
8.12 The evolution of the horizontal cross section from the ARM E32-C1-E39 sites for the 8-18-2016 case during the surge in moisture across the WWB. The left column indicates the q_v profile, while the right indicates the CAPE profile. Arrows in the CAPE plot indicates the cross-WWB wind vector at the C1 and E39 sites. From top to bottom the time of the cross sections moves from 00:20 to 1:00 to 1:30 UTC. Black indicates the ground. 163

8.13 An illustration showing the cross section along the WWB between the ARM sites C1 and E39 and how turbulence, winds, and moisture change before (left) and during the AET (right). The bottom table shows the sign of the relevant terms of the moisture tendency equation and their second derivatives in both stages. The blue circulation over the WWB represents the mixing ongoing throughout the day (left) and reduced mixing later on (right). The length of the black arrow indicates the wind speed along the WWB cross section, which accelerates per Figure 8.5. z_i indicates the convective boundary layer (CBL) top which varies across the WWB per McPherson and Stensrud (2005). 164

9.1 Geographical locations of where winter wheat is grown in the United States. Data used for this map is constructed using the National Agriculture Statistics Service, and the map was constructed by the U.S. Department of Agriculture. Image URL: https://www.usda.gov/media/blog/2013/03/7/usda-releases-new-maps-identifying-major-crop-producing-areas-united-states . . . 172

Abstract

Each summer, the U.S. Southern Great Plains hosts a variety of ingredients (e.g. moisture, shear, instability, and lift) critical to understanding the life-cycle of deep, moist convection. Past studies have primarily shown that two ingredients undergo substantial changes in the evening hours: shear and instability. While increases in low-level static stability may act to inhibit deep convection, increases in low-level shear may promote the maintenance of convective updrafts. Consideration of only a subset of these ingredients presents an incomplete conceptual model of local, low-level environmental changes that occur during the Afternoon-to-Evening Transition (AET). As various studies of the SGP indicate that the frequency of hazardous thunderstorms begins to increase in the evening hours, consideration of how other ingredients evolve may facilitate additional improvements to convective forecasts.

To improve this conceptual model, a new line of research aims to track the spatiotemporal evolution of water vapor during the SGP AET and understand the processes behind these changes. By using data produced by the Oklahoma Mesonet and Atmospheric Radiation Measurement (ARM) programs, rapid increases (1-4 g/kg) in moisture are found to occur near the SGP Winter Wheat Belt (WWB). In some cases, these jumps in moisture can greatly reverse the loss of conditional instability caused by the setting sun. By using a combined observation and modeling strategy, this study helps clarify the relationships between decaying turbulence and moisture advection on moisture and conditional

instability. The results from this study lends support to a conceptual model that in the summertime, the processes occurring during the AET initiate a westward surge in moisture from the eastern boundary of the WWB that may intensify deep, moist convection downstream.

Chapter 1

Introduction

To atmospheric scientists, any mass within an atmosphere that can potentially change phase presents a challenging problem. Thankfully, only one gas in Earth's atmosphere regularly changes phase: water. Although water sustains life on Earth, it does so with a violent streak. Most notably, water facilitates the rapid vertical exchange of air in the atmosphere we call thunderstorms. Water plays a key role in this phenomenon. When ascending, the conversion of water vapor into liquid water (or ice crystals) within the air may cause a stunning show of lightning. When descending, the evaporation of water droplets can accelerate air downwards, causing damaging winds at the surface. Regardless of whether the air goes up or down, water is the driving force behind this exchange.

Thunderstorms have a significant impact upon human lives though a variety of potential threats (e.g., high winds, hail, heavy rain, tornadoes, and lightning). Without proper awareness and preparedness, thunderstorms can cause injuries and fatalities, especially in places where the population density is high, such as stadiums or amusement parks (Gratz and Noble 2006; Edwards and Lemon 2002). Thunderstorms can also make people sick. Allergists have found that high winds produced by thunderstorms can loft fungi and pollen into the air and cause asthma outbreaks (Nasser and Pulimood 2009). This vulnerability is troubling as climate predictions suggest that the frequency of severe thunderstorms will increase in the future in response to anthropogenic climate change

(Diffenbaugh et al. 2013; Trapp et al. 2007; Brooks 2013). Because of future projections and their societal relevance, it is imperative that scientists study the origins and evolution of thunderstorms.

Observations by various atmospheric scientists and storm-chasers have noted that the likelihood of thunderstorm formation and intensification increases near sunset (Figure 1.1). Maddox (1993) wrote: "It is observed by storm chasers, whose activities tend to be confined to the open spaces of the Plains states, that poorly organized storms occasionally change markedly around sunset, with supercell events developing during the evening to early nighttime hours." This phenomenon has colloquially been referred to as "6 o'clock magic." The term "6 o'clock magic" was first formally introduced to the scientific literature in Bosart and Bluestein (2008) and Bluestein (2015). They have referred to this phenomena as "the apparent increase in the likelihood of storm formation and the formation of tornadoes beginning at 6 PM local time."

Although the causes behind the 6 o'clock magic theory have not been proven rigorously using observations (Bluestein et al. 2017), studies reinforce these anecdotal observations. Hocker and Basara (2008) demonstrated in a 10-year climatology that, supercells most commonly develop in Oklahoma around 23 UTC. Anderson-Frey et al. (2016) and Mead and Thompson (2011) further demonstrate that the likelihood of significant tornadoes (EF2+) begins to increase around sunset. In the Great Plains region of the United States, numerous thunderstorm climatologies have indicated that the evening hours denote the beginning of an increase in thunderstorm related hazards such as tornadoes, lightning, and heavy precipitation (Means 1944; Wallace 1975; Orville 1981; Balling Jr 1985; Mead and Thompson 2011).

Figure 1.1: An isolated supercell thunderstorm in southwestern Oklahoma around sunset on March 30, 2008. Throughout the supercell's life cycle, the author observed a significant intensification of the storm's inflow beginning around sunset and continuing into the nighttime hours.

The name of the field of research that encompasses the time period around sunset varies across the literature. Some papers refer to this period as the AET (e.g. Busse and Knupp 2012; Wingo and Knupp 2015), while others refer to it as the early-evening transition (EET, e.g. Bonin et al. 2013; Coffer and Parker 2015). The exact time frame that these two acronyms define is difficult to ascertain from the literature, and the measurements available in past studies often dictate how to identify this time period. Lothon et al. (2014) formally made the distinction between the afternoon transition (AT) and the evening transition (ET) via the sensible heat flux. The former can be identified by

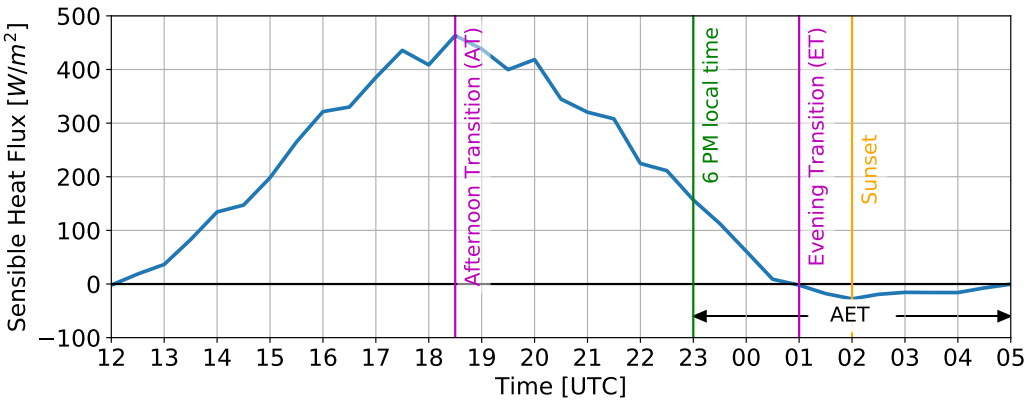

Figure 1.2: The various time frames that encompass the afternoon-to-evening transition time period applied to a time series of sensible heat flux obtained in Northern Oklahoma at the ARM SGP Central Facility (36° 36′ 18″ N, 97° 29′ 6″ W). The figure starts at 2017-06-17 12 UTC and ends on 2017-06-18 05 UTC. 6 o'clock local time occurs at 23 UTC, at the beginning of the AET.

finding the time when the sensible heat flux is at a maximum during the day, while the latter can be found by identifying the time in the evening when the sensible heat flux sign reverses. In this research, the terms of AET, AT, and ET defined in Wingo and Knupp (2015) and Lothon et al. (2014) are used, and their definitions are illustrated in a time series of sensible heat flux in Figure 1.2. The AET in this study is defined as a time period encompassing the ET, which is roughly a six hour period centered on local, astronomical sunset. However the name, the rapid changes within this time frame are challenging to study as it is difficult to adequately sample the many atmospheric processes occurring.

As water vapor is a critical component to precipitation and thunderstorm development, it is important to be able to understand its evolution throughout the diurnal cycle. Given this fact and the results from previous studies describing an increase in thunderstorm activity in the evening hours of the Great Plains, a natural question arises. How does water vapor evolve during the evening hours of the Great Plains? This question is the central focus of this dissertation. In

the following chapter, past studies are discussed to help dissect this question and past work that has been done to address it. This discussion summarizes the current understanding of the various environmental changes that occur as the sun sets. Attention is also paid towards the various techniques used to study these changes and their impact on deep, moist convection. An understanding of this past work is important to understand the scientific context, direction taken, and results found during this study.

Chapter 2

Background

A primary way of understanding the causes behind deep, moist convection is through the lens of the "ingredients-based approach" (Doswell et al. 1996; Brooks 2007). In this framework, the scientific approach to anticipating a phenomena involves identifying the environmental ingredients for that phenomena and then focusing on the processes that change the spatiotemporal distribution of ingredients (Brooks 2007). In places where the ingredients are maximized, the probability of the phenomenon in question increases. Ingredients-based thinking forces the problem to be simplified to basic variables. For example, a primary ingredient for snowfall is identifying air that is below freezing, and is therefore linked to the variable of temperature (T) (Wetzel and Martin 2001).

For the problem of severe, deep, moist convection, four ingredients have been identified. Doswell et al. (1996) first proposed that the ingredients of moisture, lift, and instability were essential to the development of deep, moist convection. For the ingredients of moisture and lift, there must be 1.) enough moisture within a rising parcel that when lifted, the parcel reaches a level of free convection (LFC) and 2.) enough lift that the parcel can reach its LFC. Per parcel theory, the parcels lifted past their LFC can ascend due to temperature differences between the parcel and the environment (Doswell III and Markowski 2004). For the ingredient of instability, the environmental lapse rate ($\partial T/\partial z$) must support the existence of conditionally unstable parcels. The final ingredient, shear, acts

to organize and sustain convection (Brooks 2007). These four ingredients, lift, moisture, instability, and shear can be used to identify where convective development and intensification is more probable. Ingredients may be measured by various parameters, such as water vapor mixing ratio, environmental lapse rates, or storm-relative helicity. Although the individual ingredients may be related to one another through other various ways (e.g., steep lapse rates facilitating stronger rising motion per quasi-geostrophic theory), analyzing data for these ingredients is a useful first step towards diagnosing these relationships (Bluestein 1992).

2.1 Overview of Ingredients Present during the AET

Previous research about the AET can be divided into which ingredients they address and how those individual ingredients impact deep, moist convection (Table 2.1). A majority of the papers found during a literature search on these topics discuss changes in shear during the AET. During the late 1950s and most of the 1960s, scientists documented an increase in shear starting around sunset due to development of the Nocturnal Low-Level Jet (NLLJ) (Bonner 1968). To explain the mechanisms behind the formation of the NLLJ, Blackadar (1957) used dynamical equations to show how the loss of friction due to rapidly decaying turbulent eddies can create an low-level inertial oscillation that accelerates low-level winds. Holton (1967) also offered an explanation by demonstrating how diurnal increases in the low-level wind shear could also be created by imposing a diurnal heating cycle on sloped terrain. These two theories were recently merged in Shapiro et al. (2016). In the early 90s, Maddox (1993) published a paper making the connection between diurnal changes in shear due to

the development of the NLLJ and storm intensity. When the NLLJ develops, the hodograph enlarges, often in the shape of a sickle. This change, Maddox (1993) argued, can increase the low-level storm relative helicity to levels where tornadogenesis can become more likely. This hypothesis was further confirmed in Coffer and Parker (2015) in numerical simulations of supercells where the low-level wind shear was modified. These simulations showed how increases in low-level wind shear may intensify the low-level updraft and near-ground rotation strength despite increasing low-level static stability. The importance of the NLLJ in increasing the likelihood of nocturnal tornadoes has also been confirmed in the proximity sounding studies performed by Kis and Straka (2010) and Mead and Thompson (2011). Because the theories connecting low-level wind shear to supercell evolution are well established, many atmospheric scientists today widely attribute the changes storms undergo during the AET and nighttime hours to NLLJ-related increases in shear.

While increases in the NLLJ have been shown to intensify storms, stabilization of the boundary layer due to the loss of insolation can cause storm demise (Markowski and Richardson 2011). This process typically reduces the presence of near-surface, conditionally unstable parcels and studies have considered its impacts on storms compared to the NLLJ on supercells. Coffer and Parker (2015) showed that the NLLJ may prolong storm longevity despite low-level stabilization. Nowotarski et al. (2011) found that although supercells may not become elevated in statically stable layers, their near-surface circulations can become greatly reduced. Because of this result, they suggested that similar to Coffer and Parker (2015), the NLLJ may be essential for nocturnal tornadoes. Ziegler et al. (2010) showed how spatial variations of low-level static stability can

Table 2.1: Chronological list of studies found during the literature review on deep, moist convection and the AET. Each study is categorized by which ingredients for convection they focus on.

Paper	Instability	Moisture	Lift	Shear/NLLJ
Blackadar (1957)	-	-	-	X
Holton (1967)	-	-	-	X
Bonner (1968)	-	-	-	X
Blackadar (1979)	-	-	-	X
Fitzjarrald and Lala (1989)	-	X	-	-
Maddox (1993)	-	-	-	X
Mahrt et al. (1998)	-	X	-	-
Acevedo and Fitzjarrald (2001)	X	X	-	-
Jones and Bannon (2002)	X	X	X	-
Song et al. (2005)	-	-	-	X
Bosart and Bluestein (2008)	X	-	-	-
Kis and Straka (2010)	X	-	-	X
Mead and Thompson (2011)	X	X	-	X
Busse and Knupp (2012)	X	X	-	X
Parker (2014)	X	X	-	X
Coffer and Parker (2015)	X	-	-	X
Bluestein (2015)	X	-	-	X
Wingo and Knupp (2015)	X	X	X	X
Anderson-Frey et al. (2016)	X	-	-	X
Mahrt (2017)	X	-	-	-
Bluestein et al. (2017)	-	-	-	X

lead to a slow decay of supercells as the increasing stabilization may cause them to become more cold pool driven. Although most studies attribute stabilization to storm decay, it can be argued that these cooling trends may increase the chance of tornadogenesis, as increased boundary layer relative humidity may reduce evaporative cooling within downdrafts (Markowski et al. 2014). Generally though, the impacts of the diurnal cycle on conditional instability and boundary layer relative humidity are well understood (Ratnam et al. 2013).

Modeling stabilization during the AET often requires correctly representing the relative contributions of radiative and turbulent sensible heat flux divergence. From observations of the AET in Belford, England, Grant (1997) indicated that roughly half of the cooling in the low-levels can be attributed to turbulent flux divergence, while the other half is generally due to radiative flux divergence. While studies to improve radiative transfer calculations (e.g. Clough and Brown 1994) have improved our modeling of radiative contributions to the AET evolution, improvements to models of turbulence during the AET have been difficult to achieve. Blay-Carreras et al. (2014) and Jensen et al. (2016) both established that counter-gradient fluxes can occur for 30-40 minutes during the AET period, suggesting that using traditional flux-gradient relationships (Monin and Obukhov 1954) when modeling the AET may lead to errors in the timing of the transition. When constructing a generalized AET cooling conceptual model (e.g., rapid cooling surrounded by two periods of slower cooling), Mahrt (2017) suggested that variations in the speed of the cooling were primarily controlled by changes in the turbulent flux divergence. This conclusion is consistent with reasoning in Acevedo and Fitzjarrald (2001), a modeling and observation study of temperature and moisture in the AET. These studies show that while it is well-understood that stabilization of the boundary layer

helps destroy deep, moist convection, an understanding of the different roles flux divergence of radiation and turbulence play in stabilizing the boundary layer is still lacking.

2.2 Studies on Moisture Changes During the AET

Although many of these studies have established that changes to the ingredients of shear and instability during the AET contribute to changes in storm properties, alternative hypotheses considering moisture and lift has been the focus of less investigation. Changes in low-level lift were discovered in Jones and Bannon (2002), who used a mixed-layer model to simulate the dryline in the SGP. Solutions to their model indicated that a drastic increase in the inversion height east of the dryline develops at dusk due to entrainment and enhanced low-level convergence. They noted that this increase also occurred around the same time the dryline began to retreat westward. The hypothesis that the AET may create a maximum in low-level convergence was also discussed in Wingo and Knupp (2015). Their study documented steady increases in convergence above the surface layer occurring throughout the AET, and later showed that boundaries also exhibit an increase in convergence during the AET (Wingo 2015). These two studies lend support to the idea that increased lift could explain why convection initiation in the SGP tends to occur around sunset (Bosart and Bluestein 2008; Bluestein 2015).

With respect to moisture, Mead and Thompson (2011) found that nocturnal supercells that produce tornadoes tended to occur in environments with increasing planetary boundary layer (PBL) moisture that coincide with increases in low-level wind shear. In these scenarios, increases in PBL moisture helps

counteract the loss of CAPE and increase of CIN associated with the stabilizing boundary layer. In addition, increasing PBL moisture also serves to reduce evaporation within downdrafts, reducing the strength of cold pools and increasing the probability of tornadogenesis (Markowski et al. 2002; Markowski and Richardson 2014). Although these scenarios have occurred in past Southern Great Plains severe weather events (e.g. the Greensburg, KS nocturnal EF-5 tornado), there have been few studies investigating how rapid local increases in water vapor occur and how they impact conditional instability.

The presence of rapid increases in moisture during the AET has been documented by other researchers, however the focus of this research has primarily been outside the Southern Great Plains. Flower (1937) was the first to identify a rapid increase in water vapor (q_v) around sunset during a field experiment in Egypt. Further knowledge of this phenomena was developed by Fitzjarrald and Lala (1989) and Acevedo and Fitzjarrald (2001). They documented similar jumps in the near-surface water vapor content of roughly 1-3 g/kg in the Hudson Valley and offered explanations of their origin using the Reynolds-averaged water vapor tendency equation (Eq. 2.1). Using this framework, they primarily considered the contributions by terms II and IV in Eq 2.1, the moisture advection by the horizontal wind ($\vec{V_h}$) and the turbulent moisture flux convergence terms. The final term (Term III), the moisture advection due to vertical motion ($\overline{w}$), was implicitly neglected in their analysis. The absence of this term was because their analysis only looked at the near-surface, where $\overline{w}$ is approximately 0.

$$\underbrace{\frac{\partial q_v}{\partial t}}_{I} = -\underbrace{\vec{V_h} \cdot \nabla_h q_v}_{II} - \underbrace{\overline{w}\frac{\partial q_v}{\partial z}}_{III} - \underbrace{\frac{\partial \overline{w' q_v'}}{\partial z}}_{IV} \tag{2.1}$$

Fitzjarrald and Lala (1989) sought to understand the causes of q_v jumps in the context of radiation fog development. Their motivation was that increases in q_v decreased the time needed to reach saturation by radiative cooling within the surface layer, therefore accelerating fog development. By analyzing time series of vertical velocity variance (σ_w) and temperature, they deduced that the jumps in moisture occur when σ_w decreases below a certain value and rapid cooling occurs. In order to connect the decay of turbulence and cooling to the jump in q_v, they derived an equation illustrating how the second derivative of temperature with respect to time can be related to temporal changes in the surface sensible heat flux and net radiation. Their analysis also showed that during q_v jumps, an extended period of upward latent heat and downward sensible heat flux occurred, suggesting that the turbulence moisture flux convergence term (Term IV) primarily contributed to jumps in q_v.

In a follow up paper, Acevedo and Fitzjarrald (2001) sought to understand the spatial and temporal variability of moisture in the surface-layer during the Hudson Valley AET. Using an idealized large eddy simulation (LES), they simulated the AET in sloped terrain and quantified contributions of horizontal advection and flux divergence on the spatial and temporal distributions of temperature and water vapor. They found that the contributions from flux divergence primarily were responsible for jumps in q_v and advective terms played a role after the jump occurred. This was caused by their use of an idealized LES run; their simulation was able to develop large gradients in moisture (∇q_v) due to the sloped terrain and the turbulent flux term. The knowledge gained by their LES may be used to explain the behavior of q_v during the AET when elevation varies, and may not be applicable outside the Hudson Valley.

Unmanned aerial system (UAS) observations presented in Bonin et al. (2013) also suggest that the turbulent flux convergence term is the source for AET q_v jumps. In their study, Southern Great Plains AETs were sampled to obtain vertical profiles of sensible and latent heat flux. During one clear sky, light wind AET case, moisture rapidly increased near the surface. Because of the weak winds, moisture and temperature advection was assumed to be negligible. During this time period, the latent heat flux profile within the lowest 50-m decayed rapidly with height at a rate of roughly 0.4 $W/m^2/m$, suggesting that the turbulent flux convergence term contributed to the observed rise in moisture.

More recently, q_v changes during the AET have been studied in Huntsville, AL. Busse and Knupp (2012) used a combination of vertical profiling and surface-based instruments to argue that the definition of the ET (sensible heat flux reversal) is too simplistic. By using cases from only the summer and autumn months, Busse and Knupp (2012) found that changes occur aloft that are not accounted for in this definition, such as changes in wind speed and turbulence. They also documented surface q_v increases occurring an hour before and after sunset. Using the same set of instruments, Wingo and Knupp (2015) expanded the number of AET cases and showed that q_v increases typically began 80 minutes prior to sunset. They also found that increases in q_v were largest in the summer (1.3 g/kg) while during the spring and autumn increases were between 0.7 and 1.1 g/kg. Inspection of individual AET cases showed that these increases were often created by short-term jumps similar to the ones found in Fitzjarrald and Lala (1989) and Acevedo and Fitzjarrald (2001). Wingo and Knupp (2015) also suggested that these increases were due to the combination of a reduction of vertical mixing and evapotranspiration throughout the AET (term IV of Eq 2.1).

2.3 Turbulence Decay during the AET

It is clear from a survey of current literature, that the contributions of vertical flux divergence to changes in temperature and humidity cannot be neglected during the AET. Because of this, many papers researching the AET have focused on understanding how turbulence decays. These studies are complicated by the fact that changes to the boundary layer during this transition are complex; turbulence can be intermittent and anisotropic. Horizontal inhomogeneities may also be present, and the combination of rapidly changing conditions and weak surface forcing may also complicate studying the transition. These conditions depart far from the continuous, homogeneous, and stationary conditions often present in daytime convective boundary layers.

To better isolate these complicating factors, numerical simulations have been used in studies of the AET. Various studies simulate the transition using single column models (SCM), large eddy simulations (LES), and direct numerical simulations (DNS). In one of the earliest studies of this type, Nieuwstadt and Brost (1986) studied the decay of turbulence within the atmospheric convective mixed layer by suddenly shutting off the surface sensible heat flux. This paper demonstrated that during the AET, turbulence in the form of larger eddies tends to persist in the developing residual layer, while smaller eddies are destroyed close to the surface. These results were confirmed in Sorbjan (1997), who revisited this problem by using a more realistic evolution of the surface sensible heat flux. By doing this, they showed that turbulence decays much more slowly when the sensible heat flux decays gradually. Additional support for these ideas was found in Shaw et al. (2009), who repeated Sorbjan (1997) but with direct numerical simulations (DNS). In addition to a more realistic

decaying sensible heat flux, Shaw et al. (2009) also showed that the presence of a mean wind in the boundary layer also delays the collapse of turbulence that occurs during the AET.

Many of the hypotheses supported by these simulations have been reinforced by observations of the AET. Grant (1997) confirmed the aforementioned LES results by showing how the peak of the vertical velocity spectra of the developing residual layer and the surface layer separate during the AET. Within the surface layer, the spectra shifts to smaller length scales, while aloft the spectra remains unchanged. Unfortunately, many of these observational studies have been restricted to the surface layer, where instrumentation can be most easily deployed. The comparisons between LES and SCM simulations to observations in Beare et al. (2006) and Edwards et al. (2006) demonstrated that both numerical simulation methods could reproduce many aspects of the transition (e.g., vertical stratification and the development of the nocturnal jet). Lothon et al. (2014) highlighted that despite these capabilities, capturing the correct timing of the transition remains a challenging problem.

Recently, many of the questions regarding boundary layer turbulence during the AET were attacked through the Boundary Layer Late Afternoon and Sunset Turbulence (BLLAST) field project (Lothon et al. 2014). In their overview paper, they laid out scientific questions towards understanding the evolution of 1.) turbulence kinetic energy (TKE) and 2.) characteristic length scales of turbulence, both which are used in Mellor-Yamada-based PBL parameterization schemes (Mellor and Yamada 1982) to describe turbulent eddies. In a two part series of papers, Nilsson et al. (2016a,b) used the TKE budget equation to understand changes in TKE during the afternoon transition. Nilsson et al. (2016b) also helped understand the behavior of the pre-residual layer, which begins in

the later parts of the afternoon transition as a layer of reduced turbulence that grows downward with time from the capping inversion towards the surface as a result of a decaying surface sensible heat flux (Darbieu et al. 2015). Although BLLAST documented near-surface moisture jumps similar to past studies, a survey of the current literature does not show any studies using BLLAST data on this topic.

Chapter 3

Research Questions and Hypotheses

This dissertation adds to the current scientific knowledge in three ways. First, this research improves our understanding of the vertical and horizontal changes in moisture during the SGP AET. This geographic region has not been investigated thoroughly in past work. For example, papers such as Fitzjarrald and Lala (1989); Acevedo and Fitzjarrald (2001); Busse and Knupp (2012) and Wingo and Knupp (2015) have only focused on AET surface moisture changes in New York and Alabama. The BLLAST studies previously mentioned took place in Southern France (Lothon et al. 2014). Prior to this work, only two cases of q_v increases in the lowest 100 m during the SGP AET have been documented (Bonin et al. 2013). Because of this geographical bias in the literature, the AET in northern Oklahoma at the ARM site is a key focus of this research.

Second, this research seeks to clarify how changes in moisture impact parcel conditional instability during the AET. As many scientists attribute deep, moist convection changes to NLLJ-related increases in shear, a look at conditional instability changes during the SGP AET may motivate future studies. Such studies could better clarify the individual contributions of shear and moisture to observed changes in storm properties during the AET. Although this study does not directly illustrate how moistening parcels change storm properties (e.g. trajectories within the storm inflow), it does investigate changes to the environment, which has been used to infer storm characteristics and evolution

by many other investigators (e.g., Rasmussen and Blanchard (1998); Thompson et al. (2003); Edwards et al. (2012); Thompson et al. (2012a)).

Lastly, while the literature has primarily argued that vertical flux divergence plays an important role during the AET, a review of the literature has revealed that moisture advection during the AET has not been fully controlled for in past experiments. However, these studies have primarily considered only changes in the near-surface water vapor. Because of this, this study will revisit this problem and will use networks of remote sensors and numerical simulations that can provide the evolution of water vapor throughout the decaying convective boundary layer (CBL). By considering the depth of q_v jumps, additional clues about the processes driving these q_v increases may be found (advection vs. turbulent moisture flux convergence).

The science questions this dissertation seeks to answer are as follows:

1. What is the spatiotemporal evolution of water vapor (q_v) in the Southern Great Plains during the AET?

2. How do these jumps in moisture change the parcel conditional instability?

3. What processes facilitate these jumps in q_v?

Throughout this dissertation three hypotheses will be tested in order to answer the above questions:

H1: Increases in q_v can be found where vegetation is present.

H2: AET jumps in q_v may act to increase the conditional instability of parcels within the changing PBL.

H3: Jumps in q_v are caused by advection of q_v rather than the turbulent moisture flux convergence term discussed in past literature.

Within this dissertation, these hypotheses will be tested using a combination of observations in the horizontal and vertical in Oklahoma, similar to the methodologies used in Busse and Knupp (2012); Wingo and Knupp (2015). To do so, datasets collected and developed for the ARM SGP site in northern Oklahoma will be used (Sisterson et al. 2016). In the following two chapters, the ARM instrumentation, processing, and simulations provided by the ARM program are discussed at length. First, Chapter 4, describes the instruments used and describes a method of combining ARM remote sensor data to produce high-temporal resolution vertical profiles of temperature and humidity. At the end of this chapter, the numerical simulations provided by the ARM program that are used in this research are described. In Chapter 5, the thermodynamic profiles retrieved from ARM observations will be compared against those obtained by radiosondes. This comparison is achieved via direct comparison of the observed profiles and convection indices derived from them. These two chapters (Chapter 4 and 5) generally reproduce the work described in Blumberg et al. (2015) and Blumberg et al. (2017b), however with a focus on radiosondes released within the AET time period.

With knowledge of some of the tools used in this study in hand, Chapters 6, 7, and 8 investigate the problem of the AET moisture increase. Within Chapter 6, two decades of data from the Oklahoma Mesonet are used in several tests to understand if AET moisture jumps have a dependency on the land-surface characteristics (**H1**). In Chapter 7, the analysis of how moisture evolves in the horizontal is extended to the vertical dimension to understand the vertical depth of AET moisture jumps. Throughout these two chapters, attention will be paid towards testing the idea that the observed jumps in moisture can overcome the loss of instability driven by reduced insolation (**H2**).

$$\underbrace{\frac{\partial q_v}{\partial t}}_{I} = -\underbrace{\vec{V_h} \cdot \nabla_h q_v}_{II} - \underbrace{w\frac{\partial q_v}{\partial z}}_{III} - \underbrace{\frac{\partial \overline{w'q_v'}}{\partial z}}_{IV} \tag{3.1}$$

In Chapter 8, this investigation shifts towards understanding the different processes that control these jumps in moisture, restated again in Equation 3.1. A combination of numerical simulations and observations are used to help distinguish which jumps in water vapor are due to advection (terms II and III shown in Eq. 3.1) compared to turbulent flux divergence (term IV). Particular attention will be paid to the depth of the moisture jump to help identify if jumps are driven by advection or the collapse of turbulence (**H3**). In the final chapter of this dissertation, results are summarized and ideas for future explorations of this topic are discussed.

Chapter 4

ARM Instrumentation, Algorithms, and Simulations

Because the ARM Central Facility site in northern Oklahoma hosts a wide variety of instrument types, it is ideal for studying the SGP AET (Sisterson et al. 2016). The datasets provided by the ARM program provide researchers the ability to describe the surface energy balance, cloud properties, and the various characteristics of the planetary boundary layer (PBL) over the diurnal cycle. Figure 4.1 illustrates the location of five of the instruments used in this study and their location at the ARM SGP site. These five instruments (eddy covariance system (ECOR), energy balance Bowen Ratio system (EBBR), Raman lidar (RLID), Doppler lidar (DLID), and the Atmospheric Emitted Radiance Interferometer (AERI)) are heavily used to characterize the evolving PBL in this study. The details of the ARM instruments, their data processing algorithms, and the numerical simulations ARM provides to compliment their measurements are described in this chapter.

In the first section of this chapter, ARM surface in-situ observations are discussed. These datasets are primarily used to understand the evolution of the near-surface water vapor, sensible heat fluxes, and latent heat fluxes. As these observations can help indicate the various segments of the diurnal cycle (e.g., the evening transition), they are important to include in AET analyses (Fitzjarrald and Lala 1989). These observations are also relevant to testing **H1**, as they can be used to identify evapotranspiration from the Earth's surface

and are located near different land surface types (e.g., the ECOR is directly north of winter wheat in the spring, EBBR over grasslands and pasture, Bagley et al. (2017)). In the next section, the ARM instrumentation used for classifying sky cover are also discussed. Cloud cover observations are important to use when analyzing AET data, as many past studies have indicated that the environmental changes characteristic of the AET (e.g., reduction of the surface winds), are best observed when the sky is clear or the sky has scattered clouds (Fitzjarrald and Lala 1989; Acevedo and Fitzjarrald 2001; Bonin et al. 2013; Wingo and Knupp 2015). Overall, the datasets described in Section 4.1 provide information on the exchange of energy between the sun, Earth's surface, and the atmosphere.

Next, Section 4.2 includes information about the various remote sensors used to obtain high resolution soundings of the atmosphere. As this research will look vertically into the boundary layer undergoing a transition between convective and stable boundary layers, it is important to understand the capabilities of each observing system. First, the individual instruments (microwave radiometer (MWR), AERI, RLID, DLID) are discussed. Next, the algorithm used to merge the data from these individual instruments is described. The high-resolution soundings that are derived from this algorithm are compared to co-located radiosonde launches in Chapter 5. Later, they are used to illustrate the changes occurring in the vertical during the ARM AET (Chapter 7).

In the final section of this chapter, the configuration of the numerical simulations used in this experiment are described (Section 4.3). These simulations are used to derive diagnostics that can help better understand the evolving atmosphere at the ARM SGP site. A discussion of the forcing datasets used

to derive these simulations is included in this section. The results from these simulations are discussed in Chapter 8.

Figure 4.1: A map of the ARM Central Facility site and the location of the key ARM instruments used in this dissertation. Image provided by Dave Turner.

4.1 Surface-Based In-Situ Observations

In the following subsections, the ARM surface meteorological (MET), ECOR, EBBR datasets are discussed. After that, ARM instrumentation used to describe the cloud-cover near the ARM site is summarized. These surface-based, in-situ measurements are listed in Table 4.1 to summarize the various properties of each ARM dataset.

4.1.1 Surface MET

The MET dataset consists of typical surface meteorology observations such as temperature, humidity, pressure, wind speed, and wind direction. These observations are taken between 2 and 10-meters above ground level (AGL) at a frequency of 1-minute. Recently, Kyrouac and Theisen (2017) revealed that temperature observations taken by the MET instruments are cold biased in high-humidity environments. Because water vapor mixing ratio (q_v) was derived from the MET data in this research and is dependent upon temperature, the MET data underwent a bias correction prior to its use in this research. This bias correction was performed by using the radiosondes launched four times daily between 2016-2017 at the ARM SGP site (6-hour intervals at 0, 6, 12, 18 UTC) to develop a new calibration curve for the biased observations.

4.1.2 ECOR and EBBR Systems

As previously mentioned, the ARM program offers observations that describe the surface energy balance at the ARM SGP site. Inclusion of this data stream is important to have as it is connected to the decay of turbulence within the PBL

Table 4.1: A summary of the surface-based, in-situ observations used in this study. Δt represents the temporal sampling frequency, while z indicates the height of the observation. For each ARM dataset used, a reference is included to the ARM documentation.

Datastream and Reference	Δt	z	Variables Derived
Surface Meteorological (MET) Ritsche (2008)	1-min	2-m – 10-m –	$T(t)$ $q_v(t)$ $u(t)$ $v(t)$
Eddy Covariance System (ECOR) Cook (2016a)	30-min	8-m	Latent Heat Flux ($E_{ECOR}(t)$) Sensible Heat Flux ($H_{ECOR}(t)$)
Energy Balance Bowen Ratio (EBBR) w/ Bulk Aerodynamic correction Cook (2016b)	30-min	8-m	Latent Heat Flux ($E_{EBBR}(t)$) Sensible Heat Flux ($H_{EBBR}(t)$)
Total Sky Imager (TSI) Morris (2005)	30-s	N/A	Cloud Fraction

during the AET (e.g. Nieuwstadt and Brost (1986); Busse and Knupp (2012); Jensen et al. (2016)). Importantly, past studies described observations where q_v increases seemed to be initiated by the beginning of the evening transition (ET) (Fitzjarrald and Lala 1989; Acevedo and Fitzjarrald 2001). This result makes identification of the evening transition in observations particularly important to this study. During the analysis of the SGP AET cases, observations of surface latent and sensible heat flux values are used to identify the ET and characterize any evapotranspiration occurring during the AET.

ARM uses two different technologies to measure latent and sensible heat fluxes: eddy covariance (ECOR, Cook (2016a)) and energy balance Bowen ratio (EBBR, Cook (2016b)) systems. ECOR systems use Reynolds averaged high-frequency observations (typically a frequency of 10 Hz) of momentum, temperature, and trace gases (e.g., water vapor), and a variety of correction algorithms to derive surface fluxes. However, when considered with measurements of other fluxes (e.g., net radiation and soil heat), the fluxes derived from the ECOR method may not close the surface energy budget. In comparison, the EBBR uses measurements of net radiation and thermodynamic quantities at two levels to derive the fluxes. This method enforces closure when deriving the surface sensible and latent heat fluxes. Despite these differences, fluxes derived from the EBBR and ECOR compare well. Fritschen et al. (1992) found that the sensible heat fluxes between the two instruments were similar, however the EBBR latent heat flux was 10-15% smaller than the ECOR. At the ARM site, these two measurements are well correlated (Bagley et al. 2017).

At its most fundamental, the ECOR method consists of taking a time series of vertical velocity (w) and scalar measurements (e.g. q_v) over a specified time period (typically 30 minutes) and subtracting off a mean from each time

series. Next, these new time series describing the perturbations of w and q_v are multiplied together and averaged over the entire length of the sampled time series. Although the algorithm is simple to perform, many preprocessing steps are performed first to obtain a useful time series from imperfect observing systems. Depending upon the instrumentation, additional corrections can be performed on the derived fluxes.

ARM ECOR systems used in this research contain open-path infrared gas analyzers (IRGA, model LI-7500) to sample the water vapor density and carbon dioxide concentration and a fast-response three-dimensional sonic anemometer (model WindMaster Pro) to obtain the three components of the wind (u, v, w). Preprocessing steps for this system include procedures to remove spikes from the dataset, quality control checks for each data point, apply corrections for frequency attenuation, and account for sensor separation. These various steps are summarized in Vickers and Mahrt (1997). Next, 2-D coordinate rotations are applied to the sonic anemometer data to achieve a mean vertical wind speed of zero, accounting for possible errors in instrument orientation. After these preprocessing steps have been applied, vertical fluxes of sensible, latent, and carbon dioxide are calculated from these rotated observations. As the IGRA used is open-path, a final correction is made to the flux measurements to account for density changes due to heat and water vapor (Webb et al. 1980). The final output from this process produces observations of sensible heat ($H_{ECOR}(t)$) and latent heat fluxes ($E_{ECOR}(t)$) every 30-minutes. Per Cook (2016a), the errors in the derived fluxes are roughly 10% of their measured value.

The ARM EBBR systems used in this study also produce 30-minute fluxes. Each station uses two aspirated Vaisala and PRTD temperature and relative humidity probes, REBS-brand net radiometer and soil sensors, and Met One

sensors to determine pressure and wind observations. To derive the fluxes, the EBBR method uses the REBS sensors to constrain the net radiation and soil fluxes. Next, the vertical gradients of temperature and vapor pressure (derived from the instruments) are used to compute the Bowen ratio β (Gavilán and Berengena 2007). An assumption in this step is that the eddy transfer coefficients for water vapor and heat are assumed to be equal. Although this method works well during the daytime, near sunrise and sunset β can approach -1, often causing spikes in the derived sensible and latent fluxes. To handle these erroneous data points, ARM data processing uses the EBBR instrumentation to replace the surface flux values with those derived from Monin-Obukhov similarity theory (Monin and Obukhov 1954). Similar to the ECOR measurements, the values derived from the EBBR data generally exhibit a 10% error (Cook 2016b).

4.1.3 Sky Type Detection

Observations from the Vaisala CL31 ceilometer (Morris 2016), and Total Sky Imager (TSI) are used to characterize the sky cover of each SGP AET. While the ceilometer provides backscatter observations to help identify clouds and precipitation overhead, cloud coverage over a larger portion of the sky can be estimated by the TSI (Morris 2005). The TSI combines both regular photos of the sky and an image processing algorithm to estimate the cloud fraction of opaque and thin clouds. Although TSI retrievals of fractional sky cover are only valid for solar elevation angles of 10 degrees or greater, this range enables an estimate of the cloud cover in the hours prior to sunset. This system is frequently monitored by the ARM instrument mentor to identify and correct for issues with the algorithm. Together, both the ceilometer and TSI were used to

identify cloud cover during the AETs occurring at the ARM SGP site. In some cases, GOES visible satellite from the NCAR/UCAR Image Archive[1] was used to further understand relationships between EBBR and ECOR observations (e.g., fields of cumulus clouds across northern Oklahoma disappearing when the ECOR indicated the evening transition had begun.)

4.2 Remote Sensors

As the AET can be a rapid process, it is both expensive and impractical to measure its evolution using radiosondes. Instead, remote sensors such as lidars and passive radiometers deployed by the ARM site are used. These instruments take advantage of the different ways radiation interacts with a medium to retrieve variables that describe the atmosphere (e.g., temperature, humidity, wind speed). The radiative transfer equation (RTE) describes the factors that influence the path of photons as they are either transmitted or received by remote sensors. This equation can be used to solve for the intensity of photons along a path ($\mathbf{\Omega}$) due to transmission, absorption, and scattering:

$$\frac{dI(\mathbf{\Omega})}{d\tau} = I(\mathbf{\Omega}) - (1-\omega_0)B(T) - \frac{\omega_0}{4\pi}\int_{4\pi} P(\mathbf{\Omega}', \mathbf{\Omega})I(\mathbf{\Omega}')d\mathbf{\Omega}' \qquad (4.1)$$

The left hand side of Equation 4.1 describes the change of radiation intensity dI along a path with respect to the change in optical depth ($d\tau$) of the medium the photons are passing through. The right hand side of the RTE describes the current intensity along the path $I(\mathbf{\Omega})$, and the addition of photons due to emission along the current path by the medium being considered ($(1-\omega_0)B(T)$). The last term describes the scattering of photons from all solid angles ($d\mathbf{\Omega}'$)

[1] http://www2.mmm.ucar.edu/imagearchive/

into the current path. The single scatter albedo, ω_0, is the ratio of scattering efficiency to total extinction efficiency by the medium. This parameter controls the ratio of scattering to absorption performed by the medium; if $\omega_0 = 1$, no absorption occurs in the medium. If the photon is scattered, the probability of its new path being in the line of the current path can be computed via a probability density function, $P(\mathbf{\Omega}', \mathbf{\Omega})$. Whether a photon is absorbed, scattered, or transmitted is a function of parameters such as the wavelength of the photon, the angle of approach to a scatterer, the size of scattering particles compared to the wavelength of the incoming photon, and the refractive index of the medium it is passing through. By utilizing EM waves that interact with the atmosphere in distinct ways, scientists can infer atmospheric structure and composition from remote sensors.

There are two different methods remote sensors use to measure the atmosphere. In the first, remote sensors measure photons naturally emitted (or scattered) by the object being observed; these are called passive sensors. Instruments that use the second method are called active sensors; they emit electromagnetic radiation and listen for a specific return signal. In this research, both types are used. Table 4.2 summarizes some of the characteristics of the remote sensors that are used in this paper, and each instrument is described in more detail in the following sections.

4.2.1 Microwave Radiometers

Ground-based microwave radiometers (MWR) observe downwelling microwave radiation emitted by the atmosphere. Thermodynamic profiling MWRs typically observe EM radiation along the edge of the 22.3 GHz H_2O and 60 GHz O_2

Table 4.2: Active (A) and passive (P) remote sensing instruments used in this study. λ_R and λ_T correspond to the instrument receiver and transmitter wavelengths. Δt and Δz are the temporal sampling frequency and the vertical grid spacing from the profiling instruments. The final column indicates the variables retrieved from each instrument.

Instrument	λ_R	λ_T	Δt	Δz	Derived Product
AERI (P)	520-3300 cm^{-1}	N/A	5-min	See Fig. 5.2	$T(z)$ $q_v(z)$ LWP
MWR (P)	23.8, 31.4 GHz	N/A	1-s	N/A	PWV LWP
Raman lidar (A)	387 nm (N_2) 408 nm (H_2O) 354.27 nm 353.27 nm	355 nm	10-min	60-m	$T(z)$ $q_v(z)$
Doppler lidar (A)	1.5 μm	1.5 μm	15-min u,v 10-min w stats.	25-m u,v 30-m w stats.	$u(z)$ $v(z)$ $w(z)$ $\overline{w'^2}$ $\overline{w'^3}$

bands. MWRs typically sample the atmosphere at a frequency of 1 Hz and can perform elevation scanning to obtain additional data for profiling and calibration (Löhnert and Maier 2012). In order to identify instances where the signal observed may not be from the atmosphere, quality control flags are typically set if liquid water is present on the radome of the instrument due to precipitation or fog. In some cases, a blower is attached to the MWR to help remove liquid water from the radome.

MWRs maintain their calibration by three different calibration methods. The first two methods are automated, while the third is manual. In the first calibration routine, a blackbody kept within the instrument is observed by the instrument with a known noise perturbation and without that perturbation (Löhnert and Maier 2012; Küchler et al. 2016). This method produces two points that can be used to regularly derive a calibration equation during the instrument's operation. In the second automated routine, elevation scans with the MWR are performed. By using relationships between optical depth and elevation angle, calibration of the instrument's lower opacity channels (typically 22.3 to 31.2 GHz) can be performed. This second method is commonly referred to as "tip-curve" calibrations (Cadeddu et al. 2013). In the final method, a secondary blackbody target filled with liquid N_2 is used to calibrate both the noise perturbation and the instrument. This final method is commonly used to calibrate all available MWR channels (Han and Westwater 2000; Maschwitz et al. 2013).

Ground-based MWRs are often used to obtain precipitable water vapor (PWV), liquid water path (LWP), and thermodynamic profiles. Various investigators have retrieved temperature and water vapor profiles from MWR

observations by utilizing the information within the H_2O and O_2 bands (Hewison 2007; Löhnert et al. 2009; Löhnert and Maier 2012; Blumberg et al. 2015). These retrievals have been used to study bores and severe weather in the past (Chan and Hon 2011; Cimini et al. 2015; Koch et al. 2016). Retrievals of LWP and PWV (Turner 2007) (MWRRET) have been used as a reference point for correcting dry biases that have been identified in certain radiosonde models (Turner et al. 2004; Turner 2007).

4.2.2 The Atmospheric Emitted Radiance Interferometer

The AERI is a ground-based interferometer that receives downwelling, infrared radiation between the wavelengths of 3.0 and 19.2 microns (520 - 3300 cm^{-1}) at a unapodized spectral resolution of 0.5 cm^{-1} (Knuteson et al. 2004). AERIs typically sample the atmosphere every 20 seconds. AERI instruments regularly perform a self calibration process by observing two blackbodies housed within the instrument casing. The first is kept at 333 K; the second changes with the ambient temperature. Through this calibration process, the AERI spectral accuracy is kept at a level better than 1% of the ambient radiance. Although the instrument can operate in both clear and cloudy conditions, precipitation can harm the foreoptics of the instrument. Because of this risk, a precipitation sensor has been mounted on the instrument and is used to determine when to close the instrument's hatch.

AERIs were originally developed to improve models of infrared spectroscopy (Turner et al. 2016). Such studies are called closure studies, in which scientists utilize a combination of instruments to identify and resolve inconsistencies between observations and numerical model output. In the case of AERI-related closure studies, the goal is to improve the line-by-line radiative transfer model

(LBLRTM) (Clough et al. 1992) by using co-located observations of AERI spectra and radiosonde observations. Such studies are difficult, as many sources of error must be controlled for in both the LBLRTM and observations. However, several closure studies performed in varying climatic regimes have successfully improved numerical modeling of the water vapor and carbon dioxide continuum (Tobin et al. 1999; Turner et al. 2004; Delamere et al. 2010; Turner et al. 2012; Mlawer et al. 2012). By updating the spectroscopy of the LBLRTM through these types of studies, both the accuracy of AERI-derived thermodynamic profiles and fast radiative transfer models used in data assimilation can be improved.

AERI-derived thermodynamic profiles have helped study various atmospheric phenomenon and have helped understand of how such instruments could be used in operational meteorology. Studies utilizing a network of 5 AERIs between 1999-2003 in the SGP documented several severe weather events and illustrated how trends of AERI-derived convection indicies (e.g., CAPE and CIN) could be used to anticipate severe weather and convection initiation (Feltz and Mecikalski 2002; Feltz et al. 2003; Wagner et al. 2008). Bonin et al. (2015) used thermodynamic profiles derived from the AERI to identify static stability differences in weakly stable and strongly stable SGP nocturnal boundary layers. This set of research has shown that the AERI can be used in many applications.

4.2.3 Raman Lidar

RLID and differential absorption lidar (DIAL) utilize the properties of extinction (scattering and absorption) to obtain profiles of various atmospheric variables. Both lidar types alternate between transmitting pulses of light and recording the radiation backscattered to the instrument. The returned signal

is recorded as a function of time and is used to derive the range of targets. Both lidar systems can utilize the ratio of received backscatter at two different wavelengths to derive atmospheric properties such as water vapor or temperature. However, the method and processes each instrument use to measure these properties differ significantly.

DIALs transmit at two wavelengths (Spuler et al. 2015; Weckwerth et al. 2016) to measure atmospheric concentrations of trace gases. One transmitting wavelength is set to the absorption line for a specific gas (the on-line frequency). The second transmitting wavelength is set close to the first, where absorption by the gas being measured is significantly smaller (the off-line frequency). Both wavelengths used are within a portion of the electromagnetic spectrum where molecular scattering is very weak, but scattering from the individual wavelengths are primarily a function of the profile of atmospheric aerosols. Using the level of relative attenuation between the two lasers, the concentration of the gas being measured can be calculated. As the system relies on absorption by the gas being measured, DIAL systems require highly calibrated and precise transmitters.

The ARM RLID at the SGP site, on the other hand, emits laser radiation at only one wavelength (Turner and Goldsmith 1999; Turner et al. 2002). The signal returned to the lidar by aerosols, clouds, and molecules in the atmosphere contain both elastic (Rayleigh scattering) and inelastic (Raman scattering) scattering components. Elastic scattering by photons (e.g. Rayleigh scattering) conserves the frequency of the incoming photon. Inelastic scattering, however, occurs when the frequency of the photon is shifted and the kinetic energy of the incoming photon is not conserved. A majority of the scattering by photons that

occurs in the atmosphere is elastic. Inelastic scattering is 3-4 orders of magnitude smaller than elastic scattering. Because of this, RLID systems require a sensitive receiver.

Similar to the DIAL, ratios are calculated from signals received by the ARM RLID to calculate thermodynamic profiles (Turner and Goldsmith 1999; Newsom et al. 2013). After transmitting at 355 nm (UV wavelength), receivers record Raman scattering by H_2O ($\lambda = 408$ nm) and N_2 ($\lambda = 387$ nm) through two fields-of-view: the high or narrow field of view (NFOV) and low or wide field of view (WFOV). Because the signal of N_2 and H_2O backscatter approximates the amount of dry and moist air with height, the ratio of these two channels is calculated to derive the $q_v(z)$ profile (Turner and Goldsmith 1999). When temperature is measured by the RLID, the rotational Raman (RR) technique is applied by measuring the signal from the NFOV with two more receivers: one at 354.27 nm and another at 353.27 nm. These two channels are sensitive to the rotational energy state transitions of atmospheric nitrogen and oxygen molecules. Division of these two received signals results in a range-dependent quantity that is dependent upon temperature within the scattering volume (Newsom et al. 2013). By calculating ratios between the variety of signals received in the NFOV and WFOV, temperature and water vapor profiles are derived.

The estimated temperature and water vapor profiles from this process undergo several corrections typical for lidars (e.g., subtraction of the solar background, dead-time corrections; Turner and Goldsmith 1999; Newsom et al. 2013. In the final steps of ARM RLID calibration process, a correction to compensate for an incomplete overlap of the detector and transmitter is preformed. This step typically uses co-located radiosonde launches to determine an overlap function $O(r)$. $O(r)$ describes what fraction of the laser beam cross section at a

given range will be imaged onto the detector. For the WFOV, complete overlap (where $O(r) = 1$) typically occurs around 800 m, where as for the NFOV, it occurs near 4 km. After the overlap is corrected for, the ARM RLID profiles are calibrated to agree with radiosonde profiles. Due to the differences in where the NFOV and WFOV best sample the atmosphere, calibrated water vapor profiles from the two FOVs are merged via weighted averaging.

The ARM site has used the RLID to measure profiles of water vapor for more than two decades (Sisterson et al. 2016). Because of this fact and its applicability to the focus of this study, data collected by this RLID are used to study the AET. This data was collected from March to August for 2 years (2016 to 2017) and has a temporal spacing of 10 minutes. To illustrate the accuracy of the RLID data calibrated by the aforementioned calibration process, RLID profiles (below cloud base, if it exists) and co-located 23 UTC radiosonde launches were compared. In these comparisons, the accuracy of both q_v and T profiles obtained from the RLID were assessed.

Figure 4.2 shows this assessment for both the RLID temperature and merged q_v profiles. The temperature profile is largely unbiased (below 0.5 C), except for the profile below 500-m. For the T STD profile, the STD starts off near 3 °C at the surface and decreases to almost 2 °C just above 1 km. There, the STD remains constant until 2 km where the STD begins to increase at a rate of 1 °C/km. These results suggest that these RLID T profiles are most accurate between 1 km and 4 km, which is expected given that the NFOV is unable to detect the temperature close to the RLID as well given the incomplete overlap at these ranges.

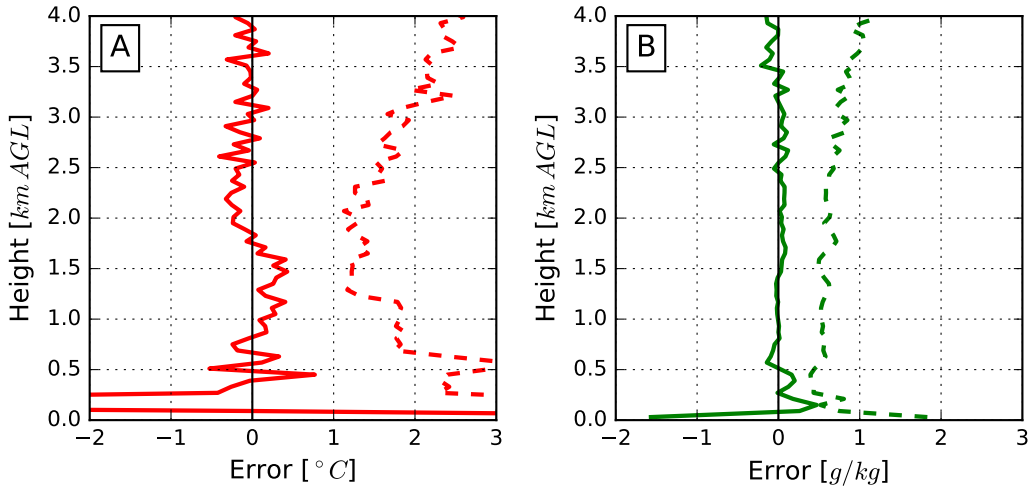

Figure 4.2: Bias (solid line) and 1-σ standard deviation (dashed line) of RLID derived temperature (A, n=144) profiles and water vapor mixing ratio (B, n=287) profiles.

However, Figure 4.2b shows that accuracy of the 23 UTC RLID q_v profiles is higher closer to the surface. The bias shown is close to 0 g/kg at 300-m and aloft. The STD is less than 1 g/kg in the lowest 300-m. These improved statistics closer to the surface compared to the T profile are due to the combined profiles of the NFOV and WFOV channels. The channels used to deriving the T profile however, are only from the NFOV. Such results suggest that the ARM RLID q_v profiles above the lowest few range bins are adequately calibrated.

4.2.4 Doppler Lidar

The Halo Doppler Lidar (DLID) is an active remote sensor that emits and receives radiation within the near-IR portion of the EM spectrum (1.5 microns) (Pearson et al. 2009; Newsom 2012). The radial wind $V(r)$ at range r is measured by observing the Doppler shift of the returned signal from various targets in the atmosphere. Within the PBL, DLID targets are primarily atmospheric aerosols, which is useful as they can act as passive tracers of the wind. The ARM

DLIDs have distinct differences from other DLIDs. Along each radial, the ARM DLIDs observations have a Nyquist velocity of 19.4 m/s and a precision of less than 10 cm/s (Newsom 2012). ARM DLIDs include a telescope that can change in both azimuth (θ) and elevation (ϕ). By using various scan patterns, ARM DLIDs provide profiles of wind direction and speed in the atmosphere.

Two different scan patterns are used by ARM DLIDs. The first is the plan position indicator (PPI), where the DL telescope is rotated 360 degrees in azimuth at a constant elevation. From this scan pattern and the velocity azimuth display (VAD) method, the 3D wind can be retrieved (Lhermitte 1961). In this method, measurements of velocity by azimuth for a single range bin are plotted, and a sine wave is fitted to the data to retrieve the wind speed and direction with height. ARM VAD scans occur every 15 minutes to obtain the horizontal wind at an elevation of 60 deg above the horizon. In this study, ARM DLID wind profiles are used to understand how the wind evolves throughout the AET.

In between the PPI scans, the second scan pattern occurs. During this time, vertical stares sample the atmosphere at a frequency of 1 Hz to obtain a time series of $w(z)$. From these time series, vertical velocity statistics can be produced as various eddy sizes in the boundary layer can be resolved. In the ARM value added product (VAP) scripts that process the DLID data, these statistics are typically computed using a 30-minute window of $w(z)$. This processing uses the Lenschow et al. (2000) method to remove the contribution of instrument noise on w statistics (e.g., variance). These statistics are computed every 10 minutes by ARM and are used in this study to analyze the decay of convectively-generated turbulence during the AET relative to changes in low-level water vapor.

4.3 Retrieval Algorithms

Because scientists rarely measure the variables they wish to observe directly, various algorithms must be used to obtain the variables they wish to measure (e.g., profiles of T, q_v from AERI infrared radiances). This class of problems are referred to as inverse problems (Rodgers 2000). In inverse problem theory, the measurements made by an instrument are collected into a vector $\mathbf{y}$ of length i, called the measurement vector. The desired variables in the retrieval (where j is the number of variables and are unknown), are contained in the state vector $\mathbf{x}$. The two are related by the forward model F, which describes the understanding of the physics behind the measurement process to obtain $\mathbf{y}$. While these two vectors are directly related, in practice the observation generated by $F(\mathbf{x})$ is also perturbed by some error ϵ:

$$\mathbf{y} = F(\mathbf{x}) + \epsilon \tag{4.2}$$

The method by which $\mathbf{x}$ is obtained from $\mathbf{y}$ is called a retrieval. Although theoretically this problem can be well-posed and over constrained, often in practice it is not. In some retrieval problems, forward models are highly non-linear, creating a space where several different inputs may produce the same output within the uncertainties of $\mathbf{y}$.

There are two common strategies used to obtain $\mathbf{x}$: statistical and physical retrieval algorithms (Blumberg 2013). With statistical algorithms, large datasets containing predictors (e.g., radiance spectra) and predictands (e.g., temperature profiles) are related using statistical relationships or machine learning methods. With respect to instruments such as MWRs or AERIs, these

datasets can be created by inserting a dataset of observations (e.g., climatologies of radiosondes) into a forward model (a radiative transfer model) to simulate radiometric observations and produce a training dataset. Statistical retrievals are more computationally efficient compared to physical retrievals, however when their retrieved variables are input into the forward model the output may not match the observed spectra due to the fact that the function being approximated is often not one-to-one.

Physical retrievals, on the other hand, seek to find a solution that minimizes the difference between $\mathbf{y}$ and $F(\mathbf{x})$. These retrievals are often iterative, which increases their computational time. Physical retrievals have a set convergence criteria that serves to act as a break to the iteration loop. Because a convergence criteria is required, physical retrievals (as opposed to statistical retrievals) may not always provide an answer to the retrieval problem. Even so, physical retrievals tend to be noticeably more accurate than statistical retrievals as they are directly constrained by the physics described in F.

4.3.1 Optimal Estimation

Optimal estimation (OE) is one such physical retrieval method used to produce profiles of T, q_v from passive remote sensors (Rodgers 2000). Optimal estimation uses the Bayesian framework to invert Equation 4.2. In the OE retrieval method, the observations in $\mathbf{y}$ are used with the a priori, called $\mathbf{X_a}$. When solving for the variable $\mathbf{x}$ in Equation 4.2 with OE, the error covariance matrices for the observations and a priori are used, ($\mathbf{S_e}$ and $\mathbf{S_a}$, respectively) Inclusion of these error estimates in the retrieval has two benefits: 1.) it uses the errors to weight the contributions from the observations and prior to the

retrieval solution and 2.) it allows for the propagation of errors through the retrieval.

In the OE-retrieval framework, the retrieved variables are contained in the state vector $\mathbf{X}$ and the following equation is iterated n times until some set convergence criteria is reached:

$$\mathbf{X^{n+1}} = \mathbf{X_a} + (\gamma \mathbf{S_a}^{-1} + \mathbf{K_n^T S_e}^{-1} \mathbf{K_n})^{-1} \mathbf{K_n S_e}^{-1} [\mathbf{y} - F(\mathbf{X^n}) + \mathbf{K_n}(\mathbf{X^n} - \mathbf{X_a})]. \quad (4.3)$$

During each iteration, the Jacobian:

$$\mathbf{K_n} = \frac{\partial F_i}{\partial \mathbf{X_j}} \quad (4.4)$$

is updated, which describes the linear relationship between the ith observation in $\mathbf{y}$ and the jth retrieved variable in $\mathbf{X}$. Typically, values in $\mathbf{K_n}$ are solved for by finite differencing. As this requires running the forward model multiple times, the calculation of the Jacobian is often the most computationally expensive part of the OE method.

In instances where the retrieval problem uses a very non-linear forward model, the γ parameter can be used in the OE equation. By steadily decreasing the γ parameter as the retrieval iterates, the weight of the a priori relative to the observations can be controlled, effectively stabilizing the retrieval so convergence can be achieved. This formulation of the OE equation has been used in the past when retrieving thermodynamic profiles from infrared spectra collected by polar-orbiting satellite (e.g., Masiello et al. (2012)).

With each iteration, an estimate of the retrieval error covariance matrix ($\mathbf{S}$) can be solved for using the equations:

$$\mathbf{S} = \mathbf{B^{-1}}(\gamma^2 \mathbf{S_a}^{-1} + \mathbf{K_n^T S_e}^{-1} \mathbf{K_n}) \mathbf{B^{-1}} \tag{4.5}$$

and,

$$\mathbf{B} = (\gamma \mathbf{S_a}^{-1} + \mathbf{K_n^T S_e}^{-1} \mathbf{K_n}). \tag{4.6}$$

In addition to the uncertainty of the retrieved profile, the OE method offers an ability to quantify the information content within the observations. To do this, the averaging kernel $\mathbf{A}$ is calculated:

$$\mathbf{A} = \mathbf{B}^{-1}(\mathbf{K_n^T S_e}^{-1} \mathbf{K_n}) = \frac{\partial \hat{\mathbf{X}}}{\partial \mathbf{X}} \tag{4.7}$$

The averaging kernel describes the sensitivity of the retrieval solution $\hat{\mathbf{X}}$ to perturbations in the truth state $\mathbf{X}$. Values of 1 along the diagonal of $\mathbf{A}$ would describe a perfect inverse method where the observations would provide perfect information about every retrieved variable.

Two metrics derived from $\mathbf{A}$ can describe the information content of the OE retrieval. The first is the degrees of freedom of signal (DFS) metric. This metric is calculated by summing the values along the diagonal of $\mathbf{A}$ (Rodgers 2000). The second is the vertical resolution of the retrieval, which is calculated by taking the inverse of the diagonal of $\mathbf{A}$, and scaling it by the layer spacing of the retrieval (Hewison 2007).

4.4 LASSO

To supplement the ARM observations at the SGP site, the ARM program has begun to run LES models regularly (Gustafson Jr and Vogelmann 2015).

LES utilizes low-pass filtered versions of the Navier-Stokes equations to eliminate small-scale information from the simulation. Because these smaller-scale motions are important to the solution provided by the LES, they are modeled by sub-grid scale parameterizations. LES is a simplification of direct numerical simulation (DNS). DNS uses unfiltered versions of the Navier-Stokes equations to model the whole range of spatial and temporal scales turbulence can be found. Because of this modeling strategy, DNS is very computationally expensive and is difficult to use when simulating atmospheric flows. These flows often have a much higher Reynolds and Rayleigh number compared to those found in engineering problems (Ferziger et al. 2002).

These simulations, funded by the ARM program, are produced by the LASSO project. LASSO seeks to supplement ARM's various observing systems using a regularly run, high-resolution modeling system. Although principal investigators aim to use LASSO to help answer a number of science questions, its current configuration is oriented towards simulating shallow convection. Some of the current goals of the LASSO project include reducing biases in global circulation model (GCM)s, creating new methods of parameterizing convective clouds, and better representing heterogeneties in land-surface effects in GCMs (Gustafson Jr and Vogelmann 2015). This last category is directly relevant to the goals of this dissertation.

Currently, the LASSO Alpha 2 release dataset consists of approximately 544 simulations of 14 cases in the SGP area. Although the diversity of the model configurations used to create these runs is quite large, they are based off of only two numerical models. The first is the Weather Research and Forecasting (WRF) model version 3.8.1 (Skamarock and Klemp 2008). The second is the SAM model version 6.10.8 (Khairoutdinov and Randall 2003). Two primary

differences are apparent in these models. First, the set of equations used is different between the two models. While the SAM model uses the anelastic set of governing equations to simulate the atmosphere, the WRF uses the full, non-hydrostatic governing equations. Second, the ability to specify the boundary conditions for these two models differs. The WRF offers the ability to simulate the atmosphere using nested grids, but the SAM can only operate using periodic boundary conditions. In the future, the WRF will only be used as it has more flexibility in its modeling configuration than the SAM (Gustafson Jr and Vogelmann 2015).

Table 4.3 indicates the configuration and various settings that are used in the LASSO runs. The LASSO domain is a 14.4×14.4 km horizontal grid with a Δx of 100-meters and 226 vertical levels. LASSO runs are initialized from the 12 UTC radiosonde launched at the ARM site and are run for 15 hours to capture the entire daytime evolution. Output from each model by their respective statistical packages occurs every 10-minutes. With respect to the parametrization schemes used in LASSO, only the microphysics is varied; either the Morrison (Morrison et al. 2005) or Thompson (Thompson et al. 2004) are used in the provided simulations. All other schemes used are fixed across the runs. To simulate radiation, the Rapid Radiative Transfer Model GCM (RRTMG) is used, which utilizes the correlated-k approach to efficiently calculate radiative terms in GCM applications. The subgrid closure scheme used is based on the 1.5 order turbulent kinetic energy (TKE) approach outlined in Deardorff (1980).

Initially, both WRF and SAM LES simulations in the LASSO dataset were to be used to test the advection hypothesis (**H3**). Unfortunately, the initial analysis process using the WRF data was found to have some artifacts that have not yet been explained by the ARM LASSO team. Because of this, only

LES simulations from the SAM model are used in this dissertation. Future work however, will include the WRF dataset in additional tests of **H3**.

4.4.1 Simulation Forcing Datasets

Table 4.3 lists the three different forcing datasets that were used to drive the LASSO models. These forcing datasets provided estimates of the large-scale temperature and water vapor advection as well as surface sensible and latent heat fluxes at the bottom boundary of the LES. In addition, estimates of the large-scale vertical velocity from these datasets were also used to include the influence of large-scale subsidence or ascent on the LES domain. Each forcing dataset provides an updated estimate of the large-scale conditions at a frequency of one hour. Given that these three datasets provide estimates of the forcing applied throughout the entire LES domain, they are important to discuss at length. These three datasets, the VARANAL, the ECMWF, and the multi-scale data assimilation (MS-DA) are discussed in more detail below.

The VARANAL program initially was used to merge observations collected during ARM intensive operating periods (IOPs) and generate the large-scale forcing for single column models (SCM) (Zhang et al. 2016). Because the ARM program's initial goals were to use observations to improve parameterizations in general circulation models (GCMs, Li et al. 2015), it was important to control for the larger scale influences when diagnosing errors in parameterization schemes (Zhang et al. 2001). Originally, VARANAL used a variational analysis scheme and radiosondes released over a small number of stations located around the C1 site (Zhang and Lin 1997) to derive profiles of temperature and water vapor advection. The constraints in VARANAL seek to make small adjustments

Table 4.3: The LASSO model suite configuration. In the large-scale forcing and microphysics categories the various options for the runs are listed.

Model	WRF	SAM
Governing Equations	Full, Compressible	Anelastic
Solver	3rd/5th order Runge-Kutta	3rd-order Adams-Bashforth
Version	3.8.1	6.10.8
Reference	Skamarock and Klemp (2008)	Khairoutdinov and Randall (2003)
Boundary Conditions	Doubly Periodic	
Grid Spacing	$\Delta x = \Delta y = 100$ m $\Delta z = 30$ m, z > 5 km, $\Delta z = 300$ m near top	
Domain Size	14.4 km x 14.4 km 226 vertical levels (0 - 14.7 km)	
Initial Conditions	12 UTC RAOB	
Microphysics	Morrison (Morrison et al. 2005, 2009) Thompson (Thompson et al. 2004, 2008)	
Large-Scale Forcing	MSDA (Li et al. 2015, 2013; Feng et al. 2015) ECMWF (Xie et al. 2003)	
Surface Forcing	VARANAL (Xie et al. 2004; Zhang and Lin 1997; Zhang et al. 2001) MSDA (Li et al. 2015, 2013; Feng et al. 2015) ECMWF (Xie et al. 2003)	
Radiation	RRTMG (Clough et al. 2005; Iacono et al. 2008; Mlawer et al. 1997)	
Subgrid Closure	Deardorff (1980)	

to the raw data and conserve column-integrated mass, moisture, energy, and momentum. As many methods exist to derive the large-scale forcing, a paper by Zhang et al. (2001) sought to understand the sensitivities of each method (e.g., Barnes 1964). It was found that by adding constraints to the water and energy budgets in the VARANAL method (e.g., weighting surface fluxes from ECOR and EBBR and top of the atmosphere measurements from satellites), the uncertainties of the derived forcing was significantly reduced. In Xie et al. (2004), it was found that adding numerical weather prediction (NWP) data to the VARANAL algorithm further improved the derived forcing fields, especially in periods where precipitation is present.

The ECMWF forcing dataset uses physical and dynamic tendencies calculated directly from the ECMWF Integrated Forecast System (IFS) (Ahlgrimm and Forbes 2014). A benefit of this method is that it more accurately closes the moisture and energy budgets and can be considered over multiple spatial

scales (Gustafson et al. 2017). In the ECMWF IFS, each grid box occupies a 16 km by 16 km box, and represents the tendencies at a single column of the IFS. Comparisons between VARANAL and the ECMWF forcing in Xie et al. (2003) showed that SCMs run using both forcing types produced similar results in non-precipitating periods. As the LASSO runs are also done during non-precipitating periods, the simulations using the VARANAL and ECMWF datasets may exhibit similar evolutions.

The final forcing method, the multi-scale data assimilation (MSDA), uses large-scale forcing derived from a 2-km convection-permitting WRF simulation that has been constrained using the MSDA assimilation strategy (Li et al. 2013). Both reanalysis products and high resolution observations are used in the assimilation step to produce regular, three-dimensional meteorological fields near the ARM SGP site. By doing so, MSDA takes into account spatial features such as land-surface types and elevation when producing forcing estimates. At its foundation, the MSDA method uses the Community Gridpoint Statistical Interpolation (GSI), which is based on the three dimensional variational data assimilation (3DVAR) algorithm (Parrish and Derber 1992). Because data assimilation can unnecessarily filter out small-scale structures when applied to high-resolution models, a multi-scale data assimilation strategy is used instead. In this method, 3DVAR is still used, but the cost function being minimized is separated into large-scale and small-scale components. This reduces the amount of filtering on small scales, therefore creating a better analysis than traditional 3DVAR methods. Li et al. (2015) illustrated this by using forcing derived from the MSDA to run a SCM. Their results indicated that the SCMs forced using MSDA compared well to those forced by VARANAL, suggesting that the MSDA

method performed at least as well as VARANAL at capturing the large-scale forcing.

A variety of observations are assimilated into the MSDA to create each forcing dataset. Such observations include both ARM and conventional observations. The conventional observations assimilated encompass datasets such as satellite radiances and NOAA operational observations (radiosondes, Oklahoma Mesonet, etc.). Within the ARM category, ARM radiosondes and MET stations across northern Oklahoma are assimilated. With this release of the LASSO data however, the MSDA forcing dataset also includes wind profiles from four ARM SGP radar wind profilers. One profiler is located at the Central Facility while the other three are found 15 km away from the Central Facility.

These forcing datasets are applied to the LASSO models in similar ways. For these models, the large-scale advection is specified as an additional tendency term in the model moisture and thermodynamic tendency equations. These additional terms are applied at every gridpoint within the LES domain (Khairoutdinov and Randall 2003; Endo et al. 2015). For both models, computations of surface fluxes are bypassed; the surface fluxes are applied to all grid points on the lowest atmospheric model level. These advective and surface flux estimates are used in this study to quantify the individual contributions from the moisture tendency equation (**H3**)

Chapter 5

Verification of AERIoe Retrievals

To synthesize high-temporal resolution soundings from the aforementioned thermodynamic profiling instruments, the OE retrieval algorithm AERIoe is used (Turner and Löhnert 2014). AERIoe was developed to improve upon AERIprof (Feltz et al. 1998; Smith and Feltz 1999; Feltz et al. 2003), the first thermodynamic retrieval algorithm written for the AERI. AERIoe offers many improvements over AERIprof. First, AERIoe uses the LBLRTM (Clough et al. 1992) to relate AERI observations to profiles of temperature and water vapor, where as AERIprof used a forward model configured for the SGP with a fixed carbon dioxide concentration. Second, AERIoe can converge in clear and cloudy scenes even from a poor first guess, a capability that AERIprof struggled to achieve. AERIoe's ability to converge in cloudy scenes also enables estimates of liquid water path (LWP) from the retrieval algorithm. Finally, AERIoe also provides a full error covariance matrix with each retrieval, which is something AERIprof did not offer.

Originally, AERIoe only used AERI spectral bands to perform retrievals of temperature and humidity profiles. In version 2.0, AERIoe was upgraded to allow for alternative data sources (e.g., RLID, NWP profiles) to be included in the observation vector $\mathbf{y}$. This allows AERIoe to utilize information that can help to solve for the entire tropospheric thermodynamic profile, instead of just the lowest 4 km (Löhnert et al. 2009; Turner and Löhnert 2014; Blumberg et al.

2015). Later versions of AERIoe also include an adiabatic and supersaturation constraint within the algorithm (Turner and Blumberg (2018), in review).

For this research, a combination of AERI spectra (Figure 5.1), RLID profiles, surface observations, and numerical weather prediction (20 km Rapid Refresh analyses; Benjamin et al. 2016) from the ARM SGP site (Sisterson et al. 2016) are used in the AERIoe $\mathbf{y}$ vector. These observations are summarized in Table 5.1. Co-located radiosondes (Vaisala RS-92; Holdridge et al. 2011) launched at 23 UTC for the months of March-August 2016 and 2017 from the ARM SGP site are used to verify the accuracy of the retrieval configuration. Filtering was done to obtain cloud-free AERIoe retrievals (the retrieved threshold is $LWP < 6$ g/m^2) that used all data sources (e.g., Raman lidar, RAP, met data). This left 182 retrievals available for comparison.

In the following sections, these retrievals are compared to the co-located radiosondes in different ways. In Section 5.1, the accuracy of the retrievals are assessed. In addition, the results from two metrics are discussed (degrees of freedom of signal and vertical resolution). These metrics quantify the information content of the observation vector and depicts where this information is used in the retrieval. Next, the convection indices are calculated from the AERIoe retrievals and radiosondes to compare their individual assessments of conditional instability. The program used for making these calculations is discussed in Section 5.2.1. In the final section, the uncertainties from both the radiosonde profiles and AERIoe retrievals are used quantify the uncertainties of indices such as CAPE.

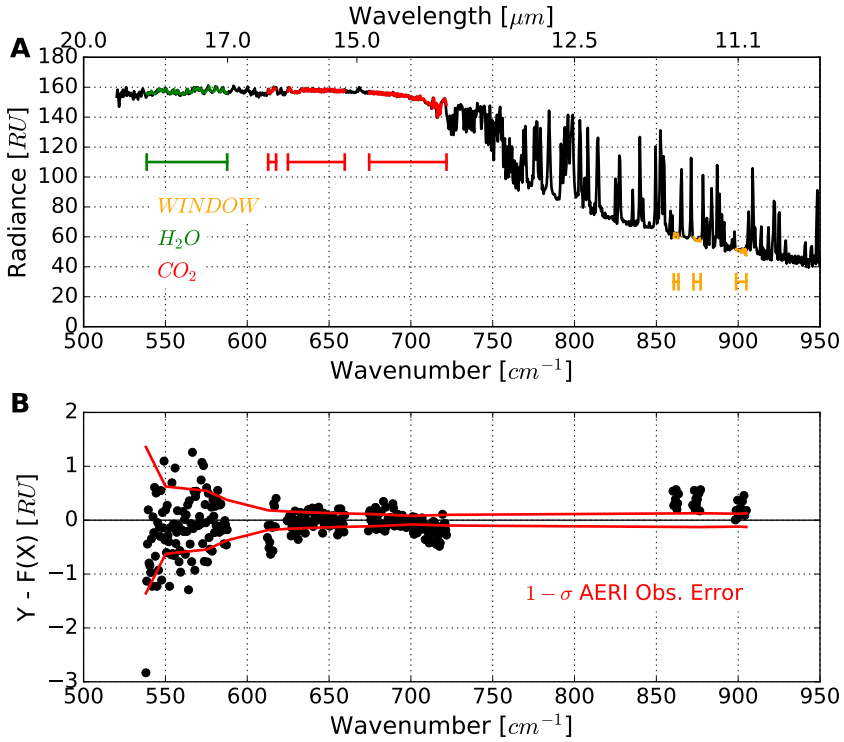

Figure 5.1: Sample AERI spectra from Blumberg et al. (2017b) with portions of the spectra used in the AERIoe retrieval highlighted in orange, green, and red colors. (b) The residuals between the observed AERI spectra and the spectra calculated using the LBLRTM for a sample retrieved profile. The red lines in (b) indicate the AERI $1-\sigma$ observational error assumed in AERIoe. Here, 1 RU = 1 $mW\,/\,(m^2\,sr\,cm^{-1})$

Table 5.1: Observations utilized in the AERIoe $\mathbf{y}$ vector for this study. The noise values for the AERI channels are listed in (Turner and Löhnert 2014; Blumberg et al. 2015). 1-σ errors for the Raman lidar are derived directly from Poisson statistics from the detected photon counts.

AERI	RLID	MET	RAP
538-588 cm^{-1}			
612-618 cm^{-1}			
624-660 cm^{-1}			
674-713 cm^{-1}	$T(z)$ (z=2-4 km)	z=2 m AGL	z = 4-12 km AGL
713-722 cm^{-1}	$q_v(z)$ (z=0.3-3 km)	σ_T = 5 K	σ_T = 1 °C
860.1-864.0 cm^{-1}		σ_{q_v} = 0.7 g/kg	
872.2-877.5 cm^{-1}			
898.2-905.4 cm^{-1}			

5.1 Retrieval Accuracy and Information Content

The plots within Figure 5.2 provide a look at where in the vertical AERIoe is able to use certain observation types. Two metrics are shown: the cumulative DFS and the vertical resolution. On the left panel of Figure 5.2, the cumulative DFS rapidly increases with height in the lowest 2 km for both the retrieved temperature and water vapor profiles. The temperature cumulative DFS shows the DFS is roughly 6 at 2 km AGL; above this point the slope of the median line changes. There, the retrieval is able to add roughly 1-2 more pieces of information from the observations to the retrieval in the 2-4 km layer, due to the information provided by the RLID temperature profile. In contrast, the water vapor cumulative DFS asymptotes at approximately 3 km AGL between 9-15 DFS, where the RLID water vapor profile is no longer provided as an observation to AERIoe. This limit indicates that the observations used in these retrievals have little to no information about the water vapor profile above 3 km, which makes sense given the vertical extent the RLID q_v data is used. However, for the temperature profile, the cumulative DFS continues to increase past 4 km, as AERIoe is provided the RAP temperature data to solve for the mid-to-upper atmospheric temperature profile. Although the AERIoe can use RAP water vapor profile data in a similar manner, it is not used in these experiments. This is primarily because the area of interest for this study is in the PBL, where the RLID data is being used.

The vertical resolution plot in Figure 5.2 also provides additional information about where the data in the AERIoe observation vector ($\mathbf{y}$) is used. Below 3-km, the vertical resolution of the water vapor profile typically is on the order of 100-400 m, with a spike at 300-m where AERIoe begins to use the RLID q_v data.

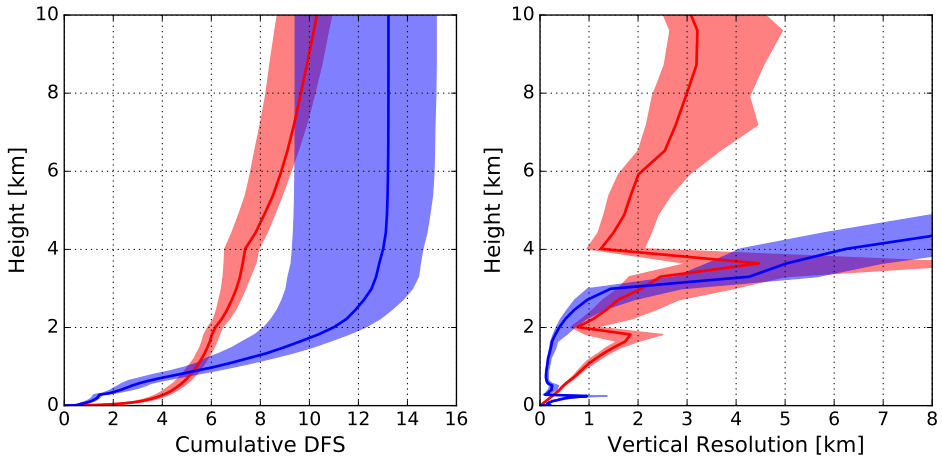

Figure 5.2: Plots showing the cumulative degrees of freedom of signal (DFS) on the left and the vertical resolution (right) from the AERIoe-retrievals. Blue indicates the statistics for the water vapor profile, while the red indicates the statistics for the temperature profile. The shaded area indicates the 25-75th percentile of the statistic, and the solid line represents the median value (n=182).

Above 3 km, the vertical resolution for the water vapor profile rapidly degrades. This result is similar to the vertical resolution results in Blumberg et al. (2015), but not in Turner and Löhnert (2014). This is due to the fact that the method of calculating vertical resolution was changed between Blumberg et al. (2015) and Turner and Löhnert (2014). For the temperature vertical resolution, three distinct regimes show up that are separated by rapid changes in the vertical resolution. Between the surface and 2 km, where the information within the AERI spectra contributes most to the retrieved profile (Turner and Löhnert 2014), the vertical resolution increases from 0 to nearly 2 km. Above 2 km, the resolution jumps back to 1 km and increases to 4 km. Here, as mentioned in the previous paragraph, the Raman lidar temperature data is providing information. Finally, a final jump back to nearly 1 km at 4 km indicates where the RAP temperature information begins to be used in AERIoe.

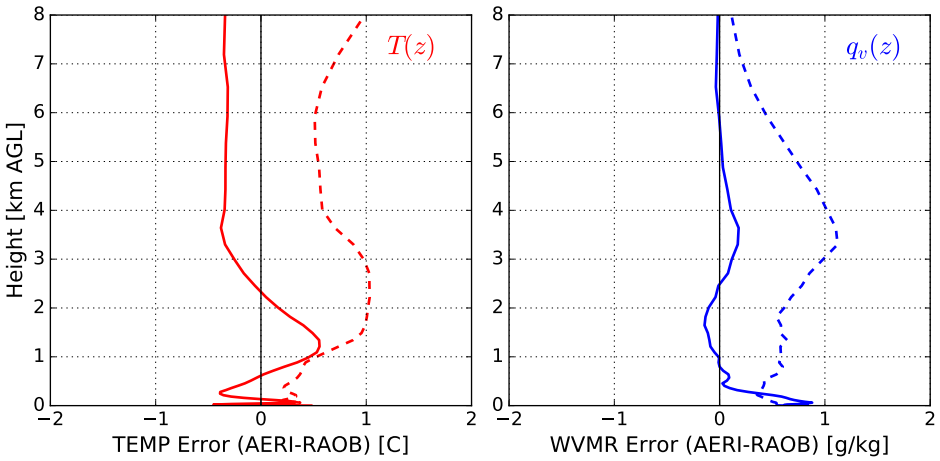

Figure 5.3: Bias (solid) and standard deviation (dashed; STD) for AERIoe-retrieved temperature (red) and water vapor (blue) compared to the profiles obtained from co-located radiosonde launches (n=182).

Figure 5.3 shows the bias and 1-sigma standard deviation (STD) of profiles retrieved from AERIoe compared to their co-located radiosonde observations. For the temperature profile, the bias of the entire profile does not exceed 0.5 °C from the surface to 8 km. The only noticeable bias is a warm bias peaking at approximately 1.2 km, which is consistent with past studies analyzing AERIoe retrievals (Turner and Löhnert 2014). Likewise, above 1 km, the STD for temperature increases to nearly 1 °C from roughly 0.3 °C. Above 3 km, the STD for temperature reduces to 0.5 °C until the profile reaches 7 km AGL. Above this point, the STD increases. For the water vapor profile retrieved from AERIoe, the lowest 300-m of the atmosphere nearly exhibits a 1 g/kg moist bias. Above 300-m, the water vapor profile is generally unbiased. Similar to the pattern indicated by the temperature STD profile, the water vapor STD profile exhibits a maxima aloft. However, unlike temperature, this peak occurs just above 3 km AGL. Below this maxima, the water vapor STD is approximately 0.5 g/kg. Above this maxima, the water vapor STD decreases with height.

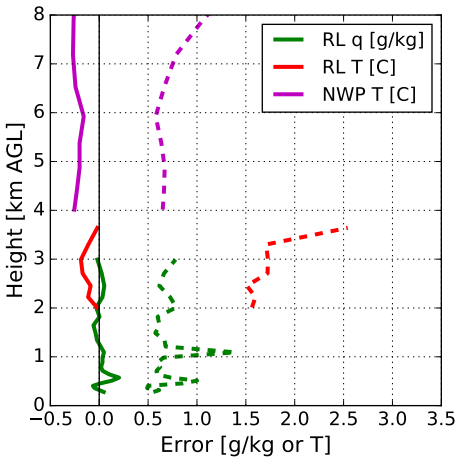

Figure 5.4: Bias (solid) and standard deviation (dashed) for profiles input into AERIoe. The profiles included are the Raman lidar water vapor profile (green), the Raman lidar temperature profile (red), and the RAP temperature profile (magenta) (n=182).

Most of the statistics from Figure 5.3 can be explained by looking at the accuracy of the profiles input into AERIoe. Figure 5.4 shows the bias and STD for the Raman lidar water vapor profile, the Raman lidar temperature profile, and the RAP temperature profile. Above 4 km, where the RAP temperature profile is used in AERIoe, the AERIoe retrieval adopts a similar cold bias and STD value. Similarly, as the Raman lidar water vapor profile is both largely unbiased and the STD remains roughly around 0.7 g/kg, the AERIoe retrieval largely adopts these characteristics within the 300-m to 3000-m AGL layer shown in Figure 5.3. As the Raman lidar temperature data has such a small cold bias and is used over only a 2 km layer, its bias does not appear as easily in the AERIoe retrieval. Overall, the statistics shown in Figure 5.3 compare well to those in Figure 4.2. These sources of data outside the traditional AERI spectra strongly influence the AERIoe retrievals. The small biases such as those from

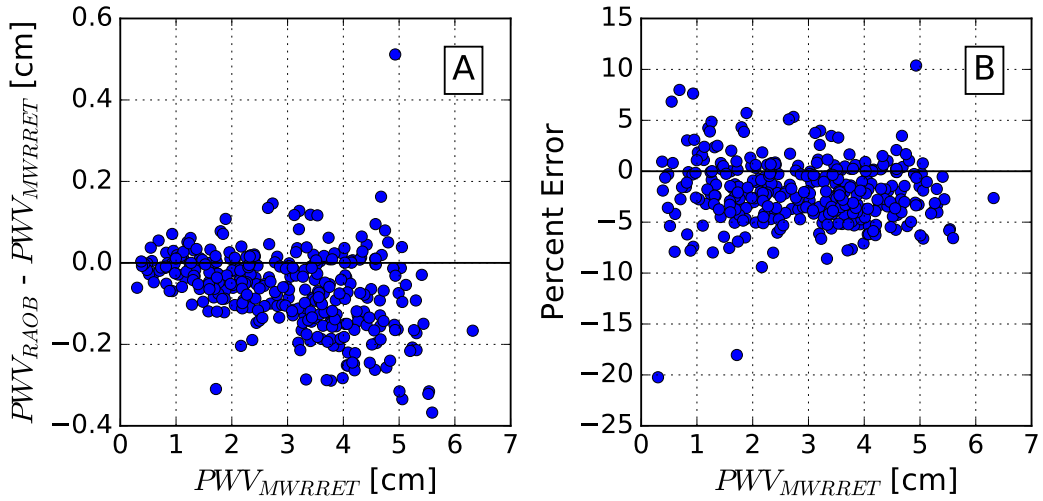

Figure 5.5: A comparison between precipitable water vapor (PWV) derived from radiosondes (PWV_{RAOB}) and MWRRET PWV_{MWRRET}. Plots A and B are the difference and the percent error for the two PWV estimates, respectively. Each point indicates a 23 UTC RAOB and MWRRET comparison. The x-axis indicates the difference between the RAOB and MWRRET PWV values. (n=350).

the Raman lidar data is beneficial to AERIoe as the OE framework assumes no systematic errors in the observations and forward models.

However, there are characteristics within the AERIoe profiles that are not attributable to the RLID or NWP data. Most obvious are the changes in the sign of the AERIoe temperature biases in the lowest 100-m and the nearly 1 g/kg moisture bias in the lowest 300-m of the water vapor profile (Figure 5.3). Although AERIoe does identify superadiabatic layers correctly in the temperature profile, the near-surface profiles just above these layers can display shallow (approximately 30 m deep) isothermal features that are not present within radiosonde observations of the mixed-layer. These features also were apparent in some of the daytime profiles in AERIoe retrievals using older AERI technology Blumberg et al. (2017b), however their presence did not impact assessments of parcel instability compared to radiosondes. The low-level moist

bias however, did not appear in the Blumberg et al. (2017b) profiles. These biases instead may be attributable to spectroscopy errors within the LBLRTM or incorrect modeling of AERI instrument characteristics.

An alternative hypothesis for the bias in q_v is that it may be related to systematic errors in the moisture sensor of the radiosondes. As radiosondes are used as the calibration standard for the RLID q_v profiles, systematic errors in the radiosondes will be carried to the RLID q_v profiles; fail to meet the assumption in the OE-framework that observations are unbiased. To test for this, precipitable water vapor (PWV) calculated from all 23 UTC radiosondes from March-August 2016-2017 was compared to PWV retrievals from MWRRET, an OE-type retrieval algorithm for microwave radiometers (Turner et al. 2004; Turner 2007). The results from this comparison are shown in Figure 5.5.

Apparent in Figure 5.5 is that the RS-92 radiosondes exhibit a dry bias in wet environments ($PWV > 3.5$ cm). This is roughly a 3-5% error. Given that this means the RLID q_v profile also exhibits a dry bias, it is possible that the low-level moist bias in the AERIoe retrievals is an attempt by AERIoe to resolve inconsistencies between precise, yet dry RLID profiles and AERI spectra that suggests that the troposphere should contain more water vapor than the RLID profiles would suggest. While further investigation and resolution of this bias is possible, the research questions addressed in this dissertation do not require it. Inspection of AERIoe retrievals during the AET suggest that this bias does not change with time. Given this fact and that this study's focus on the time derivative of moisture suggests that this bias will not significantly impact the conclusions of this research.

Although the bias and standard deviation metrics can help characterize random and systematic errors at each height in the profile, Taylor diagrams (Taylor 2001) can help understand how well the AERIoe-retrieval profiles match the thermodynamic structures inherent in radiosonde profiles. Taylor diagrams show the correlation coefficient between the AERIoe and radiosonde profiles on the y-axis and the ratio of the standard deviation from each profile on the x-axis. Each point indicates an individual case where the AERIoe retrieval and radiosonde profiles were present. An AERIoe retrieval that reproduces the radiosonde structures within the lowest 2 km perfectly would be found on the (1,1) point on the diagram. Taylor diagrams have been used in Blumberg (2013),Turner and Löhnert (2014), and Blumberg et al. (2015) to assess the quality of AERI retrievals.

Figure 5.6 shows the Taylor diagram for the AERIoe temperature and water vapor profiles. The clustering of the points near the (1,1) point for the temperature retrieval indicates that the AERIoe retrieval does an excellent job of reproducing structures present in the lowest 2-km of the profile. The water vapor profiles also cluster around the (1,1) point, but they do exhibit more scatter than the temperature profiles. Part of this loss in skill is due to the moist bias in the lowest 300-m of the profile. However, the inclusion of the RLID in the AERIoe retrievals improves the Taylor diagram statistics for the q_v profile compared to those in past studies (Turner and Löhnert 2014; Blumberg et al. 2015).

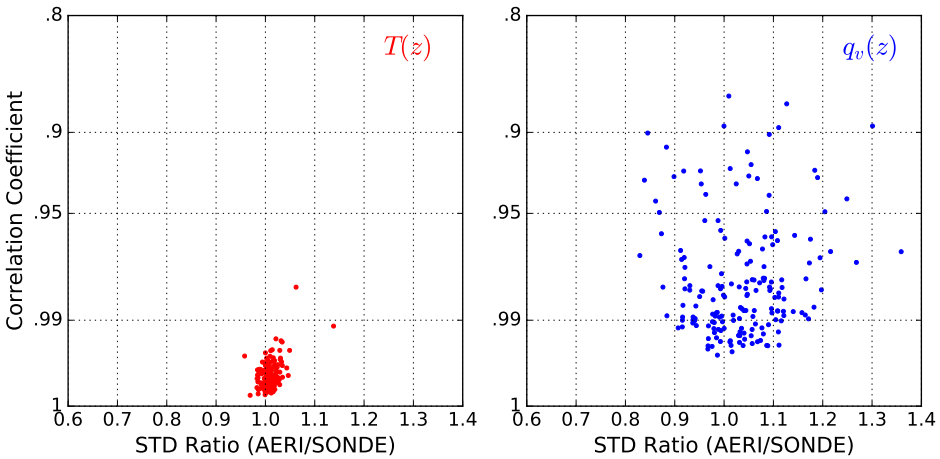

Figure 5.6: Taylor plots for the AERIoe-retrieved temperature (red) and water vapor (blue) compared to the profiles obtained from co-located radiosonde launches. Portions of the vertical profile used in this analysis are between the surface and 2 km AGL (n=182).

5.2 Verification of AERIoe Convection Indices

As the profiles retrieved from AERIoe will be used in assessing changes in parcel stability throughout the evening transition to test **H2**, it is important to compare how metrics of parcel stability compare to those from co-located radiosondes. In order to perform this comparison, convection indicies derived from the All AERIoe cloud-free AERIoe retrievals derived in the processing steps explained in the last section are compared regardless of the availability of data. The analysis performed in this section is similar to the one performed in Blumberg et al. (2017b).

In this section, two comparisons of convection indices between radiosondes and AERIoe profiles will be made. First, comparisons of deterministic convection indices determined from each observation framework will be compared. Second, the uncertainty of the indices from each observation type will be compared. This test considers convection indices in a probabilistic sense (Moller et al. 1994) and seeks to determine whether if AERIoe retrievals or radiosondes offer more precise diagnoses of parcel stability. This will be accomplished by using Monte-Carlo sampling profiles to generate 500 profiles that lie within the error bounds of the each observation. The equation for calculating the Monte Carlo sampled profile $\hat{\mathbf{X}}$:

$$\hat{\mathbf{X}} = \mathbf{S^{1/2}Z} + \mathbf{X} \tag{5.1}$$

uses the profile's error covariance matrix $\mathbf{S}$, a normally distributed random number vector $\mathbf{Z}$, and the original profile $\mathbf{X}$. Parcels are then lifted in each Monte Carlo sampled profile using SHARPpy (Blumberg et al. 2017b), therefore generating a distribution of convection indices.

For radiosondes, the covariance matrix **S** is generated by considering two types of errors in RS-92 radiosonde observations: 1.) repeatability errors (random errors: $s_{RH} = 1.41\%$ RH, $s_T = 0.398$ °C) and 2.) reproducibility errors (systematic errors: $s_{RH} = 3\%$ RH, $s_T = 0.28$ °C). Each radiosonde profile was perturbed by adding one randomly chosen systematic error value and a random noise profile. The perturbation chosen were applied independently to the profiles of temperature and relative humidity. Once the set of perturbed $T(z)$, $RH(z)$ profiles was computed, they were used to calculate perturbed profiles of water vapor mixing ratio. Finally, a covariance matrix **S** was calculated using the $T(z)$ and new $q_v(z)$ profiles. This matrix contains off-diagonal values as the assumed uncorrelated errors in T and RH create correlated errors when q_v is calculated given q_v is dependent upon T and RH.

5.2.1 SHARPpy

SHARPpy, or the Sounding and Hodograph Analysis and Research Program in Python, is an open-source, Python implementation of the historical sounding analysis program called SHARP (Hart and Korotky 1991). The development of SHARPpy was motivated by various investigations that revealed that when sounding data is run using different sounding analysis programs, noticeable differences in the results appear. For example, different sounding analysis programs may give different values of CAPE (Marsh and Hart 2012). A quick search using Google Scholar reveals that the workstation manual for SHARP has been cited over 150 times. While the below text summarizes the relevant parts of the SHARPpy program for this research, more information can be found in Halbert et al. (2015) and Blumberg et al. (2017a).

SHARPpy takes in thermodynamic and kinematic profiles and can calculate the properties of lifted parcels from them. Parcels that are lifted from locations in the environmental profile are defined as having an origination height called z_i. Parcel properties, such as the initial parcel virtual temperature $T_{v,parcel}(z_i)$ can be derived (Doswell and Rasmussen 1994). Three common parcel types are used in this study, called the 100-mb mean-layer (ML), the surface-based (SB), and the most-unstable (MU). The equations for $CAPE$, CIN, and LI_5 calculated using SHARPpy are shown below:

$$CAPE = \int_{z_i}^{EL} g \left(\frac{T_{v,parcel}(z) - T_{v,env}(z)}{T_{v,env}(z)} \right) dz \tag{5.2}$$

$$CIN = \int_{z_i}^{LFC} g \left(\frac{T_{v,parcel}(z) - T_{v,env}(z)}{T_{v,env}(z)} \right) dz \tag{5.3}$$

$$LI_5 = T_{v,parcel}(p = 500mb) - T_{v,env}(p = 500mb) \tag{5.4}$$

Here, EL corresponds to the equilibrium level, LFC to the level of free convection, and g to Earth's gravitational constant (9.81 m/s^2). In cases where no level of free convection (LFC) exists, both CIN and $CAPE$ are set to 0.

SHARPpy has also had the buoyancy minimum B_{min} index added to its set of indices (Trier et al. 2014a,b, 2015). B_{min} is calculated by finding the location where an ascending parcel reaches its global minimum in buoyancy:

$$B_{min} = min(T_{v,parcel}(z) - T_{v,env}(z)), \tag{5.5}$$

where B_{min} provides similar information to CIN in that it estimates how resistant the environmental profile will be to ascending parcels. In contrast to CIN,

B_{min} can be computed even if a parcel does not have a level of free convection (LFC).

Because repeated parcel lifting of the Monte Carlo sampled profiles can become computationally expensive, a modification was made to SHARPpy to both improve the accuracy and speed of pseudoadiabatic calculations. During the course of this work, SHARPpy's method of lifting saturated parcels was upgraded using the method outlined in Davies-Jones (2008). In Davies-Jones (2008), the wetbulb temperature is calculated through an accelerated iterative algorithm that inverts the equation for equivalent potential temperature derived in Bolton (1980). This newer method is more computationally efficient and more accurate than the Wobus method that is currently used in SHARP/SHARPpy (Doswell 1987). Figure 5.7 shows how the Davies-Jones (2008) method is faster than the Wobus method yet still maintains similar CAPE and CIN values.

5.2.2 Comparison of Convection Indices

Figure 5.8 shows the comparison between the 23 UTC clear-sky AERI retrievals and the radiosondes for the indices: CAPE , CIN , B_{min}, LI_5, and the location of the buoyancy minimum ($B_{MINHGHT}$). Table 5.2 lists statistics relevant to understanding how well the AERI retrievals reproduce the indices computed from the co-located radiosonde measurements. On average, AERIoe CAPE measurements tend to be greater than radiosonde CAPE measurements by roughly 200-300 J/kg. This overestimation in parcel instability is mirrored in the roughly 1 C biases shown for the LI_5 index. The random errors (denoted by the $1-\sigma$ standard deviation or STD) of these CAPE measurements range between 200-400 J/kg and between 1.1 and 1.5 °C for LI_5. Per the bias

and STD metrics for CAPE and LI_5 in Table 5.2, the AERI ML parcel tends to compare the most favorably with the radiosonde ML parcel. Although the NSTD suggests that the AERI retrievals are more accurate at retrieving LI_5 than CAPE (0.17-0.26 vs 0.26-0.31), AERIoe performs best at retrieving these two indices.

Table 5.2 and Figure 5.8 reinforce the conclusion found in Blumberg et al. (2017b): AERIoe compares more favorably to radiosondes when using the B_{min} index than the CIN index. For this dataset, AERIoe tends to exhibit parcels that are slightly less restricted by negatively buoyant layers in the atmosphere. This is evident by the positive biases in CIN and B_{min} in Table 5.2. Blumberg et al. (2017b) found biases (approx. 10 J/kg and 0.1-1 C) and STD (approx. 50 J/kg and 1-2 C) of the same order of magnitude as the statistics in Table 5.2. Most notable Table 5.2 are the differences in NSTD between CIN and B_{min}. For both the SB and ML parcels, the NSTD between the two are roughly 0.57 and 0.17, respectively. For the MU parcel however, the NSTD for B_{min} is slightly greater than that for CIN.

The final index in this section, the $B_{MINHGHT}$ indicates the location of where B_{min} is found. Per Table 5.2, AERIoe struggles to reproducing the same $B_{MINHGHT}$ location as the radiosonde. AERIoe $B_{MINHGHT}$ for all parcel types is typically found nearly 1 km lower than the radiosonde. The STD is also generally found to be 1 km, as well. These larger errors are partially due to the fact that while two profiles may generally have identical shapes, subtle differences in weakly capped environments (where B_{min} 0) create large errors. In these environments, one profile's $B_{MINHGHT}$ to be found at the origination height z_0, while the other profile's $B_{MINHGHT}$ may be found at the capping

Table 5.2: The verification statistics for different median thermodynamic indices: CIN (J/kg), CAPE (J/kg), B_{min} (°C), LI_5 (°C), and B_{min} height (km). Shown are the number of data points n, bias, STD of the error, and the Normalized STD (NSTD). NSTD is the ratio of STD to the 1-sigma STD calculated using all the radiosonde indices for that index. Only profiles where the radiosonde parcel being evaluated had a $CAPE > 100$ J/kg and a $CIN > -800$ J/kg were used in the CIN comparisons to ensure that the radiosonde had a nonzero value of CIN and CAPE. Caption is reproduced from Blumberg et al. (2017b).

Index Name	n	Bias	STD	NSTD
SB $CAPE$	231	325.7	396.4	0.31
SB CIN	143	18.1	48.3	0.57
SB B_{min}	231	0.9	1.3	0.33
SB LI_5	231	-1.2	1.2	0.18
SB $B_{MINHGHT}$	231	-0.8	0.9	0.65
ML $CAPE$	231	184.9	234.5	0.26
ML CIN	114	8.7	52.4	0.59
ML B_{min}	231	0.6	1.3	0.32
ML LI_5	231	-0.88	1.1	0.17
ML $B_{MINHGHT}$	231	-0.9	0.9	0.70
MU $CAPE$	231	330.1	399.3	0.31
MU CIN	148	16.9	44.9	0.60
MU B_{min}	231	0.7	1.9	0.68
MU LI_5	231	-1.2	1.5	0.26
MU $B_{MINHGHT}$	231	-0.7	1.1	0.74

inversion. Some of these cases are found when the AERIoe $B_{MINHGHT} = 0$ and along the gray boundary in Figure 5.8. These errors suggest that profiles of buoyancy from AERIoe may be more useful when identifying if AET moisture jumps help parcels overcome any capping inversions.

5.2.3 Uncertainty of Convection Indices

The impact of random and systematic errors on the distribution of convection indices derived from AERIoe were also evaluated. As AERIoe retrievals will be used to identify if increases in conditional instability coincide with AET moisture jumps, understanding the error characteristics of the indices used to assess conditional instability is important. To do this, the IQR was computed using each distribution of convection indices generated via Monte Carlo sampling. Uncertainties were also computed using the 23 UTC radiosondes to act as a baseline comparison.

Figure 5.9 shows similar trends in the uncertainty of indices independent of parcel type and instrument. First, trends in LI_5 uncertainty across all parcels are either small or non-existent. In contrast, the uncertainty in CIN and B_{min} decreases as CIN and B_{min} increase. This signifies that there is less uncertainty in capping-related metrics when AERIoe and the radiosondes observe weakly capped environments than strong ones. This pattern is due to the presence of a upper bound of 0 for both CIN and B_{min}. This trend reverses for CAPE, and CAPE uncertainty increases as CAPE grows. These increases, however, are explained by considering how errors in $q_v(z)$ from each instrument are dependent upon q_v. For the SGP, large errors in q_v generally transfer into large errors in $CAPE$. For radiosondes, a 5% change in RH in an environment with high q_v

will create a much larger q_v error than if the same RH error was applied in a low q_v environment. For the AERIoe retrievals, uncertainty in q_v grows as PWV increases. Compared to low PWV environments, AERI observations taken in profiles with high PWV tend to be less transparent and therefore decrease the overall degrees of freedom of signal (DFS). While this explains the behavior of CAPE uncertainty trends, it does not explain all of the differences apparent in Figure 5.9.

Figure 5.9 shows some interesting behavior of the ML parcel that was not seen in Blumberg et al. (2017b). In these tests, all AERI-based indices derived from the ML parcel tended to exhibit less uncertainty than those derived from the SB or MU parcel. This pattern does not occur with indices derived from radiosondes. These differences are explained through key differences in the error covariance matrices used in the Monte Carlo sampling step (Figure 5.10). When creating the radiosonde error covariance matrix, the inclusion of systematic errors creates level-to-level correlated errors. In contrast, the inclusion of RLID q_v data in AERIoe results in retrievals with practically no correlated errors between levels. When the 100-mb average is taken to construct the ML parcel properties, the averaging suppresses errors in the AERIoe more effectively than the radiosonde, as the AERIoe retrieval covariance matrix has less correlated errors than the radiosonde. When computing the SB and MU parcel, no modification is made to the uncertainties of the parcel's initial properties (e.g., $T(z_0), q_v(z_0), p(z_0)$), and therefore there are no substantial differences in the uncertainties of indices derived using these two parcel types. Because Blumberg et al. (2017b) did not use RLID data in their retrievals, this overall behavior was not seen.

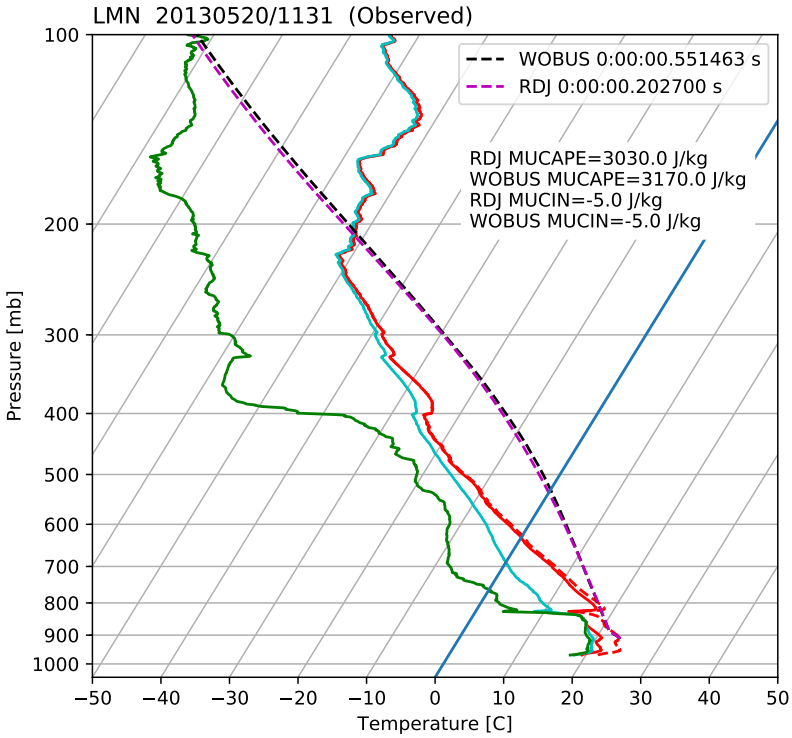

Figure 5.7: An example of the different lifting routines in SHARPpy. The profile is from the ARM site and was launched on May 20th, 2013 at 11:31 UTC. Red represents the temperature trace, green the dewpoint trace, and dashed red the virtual temperature trace. In the legend are the different parcel traces (RDJ; Davies-Jones (2008) and WOBUS; Doswell (1987)) along with the speed in seconds.

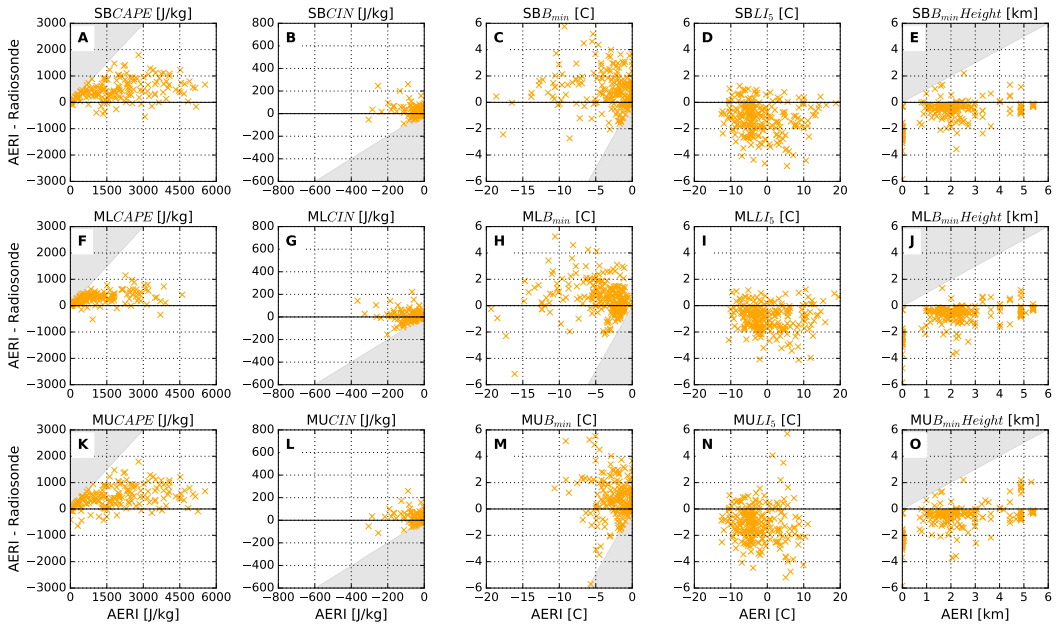

Figure 5.8: Error plots for thermodynamic indices (a, f, k) CAPE (J/kg), (b, g, l) CIN (J/kg), (c, h, m) B_{min} (°C), (d, i, n) LI_5 (°C), and (e, j, o) B_{min} height (km) for the (top) SB, (middle) ML, and (bottom) MU parcels. The y-axis represents the difference between the AERI and radiosonde index, while the x-axis represents AERI index value. Individual points indicate a single AERI-radiosonde comparison. The light gray shading in these plots represents the area where invalid bias values exist because of a lower or upper bound on the range of valid index values (for example, CAPE is nonnegative) (n=231).

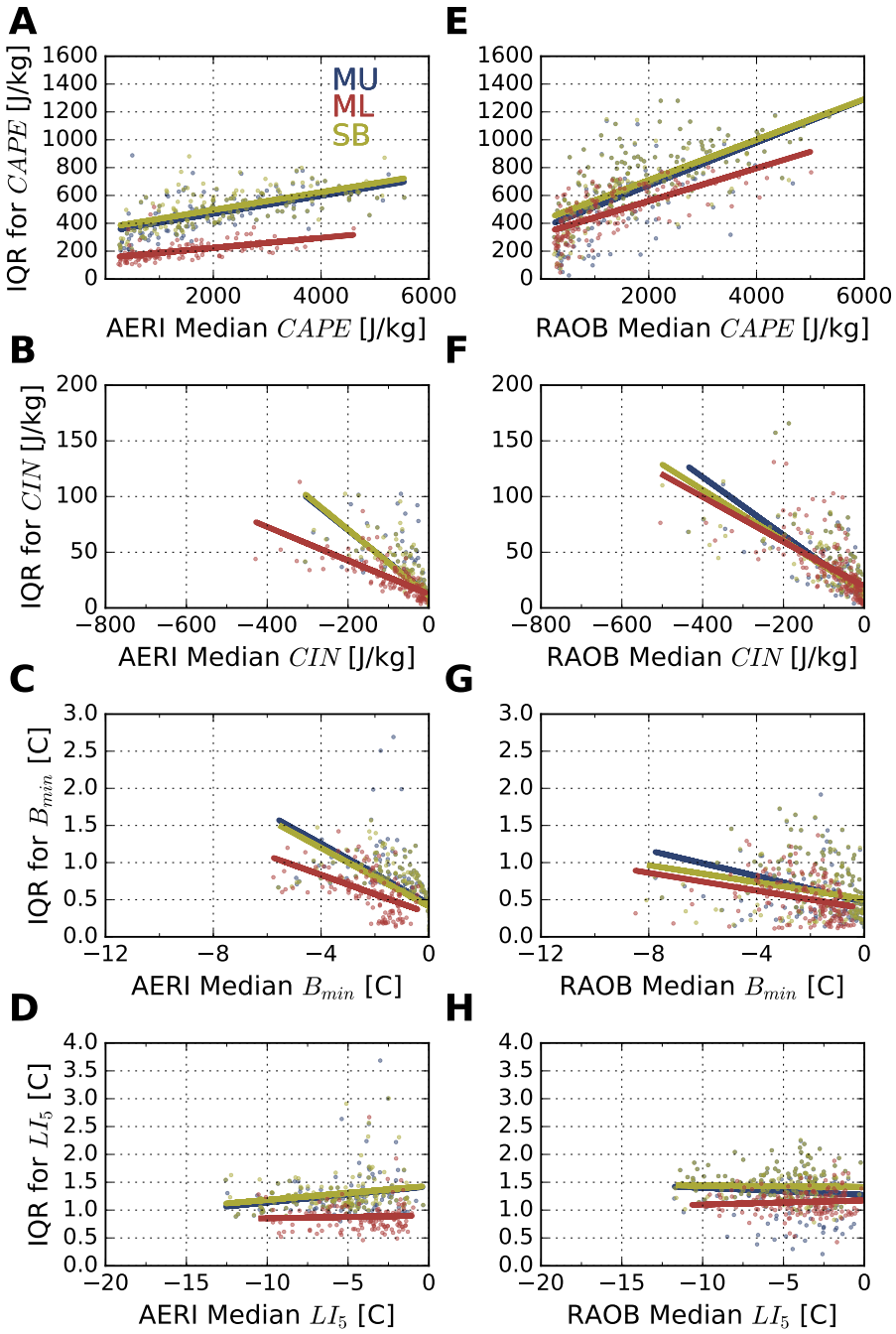

Figure 5.9: The impact of instrument random error on the calculation of the $CAPE$, CIN, B_{min}, and LI_5 indices using (a)–(d) AERI and (e)–(h) radiosonde profiles with $CAPE > 250$ (J/kg). The IQR of the index distribution is on the y axis, while the median value of the index is on the x axis. The points are colored by the type of parcel used to calculate the index (MU parcel: blue; ML parcel: red; SB parcel: yellow). Thick lines indicate the line of best fit to qualitatively show the trends for illustration purposes. Caption and figure are reproduced from Blumberg et al. (2017b).

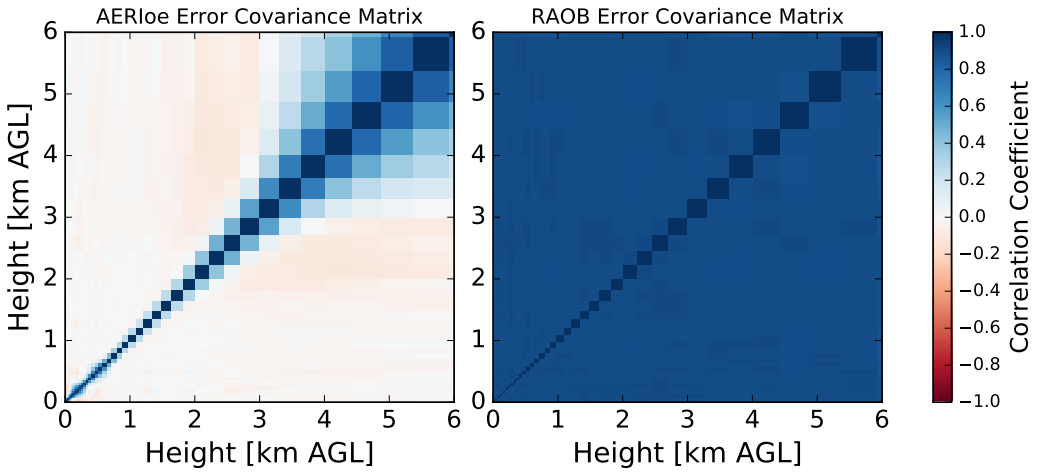

Figure 5.10: An comparison of the correlation matrices derived from the error covariance matrices for the AERIoe retrieval (left) and a co-located radiosonde (right).

Chapter 6

Lateral Evolution of Moisture

This investigation into the spatiotemporal changes in moisture during the SGP AET begins by using data from the Oklahoma Mesonet. Previous studies including Fitzjarrald and Lala (1989) and Acevedo and Fitzjarrald (2001) both established that during the AET, moisture tends to increase at a rate of 1 $g/kg/hr$ around sunset, just as the temperature begins to rapidly fall. As the presence of these moisture jumps have been established in New York (Fitzjarrald and Lala 1989; Acevedo and Fitzjarrald 2001) and Alabama (Busse and Knupp 2012; Wingo and Knupp 2015) through the literature, a natural first step is to see if similar increases occur in surface time series in the SGP. As mentioned before, the number of published cases observing the SGP AET are few (Bonin et al. 2013). To fill this knowledge gap, data collected over two decades by the Oklahoma Mesonet is used.

After identifying if these jumps occur, it is necessary to see what sort of dependence they have on season or location in the state of Oklahoma (**H1**). This includes tests to see if the jumps are sensitive to the land surface, as has been suggested by past studies. Finally, because these jumps manifest themselves as maxima in water vapor prior to sunset, Mesonet data will be used to test the idea that a maxima in water vapor can also create maxima in parcel instability prior to sunset (**H2**). In this final section, the sensitivity of these extrema in q_v to environmental conditions (e.g., cloud cover, soil moisture) are tested.

6.1 The Oklahoma Mesonet

The Oklahoma Mesonet is a network of 121 observing stations spread out across the state of Oklahoma at a spacing that can observe mesoscale phenomena. As of this writing, the Mesonet has been in operation for 26 years (since 1991) (Brock et al. 1995; McPherson et al. 2007). This network is currently managed by Oklahoma State University, the University of Oklahoma, and the Oklahoma Climatological Survey.

Each Mesonet station contains a variety of meteorological sensors located either on a 10-meter tower or embedded within the soil nearby. Temperature, relative humidity, and pressure sensors are located 1.5 m on the tower, while the wind is measured at 10-m. Additional sensors include a pyranometer to measure downwelling shortwave radiation, soil temperature, and moisture sensors. The sensors relevant to this study are listed in Table 6.1. The above ground sensors listed sample at a rate of one sample every three seconds (Brock et al. 1995; McPherson et al. 2007).

For this portion of the study, two decades of Mesonet observations are used (1994-2014) to analyze how moisture changes in Oklahoma during the AET. Only data from the months of March through August are used in this study, which results in a total of 3822 days/AET cases observed by the Oklahoma Mesonet. At least 114 sites are available for analysis in each AET case. Broken up by month, this data enables a little more than 600 cases available to analyze the AET in each month. The distribution of cases available for analysis is illustrated in Figure 6.1. Generally, data is available from all days in the two decades considered. No environmental filtering was performed on the data (e.g., removal of fronts).

Table 6.1: Variables reported by the Oklahoma Mesonet instruments by height z. The errors column represents the $1-\sigma$ errors for the 5-minute observations. Soil moisture is reported every 30 minutes.

z	Variable	Instrument	Error
1.5-m 9-m	Temperature (T)	Vaisala HMP35C Thermometrics Air Temperature	0.3 °C
1.5-m	RH (RH)	Vaisala HMP45C	0.2 - 0.3 %
1.5-m	Pressure (p)	Vaisala Barometer	0.04 mb
10-m	Wind Speed (WS)	RM Young Wind Monitor	0.3 m/s
10-m	Wind Direction (WD)	RM Young Wind Monitor	0.3°
1.75-m	Solar Radiation ($SRAD$)	LI200S Pyranometer	5%
-5-m -25 m -60 m	Temperature Rise (ΔT_{rise}) Fractional Water Index (FWI)	Campbell Scientific 229 - L	$\sim \pm 1$ °C N/A

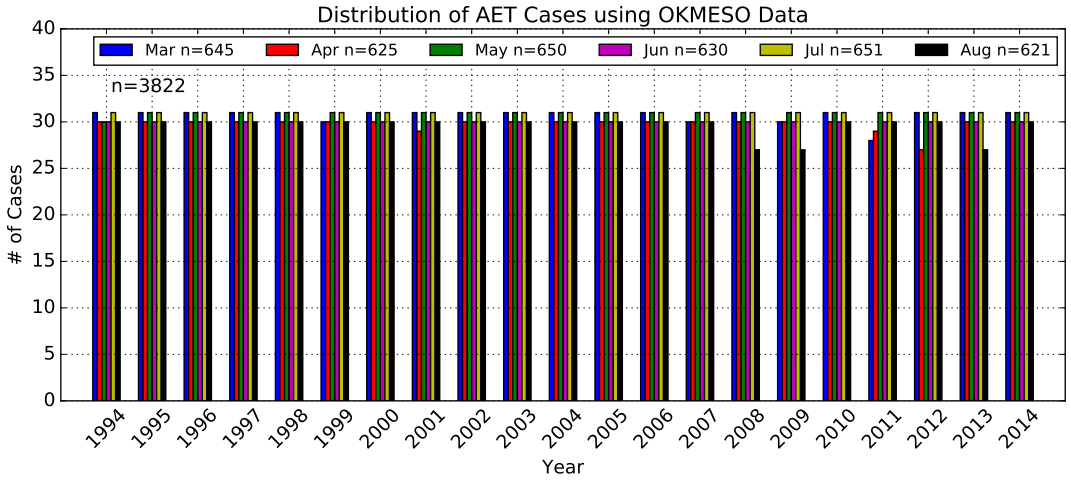

Figure 6.1: Distribution of AET cases from the Oklahoma Mesonet between 1994-2014 (n=3822).

For each AET observed by each Mesonet station, two steps are performed to prepare the data for analysis. In the first step, the time series from each Mesonet site was interpolated to a 5-minute, 6-hour temporal grid centered around local sunset. Local sunset in this study is defined as the time of astronomical sunset, and is computed by PyEphem, a Python package that runs astronomical algorithms (Rhodes 2011). Second, to compare against each observed time series of solar radiation, the expected incoming solar radiation for a cloud-free sky was calculated using a simple model (Stull 1988). This model calculates the downwelling shortwave radiation at the surface ($K\downarrow_s$) where the net sky transmissivity T_K is 1 for clear sky, and S is the solar irradiance of -1370 W/m^2 from Kyle et al. (1985):

$$K\downarrow_s = S \cdot T_K \cdot sin(\Psi). \tag{6.1}$$

The local solar elevation angle Ψ is calculated using Equation 7 in Zhang and Anthes (1982). For instances when Ψ is negative, the sun is below the horizon

and therefore $K\downarrow_s$ is set to 0 W/m^2. This model was used to develop a method of classifying the cloud cover of each AET during the 3-hour period prior to sunset so that the sensitivity of q_v jumps to cloud cover could be analyzed.

The method of classifying the AET cloud cover is similar to the AERI cloud detection algorithm described in Blumberg (2013). For each month, thirty randomly drawn Mesonet AET cases were selected to develop thresholds to classify the AET as clear sky, scattered clouds, or overcast. From each AET, all Mesonet stations were used, resulting in approximately 3000 data points for each cloud filter developed. For each AET time series, differences between the daytime (3 hours before sunset) theoretical and observed insolation were analyzed, and subjective thresholds based upon the variability of the differences ($log(\sigma_{SRAD})$) and the average differences ($AvgSRAD$) were determined. Figure 6.2 shows the result from this algorithm. AETs where $AvgSRAD$ and $log(\sigma_{SRAD})$ were low tended to be clear sky, whereas cases where the variability was high $log(\sigma_{SRAD})$, tended to have scattered clouds. AETs where $log(\sigma_{SRAD})$ and $AvgSRAD$ were both high tended to be AETs with overcast clouds.

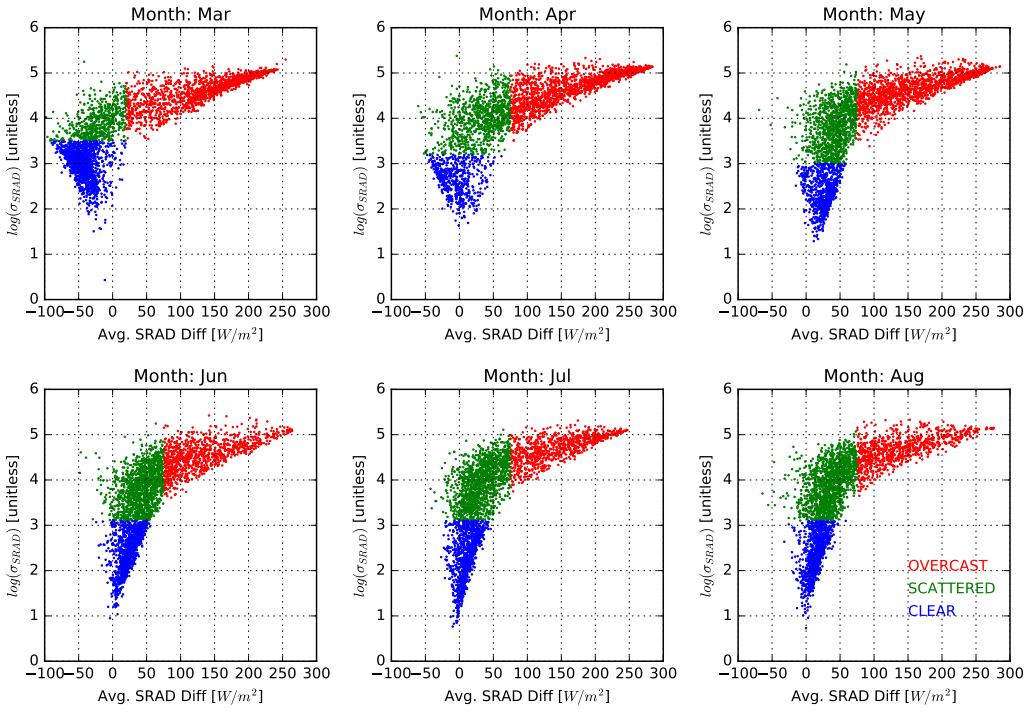

Figure 6.2: The AET cloud classification algorithm using the Oklahoma Mesonet SRAD variable showing the thresholds for clear (blue), scattered (green), and overcast (red) for the months of March-August. Average difference between the daytime theoretical and observed insolation is on the x-axis while the natural logarithm of the standard deviation of those differences is on the y-axis.

6.2 2D-VAR

To understand the spatial variability of moisture during the AET, Mesonet observations were also analyzed to a rectilinear grid using a two-dimensional variational analysis program (2D-VAR). The choice to use 2D-VAR was motivated by the work done in Spencer et al. (2003); Spencer and Gao (2004), which demonstrated that their 2D-VAR algorithm was able to more accurately analyze a scalar from observations better than multi-pass Barnes analysis schemes (Barnes 1964; Koch et al. 1983; Barnes 1994). Their method attempts to adhere to the Barnes (1994) suggestion that analyses should be judged by not

only how accurately they reproduce the scalar field, but also it's derivatives. By using derivative information contained in the observations, Spencer et al. (2003) argued that the analysis can be improved.

2D-VAR generates an 2D analysis of a scalar variable Z_v using observations of the scalar Z_o and "observations" of the gradient of the scalar $\frac{\partial Z_o}{\partial x}$ and $\frac{\partial Z_o}{\partial y}$. The 2D-VAR algorithm minimizes a cost function J that seeks to find the analysis that best fits both the scalar and gradient observations:

$$J = \int\int \left\{ [H(Z_v) - Z_o]^2 + \psi \left[H\left(\frac{\partial Z_v}{\partial x}\right) - \frac{\partial Z_o}{\partial x} \right]^2 + \psi \left[H\left(\frac{\partial Z_v}{\partial y}\right) - \frac{\partial Z_o}{\partial y} \right]^2 \right\} dxdy \tag{6.2}$$

where ψ is a weighting parameter that determines how much to weight the gradient observations compared to the scalar observations when minimizing J. H is a bilinear interpolation operator that acts to interpolate the analysis variables to observation locations. While J is minimized, a two-dimensional recursive filter is run in order to spread the information from each observation to nearby grid points (Gao et al. 2004). The recursive filter simulates isotropic Gaussian error correlations without requiring matrix inversion or development of an error covariance matrix (Purser et al. 2003).

In Spencer and Gao (2004), simulated observations taken from a truth analysis field were used to calibrate the 2D-VAR algorithm. From the observations a Delaunay triangulation was computed; this produces a tessellation of the observations. By using the set of triangles computed by the Delaunay triangulation that did not have an angle less than 15 deg, observations of $\frac{\partial Z_o}{\partial x}$ and $\frac{\partial Z_o}{\partial y}$ were calculated at the centroid of each triangle (the gradient observations). This filter by angle was put into the algorithm to avoid problems associated with the

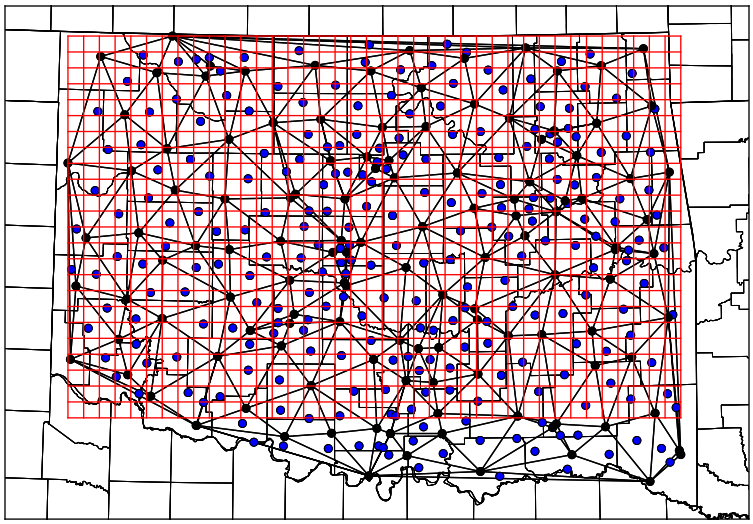

Figure 6.3: A map of the Oklahoma Mesonet observations (black points), the Delaunay triangulation using those data points (black lines), the gradient observations (blue dots), and the 2D-VAR grid (red lines) using a grid spacing of $\Delta x = 12$ km.

possible co-linearity of the triangle vertices. From the set of scalar and gradient observations, 2D-VAR was run several times, each time varying the ψ parameter. By determining the value of ψ that enabled 2D-VAR to best reproduce the truth analysis grid, they calibrated the 2D-VAR program.

For this study, 2D-VAR was calibrated in a similar way. In this calibration, 90 randomly selected 20 km Rapid Update Cycle (RUC, Benjamin et al. 2004) analyses from April 2002 to October 2003 were used as truth grids. These 90 grids were interpolated to a 12 km grid used in the 2D-VAR analysis (Figure 6.3). From these truth grids, observations of T, RH, p, wind speed, and wind direction at Mesonet sites were generated by bilinear interpolation. Mesonet stations located outside of the grid were not included in the analysis process. These observations were first perturbed by the $1 - \sigma$ errors described in Table 6.1. The resulting observations were then converted into q_v, u, and v. These three variables were used in 2D-VAR in the calibration step.

Figure 6.4 shows the results from calibrating 2D-VAR to optimize the accuracy of water vapor (q_v) analyses from Mesonet observations. As the Ψ parameter increases, the accuracy of the analysis changes very little until the parameter is equal to 10^8. Here, the accuracy of 2D-VAR in reproducing both the truth scalar field and its derivatives increases until Ψ reaches 10^{10}. When Ψ is increased further, the accuracy of the analyses stays constant with median errors of roughly 0.12 g/kg and 0.0040 g/kg/km. The optimum value of Ψ for the 2D-VAR using the Mesonet data is best shown in the bottom plot of Figure 6.4. There, the 2D-VAR analyses of water vapor advection are most accurate when Ψ equals 10^{11}, where the global minimum for the 1-σ standard deviation exists. In future runs of 2D-VAR discussed in this dissertation, this value of Ψ is used.

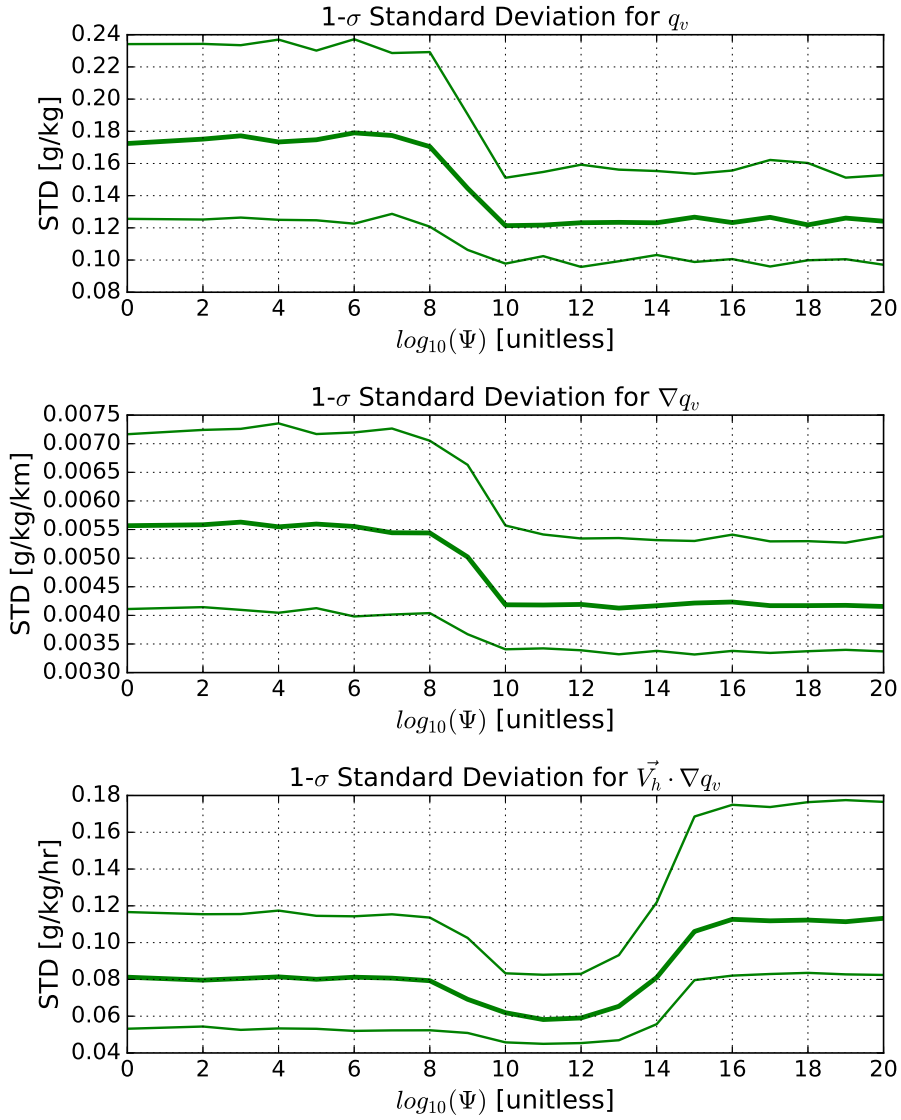

Figure 6.4: Figures showing the dependency of 2D-VAR accuracy on the Ψ parameter. The accuracy is measured by computing the 1-sigma standard deviation using the difference between the truth grid and the analyzed 2D-VAR grid. The top plot shows the accuracy for the q_v scalar field, the middle plot for the horizontal gradient of q_v, and the bottom plot for the water vapor advection. The thick line indicates the median standard deviation, while the thinner lines indicates the 25th to 75th percentile of the standard deviation metric.

6.3 Monthly Changes in Moisture

To test to see if jumps in moisture occurred in the Mesonet data, data were binned into monthly categories for each Mesonet site. From this data, a time series of changes to water vapor using the value occurring three hours prior to local sunset (defined as Δq_v) were calculated using the 6-hour, 5-minute grid time series centered on local sunset. From these time series, distributions of this change were constructed, following the analysis performed by Wingo and Knupp (2015).

Figure 6.5 shows results for this experiment using the Medford, OK Mesonet site located in northern Oklahoma. For the months of March to August, the surface q_v begins to increase approximately one to two hours prior to sunset, as evident by the shift of the median Δq_v towards positive values. More apparent though, is the trend that the magnitude of these increases shift to larger values as the year progresses. For example, the interquartile range of AET Δq_v shifts from spanning between -0.25 to 0.5 g/kg in March to ranging nearly 0 to 2.25 g/kg in August. This also suggests that a primary trend is that changes to q_v during the AET at the Medford site are stronger in the summer than in the spring. A final difference between these two seasons is that while both seasons show an increase in q_v prior to sunset, they differ on whether or not that increase continues after sunset. In the spring season, q_v tends to decrease after sunset. However, in the summer season, Δq_v tends to continue to increase in magnitude throughout the three hour period after sunset. Between the spring and the summer season the typical rate of increase of q_v during the AET can be estimated to be anywhere between 0.5 g/kg/hr to 1.5 g/kg/hr, which is

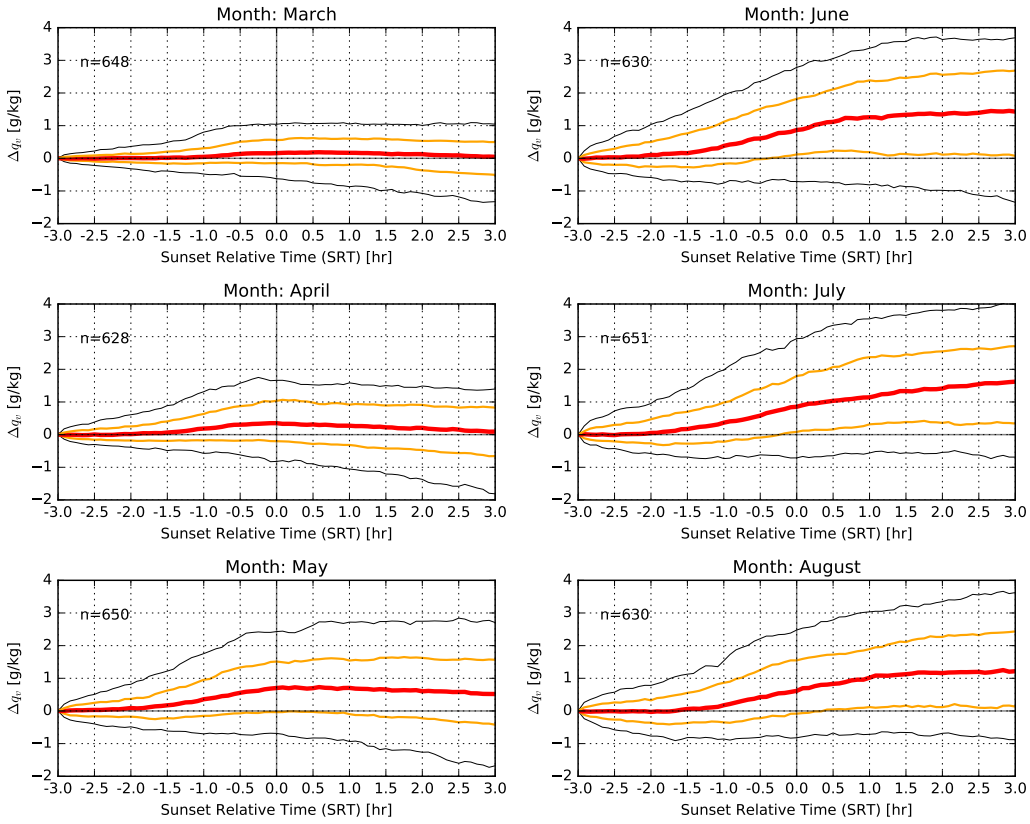

Figure 6.5: This distribution of changes of water vapor relative to the value three hours prior to sunset (Δq_v) for the Medford, OK Mesonet station. The distribution is identified by the red lines (the median), the orange lines (the 25-75 percentile) and the black lines (the 10-90th percentiles). Data is also broken up by month to illustrate how the distribution changes with the season with spring months in the left column and summer months on the right.

consistent with some of the more typical changes in q_v described in Fitzjarrald and Lala (1989) and Acevedo and Fitzjarrald (2001).

The results in Figure 6.5 have some key differences and similarities to findings that explain how q_v behaves during the northern Alabama AET (Busse and Knupp 2012; Wingo and Knupp 2015). First, the time frame in which the increases in q_v occur is roughly the same; Wingo and Knupp (2015) found that q_v increases began roughly 80 minutes prior to sunset on average. Similar to Wingo and Knupp (2015), this analysis found increases for q_v typically occurred

earlier in the day than the ones found in Busse and Knupp (2012) (90 minutes vs. 30 minutes prior to sunset). Second, both this study and Wingo and Knupp (2015) found that during the summertime months, both Alabama and Oklahoma exhibited similar magnitude changes in q_v (e.g., roughly a median change of 1.2 g/kg two hours after sunset). In addition, the summertime increases in both this study and Wingo and Knupp (2015) were the largest compared to the rest of the year. Lastly, a primary difference is apparent in the q_v changes that occur after sunset. As mentioned previously, Figure 6.5 shows that in the springtime, q_v tends to increase prior to sunset, but then decrease after sunset. This behavior was not observed in Wingo and Knupp (2015). Instead, their data suggested that q_v continues to increase after sunset, similar to the summertime trends visible in Figure 6.5. Wingo and Knupp (2015) attributed their post-sunset upward trend primarily to evaporation, as plants would no longer be transpiring due to photosynthesis. Although the general magnitude and timing of AET q_v increases seem consistent between northern Alabama and northern Oklahoma, differences are most apparent in what happens after sunset. While the water vapor stays stationary with time after sunset in northern Alabama, it increases with time after sunset in northern Oklahoma.

6.4 Spatial Changes in Moisture

In the previous section, the temporal changes at a single Mesonet site was analyzed to identify if changes in moisture occur during the AET and to build an expectation of the kind of patterns that can be hypothesized to occur spatially. In this section, the same method of analysis used in the previous section is applied to analyses of q_v generated using 2D-VAR. The data used is a subset

of the overall Mesonet data from 1998-2014. Using this data, the hypothesis that seasonal shifts in vegetation along the Great Plains Winter Wheat Belt (WWB) affects the location and extrema of water vapor during the AET is tested (Chapter 3, **H1**).

The land surface properties of the SGP evolve throughout the year in a predictable cycle. Bagley et al. (2017) described the SGP as being made up of 42% grassland/pasture and 43% cropland, of which 30% is winter wheat. While the grassland/pasture grows with the seasons, winter wheat grows in an opposite pattern. The winter wheat is typically planted in the fall and is harvested in late May and early June (McPherson et al. 2004; Haugland and Crawford 2005; Bagley et al. 2017). Figure 6.6 illustrates this cycle of the health of the winter wheat belt and the grasslands for the months of March through August. Because of this typical harvest time, months in this analysis between March to May are considered pre-winter wheat harvest months, while June through August are post-winter wheat harvest months. These drastic shifts in vegetation offers the ability to study how the land surface impacts AET moisture changes.

Figures 6.7, 6.8, and 6.9 show the distribution of the spatial change of q_v relative to the value three hours prior to sunset for the pre-harvest months. Similar to the results in the previous section, the distribution of changes to q_v suggests that the near-surface moistens throughout the AET. In addition, the distribution of the changes of moisture during the AET shifts in magnitude towards higher values as the months progress. For March, the median changes prior to sunset shifts from roughly 0.2 g/kg to 0.4 g/kg in April (Fig 6.7 and Fig 6.8). In May, the median changes reach their maximum of 0.6 g/kg (Fig

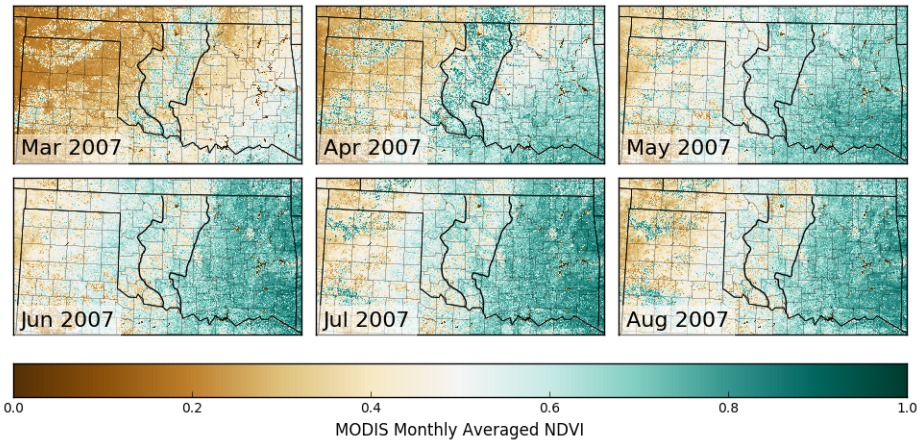

Figure 6.6: Monthly averages of MODIS-derived NDVI for Oklahoma and the Texas Panhandle from 2007 for the months of March through August. Black lines indicate the boundaries of the WWB from McPherson et al. (2004).

6.9). The 75th percentile changes also increase from March to May from 0.6 to roughly 1 g/kg.

The location of the moisture changes also shifts during the pre-harvest months. Prior to sunset, moisture tends to accumulate along the WWB. After sunset, moisture increases occur west of the WWB. These increases are best illustrated in the March and April figures (6.7 and 6.8), where the moisture change distribution shifts towards moister values just west of the WWB boundary one hour after sunset. However, east of the WWB, the magnitude of the median pre-sunset moisture changes increase as the months shift from March to May. In March, the median change is actually slightly negative east of the WWB where the vegetation is not as active (Fig 6.6). In accordance with the growth of vegetation east of the WWB in May and April, the median change in water vapor during the AET increases. Given the changes in vegetation apparent in Figure 6.6 for these months, these results suggest that there is a dependence of AET moisture changes on vegetation location and health.

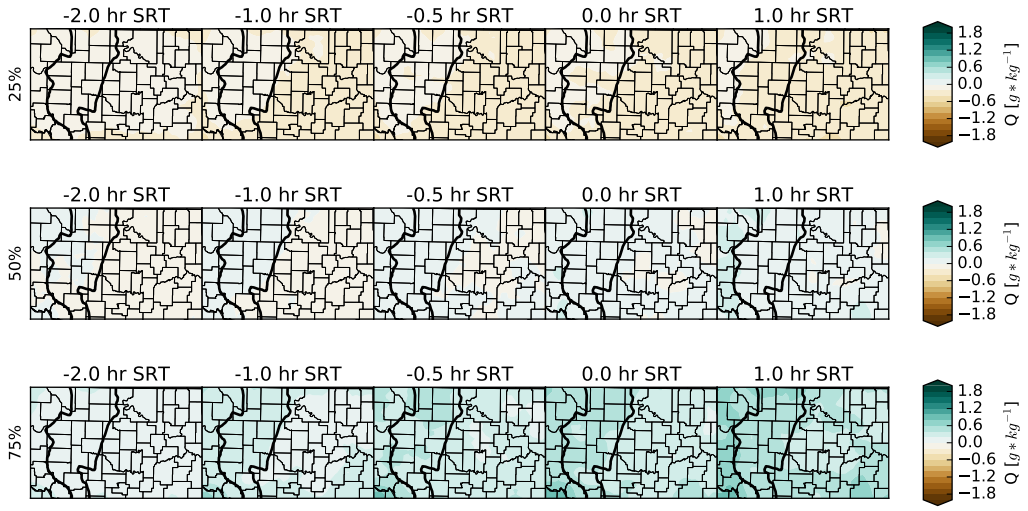

Figure 6.7: Spatial changes in moisture relative to the moisture value 3-hours prior to sunset using March 2D-VAR analyses (n=503; 1998-2014). Rows correspond to the 25th, 50th, and 75th percentile changes of the water vapor, while columns refer to the time of the map in sunset relative time (SRT). The black lines indicate the outline of the winter wheat belt from McPherson et al. (2004).

These above descriptions suggest that AET moisture increases no longer occur along the harvested WWB. In fact, Figures 6.10, 6.11, and 6.12 show that summertime increases in q_v do occur along the WWB, but they primarily occur after sunset, similar to the summertime increases indicated in Figure 6.5. These post-sunset increases are quite apparent in June and July in the northern portion of the WWB (Figures 6.10, 6.11). The timing of these post-sunset increases suggests that processes other than the decay of turbulence may be playing a role in changing the near-surface moisture properties of the WWB. Regardless, these results support the idea that the evolution of moisture during the AET is dependent upon the land surface properties, and more specifically, the distribution and life-cycle of vegetation.

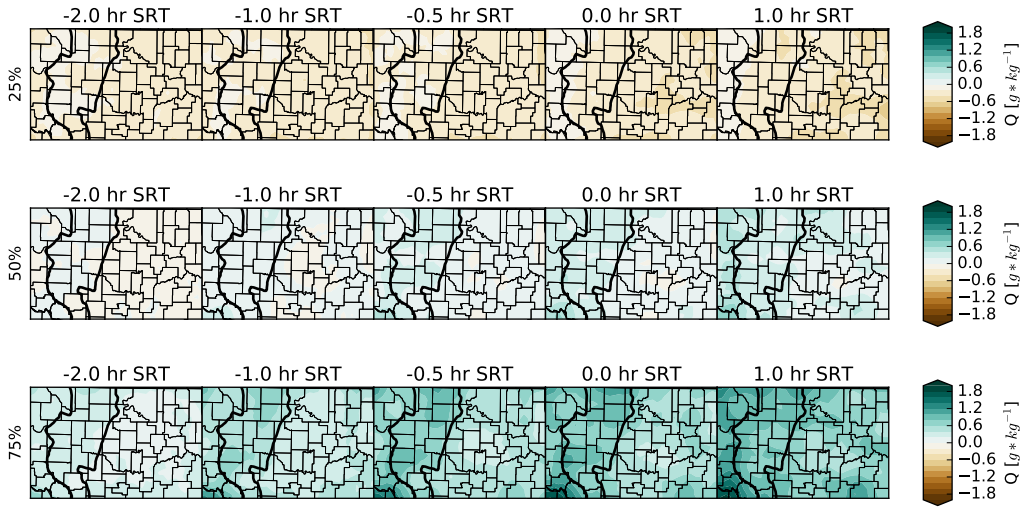

Figure 6.8: Similar to Figure 6.7, but using April analyses (n=503; 1998-2014).

These results are consistent with two past studies that used Mesonet data to understand how the WWB impacts the near-surface over the entire diurnal cycle. McPherson et al. (2004) showed how during the growing season, surface moisture increases during the daytime along the WWB. Although they used a Barnes analysis method (Koch et al. 1983) instead of 2D-VAR, their March 27, 2000 case study illustrated an instance when dewpoint increased along the WWB during the three hours prior to local sunset, similar to the trends shown in Figure 6.7. These observed McPherson et al. (2004) trends were supported in a later study by Haugland and Crawford (2005). While not a primary goal of their study, Haugland and Crawford (2005) also showed pre-sunset increases in dewpoint occur in Oklahoma Mesonet data. In their analysis of the June Mesonet data, WWB increases in dewpoint continued after sunset while stations surrounding the WWB only increased until sunset. In March, these contrasting trends were reversed; only the stations surrounding the WWB exhibited post-sunset increases in dewpoint. These changes are similar to the results in Figure

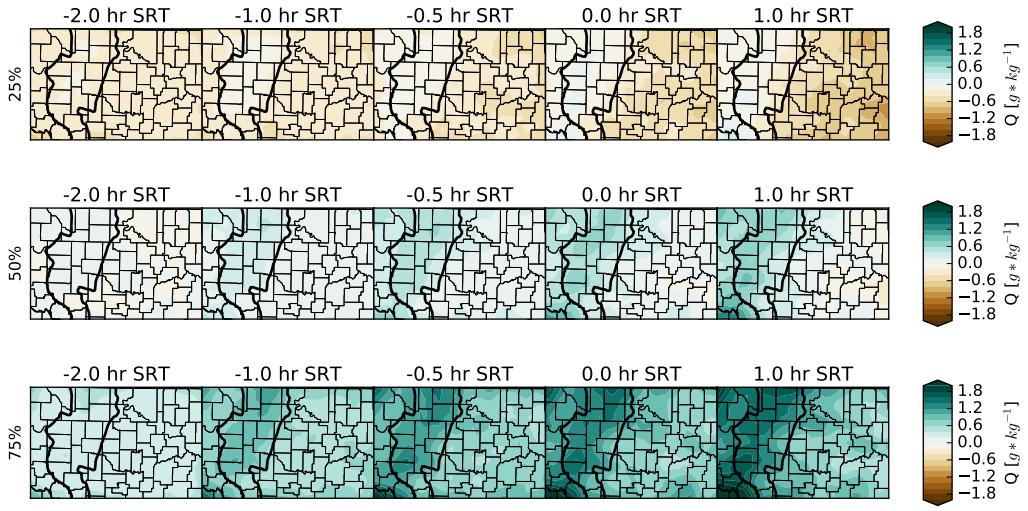

Figure 6.9: Similar to Figure 6.7, but using May analyses (n=540; 1998-2014).

6.5 and Figures 6.10 - 6.12. This new analysis, focused on the sunset time period, lends support to the results of these past two studies.

The trends shown in Figures 6.7 - 6.12 also tangentially lend some support to discussion in Acevedo and Fitzjarrald (2001). The authors of this paper illustrated how topographical and sheltering could impact the timing and magnitude of processes in the AET. While the dependency of the AET on sheltering due to wind fetch is not analyzed in this dissertation, Figures 6.7 - 6.12 also suggest the magnitude of AET moisture changes has a dependency on topography. This is most apparent in the summer months, where an evening maxima in water vapor develops parallel to I-40 in the valley between the Ozark and Ouachita Mountains in Eastern OK (Figure 6.10 - 6.12). While Acevedo and Fitzjarrald (2001) did not look at the dependency of land use on the evening transition, these results lend support to their larger hypothesis that in topography, sheltering, and land use all play a role in controlling the timing of the AET.

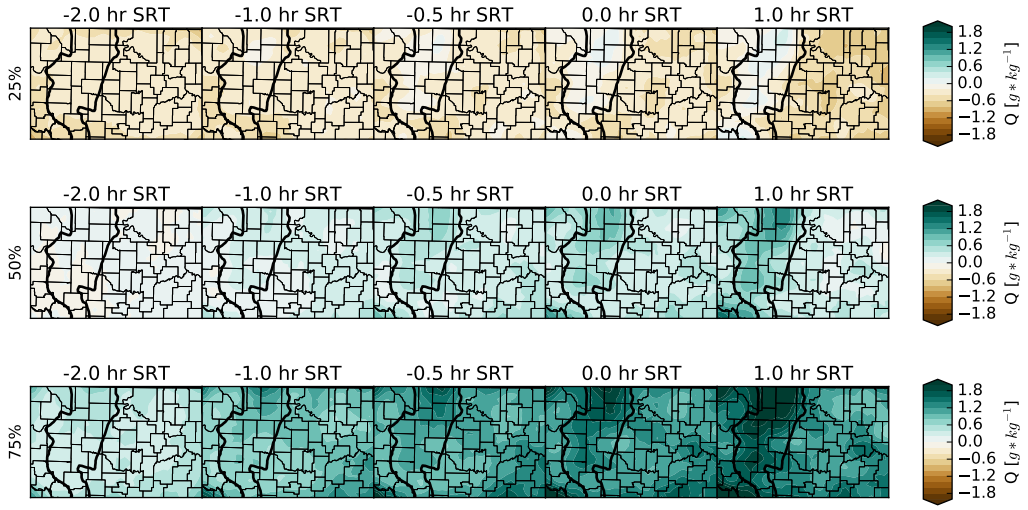

Figure 6.10: Similar to Figure 6.7, but using June analyses (n=522; 1998-2014).

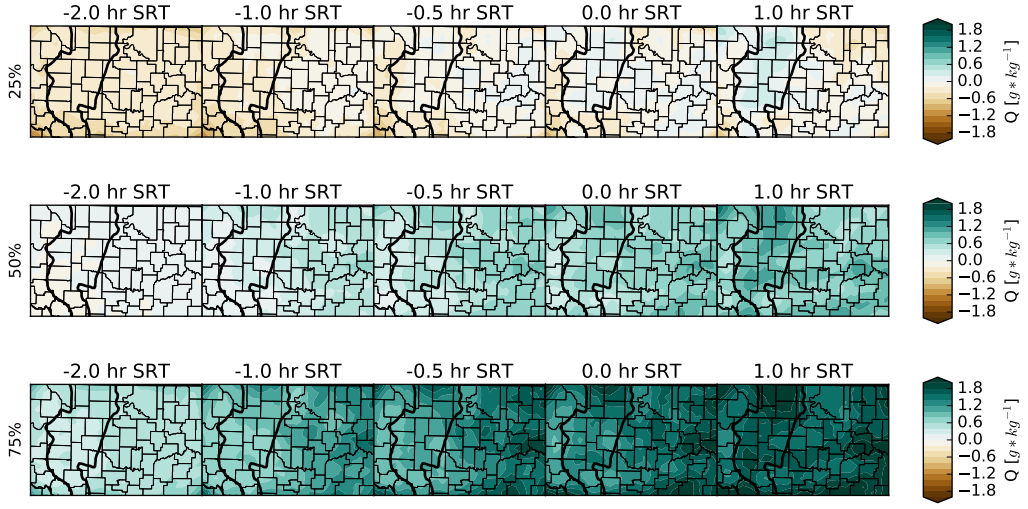

Figure 6.11: Similar to Figure 6.7, but using July analyses (n=510; 1998-2014).

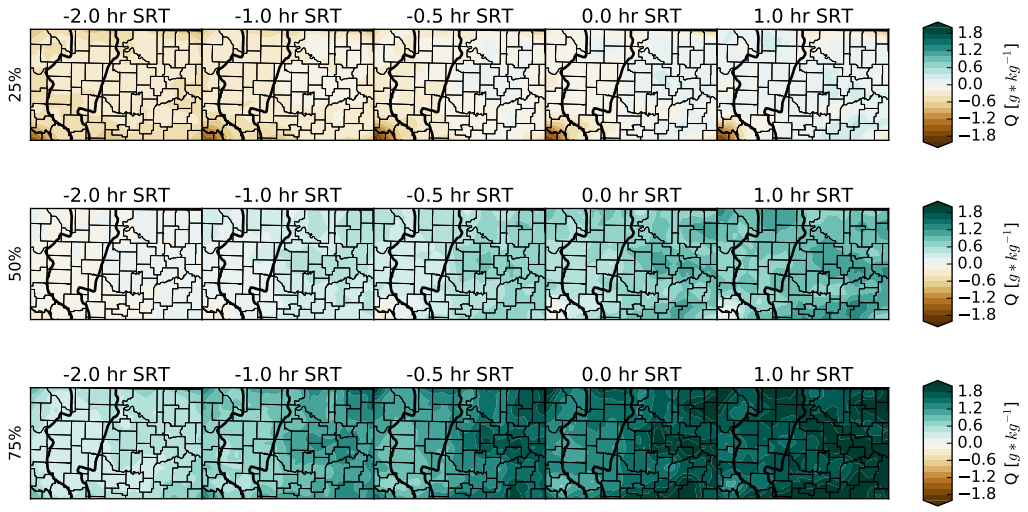

Figure 6.12: Similar to Figure 6.7, but using August analyses (n=510; 1998-2014).

6.5 Analysis of AET q_v Maxima

Further analysis showing the dependency of the AET q_v jump on land surface conditions was accomplished by analyzing data collected during the AET to identify the time period where q_v typically reaches its maximum value. The use of a maximum in water vapor to identify this phenomenon was first suggested in Fitzjarrald and Lala (1989); Acevedo and Fitzjarrald (2001) and is extended in this study to include time series of virtual temperature T_v and surface-based 500-mb lifted index LI_5. Doing so enables this dataset to also be used to test the impact of the q_v jumps on parcel instability (**H2**).

The availability of two decades of Mesonet data enabled the construction of a stronger set of tests for **H1** and **H2**. First, because of the results described in the previous section (Section 6.4), Mesonet sites are grouped into categories by their location relative to the WWB, similar to the methodology in McPherson et al. (2004) to analyze the dependency of thermodynamic properties on the land-surface. Figure 6.13 shows the three groups used: the West Winter Wheat Belt (W-WWB), East Winter Wheat Belt (E-WWB), and Winter Wheat Belt (WWB) and the Mesonet sites contained within each group. Each group contains roughly several thousand individual AET observations available for analysis (Table 6.2). For each AET time series in the categories, the time of the maximum q_v and T_v were found. To identify maxima in conditional instability, the minimum LI_5 was identified (LI_5 becomes more negative when instability increases). LI_5 was calculated using the surface properties from the Mesonet station and an estimate of the 500-mb virtual temperature from the 3-hourly North American Regional Reanalysis (NARR, Kalnay et al. 1996).

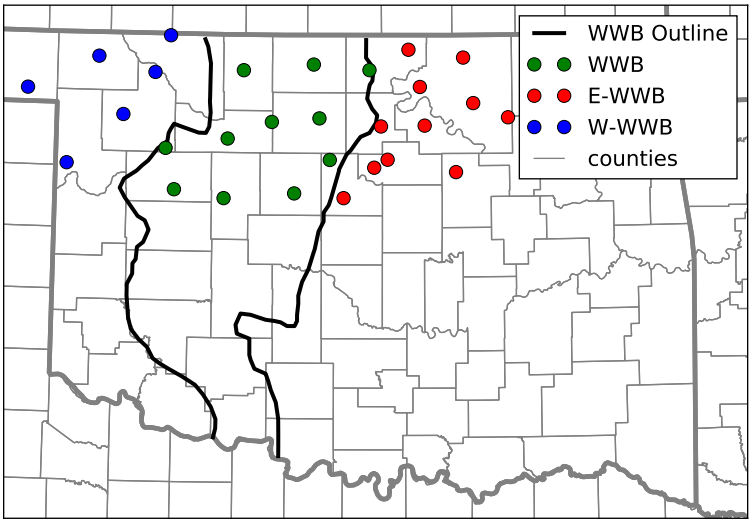

Figure 6.13: Groups of Mesonet sites relative to the winter wheat belt (WWB) used in McPherson et al. (2004). W-WWB and E-WWB refer to the sites west (blue) and east (red) of the WWB (green). The outline of the WWB from McPherson et al. (2004) is included in the map in the dark black outline.

After the identification of the time of extrema in the Mesonet time series, the data in each WWB-relative group was re-sampled in order to generate uncertainty estimates and test for statistical significance between the different groups. During the re-sampling process, 500 AET cases wer e randomly drawn 1000 times in each group (with replacement). From each 500 samples, probability distributions functions (PDFs) were estimated using a Gaussian kernel density estimator (KDE) from the SciPy stats package (Jones et al. 2001). This package uses Scott's Rule to estimate the bandwidth of the KDE (Scott 2015). Overall, this process created 1000 PDF estimates describing when extrema of T_v, q_v, and LI_5 can be found during the AET time period. In the final step, the mean and 2-sigma errors for PDFs were calculated to test for statistical significance at the 95% confidence interval. After this process was completed, tests determining the sensitivity of thermodynamic extrema to land-surface characteristics, time of year, and environmental characteristics were performed.

Figure 6.14 shows monthly bootstrapped PDFs for the q_v time series from this experiment. Peaks in the PDF represent time periods when a maxima in q_v is more likely to occur. As the wheat grows in the spring months, the probability of a maximum in q_v in the hour prior to sunset also increases (roughly from 0.0025 to 0.003). For March and April, the differences in the PDFs between the WWB and the surrounding vegetation become statistically significant at the 95% confidence interval an hour and a half prior to sunset. While a formal statistical test is not performed here, statistical significance in this research is met when the 95% confidence intervals do not overlap. Most notable in Figure 6.14, is that the surrounding areas (W-WWB and E-WWB) do not exhibit signs of a pre-sunset max in q_v. In May, the PDF for the E-WWB develops statistically significant differences from the PDF of the W-WWB. Similar to past results, the likelihood of a pre-sunset maximum in q_v increases and coincides with the growth of healthy vegetation east of the WWB in Figure 6.6. Compared to the prior months, the W-WWB PDF does not change. In summary, May tends to be the month when both the WWB and E-WWB are most likely to exhibit maxima in q_v in the 1.5 hours prior to sunset.

After the harvest of the WWB (June - August), the WWB PDFs in Figure 6.14 mirror the PDFs for the W-WWB region. In fact, their differences are not statistically significant. In these cases, a maximum in q_v tends to occur after sunset more often, suggesting that moisture tends to increase after sunset in these locations similar to the results found in Figure 6.5. Meanwhile, the PDFs describing the E-WWB indicate that in the summer months, a pre-sunset maximum in q_v is more likely than in the spring months. However in August,

there is even evidence that a post-sunset maxima in q_v may be more likely in the E-WWB than in other months.

Because a pre-sunset maxima in q_v often appears in the Mesonet time series, a pre-sunset maxima in conditional instability may also be present. Figure 6.15 shows when maxima in conditional instability (indicated by a minimum in $SBLI_5$) are most likely to occur. For all months, a maximum in conditional instability is most commonly found three to two hours prior to sunset. A maximum in instability may also be found in the post-sunset hours, however its probability is substantially less than those found in the pre-sunset hours. However, in the time period approaching sunset, when the probability of a maximum in q_v begins increasing, the PDFs in Figure 6.15 begin to flatten, and the relative probabilities coincide with those in Figure 6.14. For example, in the months prior to the winter wheat harvest, the WWB is most likely to exhibit a maximum in conditional instability compared to the surrounding regions. The only exception is in May, when both the E-WWB and WWB regions are most likely to show maxima in q_v and $SBLI_5$ prior to sunset. After the harvest, the E-WWB is more likely to have a pre-sunset maxima in conditional instability compared to the surrounding regions.

These differences in $SBLI_5$ between WWB-regions are not as distinct as those previously shown for q_v. Statistical significance at the 95% confidence interval between the WWB and E-WWB is only apparent in the March and April months. In May, statistical significant differences between the W-WWB sites and WWB occur only 40 minutes prior to sunset. After the harvest, statistically significant differences at the same confidence level do not occur between the various WWB regions. However, the presence of a maximum in

conditional instability prior to sunset that coincides with maxima in q_v lends support to **H2** that such jumps in water vapor can increase parcel buoyancy.

An alternative hypothesis can be posed suggesting that minima in $SBLI_5$ are attributable to maxima in temperature instead of q_v. Figure 6.16 shows when the maximum value of virtual temperature occurs during the AET. For all months, the maximum of T_v is often found in the first hour of the AET time period. When comparing Figures 6.15 and 6.16, the maximum in instability that occurs one hour to sunset is not likely explained by a maxima in T_v, as the probability for a maxima in T_v is nearly 0 in Figure 6.16. This conclusion is supported also by the inspection of numerous individual Mesonet AET cases. Many cases reject this hypothesis by showing jumps in instability in the hour prior to sunset despite falling temperatures and loss of insolation. The sole factor contributing to these pre-sunset jumps in instability are distinct jumps in q_v.

A natural question to regarding the pre-sunset jumps in q_v follows: What environmental factors make these jumps more likely? Past literature discussed in the background section suggests these jumps may be a combination of three factors: the strength of evapotranspiration (Wingo and Knupp 2015), the ambient wind speed (Acevedo and Fitzjarrald 2001), and the presence of cloud cover (Acevedo and Fitzjarrald 2001). To test these hypotheses, Mesonet observations between 90 minutes prior to sunset and sunset were averaged and used as independent variables to classify the environmental conditions present during each AET timeseries. For dependent variables, PDFs were integrated within the same time frame to produce probabilities of a pre-sunset maxima in

q_v during an AET. Bootstrapping of the AET cases were again used to assess statistical significance between the different environmental factors.

The averaged independent variables used were the fractional water index (FWI), 10-m wind speed, and the cloud cover classification. As the Mesonet sites used in this study did not directly measure evapotranspiration, fractional water index (FWI) is used as a proxy variable instead. FWI ranges between 0.0 (very dry) and 1.0 (very wet, soil at field capacity) and can be calculated from the Mesonet soil moisture measurements (Illston et al. 2008). To test for dependencies on FWI and surface wind speeds, datasets were split up by the median values of each independent variable. For example, AET cases were divided into two categories ($FWI > 0.85$ and $FWI < 0.85$), as the median value of FWI within this dataset was roughly 0.85. This enabled AETs to be categorized as having wet soil ($FWI > 0.85$) or dry soil ($FWI < 0.85$) or as having fast wind speeds (> 5 m/s) or slower speeds (< 5 m/s).

Figure 6.17 shows the dependency of the pre-sunset q_v maxima on soil moisture. For most months out of the year and WWB-relative regions, increased soil wetness (denoted as larger FWI) generally increases the probability of a pre-sunset q_v maxima by roughly 5-10%. For the W-WWB and WWB regions, these differences between FWI amounts are statistically significant for most months out of the year. While not exactly measuring the evapotranspiration from the surface, the increase in likelihood of a pre-sunset maxima in surface q_v in conditions where wet soil is present hints that evapotranspiration might be playing a role in increasing the surface q_v during the pre-sunset period.

Experiments showing the sensitivity of the pre-sunset q_v maxima to ambient surface wind speeds are outlined in Figure 6.18. First, the probability of pre-sunset W-WWB q_v maxima does not show any strong sensitivity to surface wind speed. However, for the WWB and E-WWB categories, AETs with slower wind speeds exhibit a higher probability of a pre-sunset q_v maxima than those with higher wind speeds (generally a 10-15% difference). These differences are statistically significant for the WWB in the spring months and in all months except for March in the E-WWB category. Finally, it is apparent that the impact of wind speed on the pre-sunset q_v maxima is strongest when vegetation is present. For example, the largest changes to the pre-sunset q_v maxima probability occur on the WWB prior to the harvest (spring months) and when vegetation found east of the WWB is growing.

In a final experiment towards understanding how environmental conditions impact the pre-sunset maxima in q_v, bootstrapped PDFs of q_v maxima were produced for AETs with clear, scattered, and overcast skies. For the WWB dataset, the PDFs for the clear and scattered skies for spring and summer months are nearly identical (Figure 6.19). The primary exception is in AET that occur in March, April, May and June, where the probability of a q_v maxima in the first hour of the AET is slightly greater when the sky has scattered clouds than when the sky is clear. Regardless, the signal for the pre-sunset q_v maxima is apparent in the spring months for both clear and scattered skies, similar to the patterns illustrated by Figure 6.14.

Figure 6.19 also shows that for AETs with overcast skies, the PDF for the q_v maxima generally becomes uniform. This shift from a highly structured PDF to a uniform PDF is most apparent the months of May to August. In March and

April, the maximum likelihood of a q_v maxima is easily found in the first hour of the AET. Overall, these results corroborate previous studies (e.g., Acevedo and Fitzjarrald 2001) that overcast clouds diminish many of the signals indicative of the AET.

The results discussed within this chapter provide insight into the evolution of moisture during the SGP AET. First, increases in water vapor similar to those found in past studies occur during the SGP AET. These increases ranged between 1-3 g/kg and tend to begin in the hours preceding sunset. Second, horizontal analyses created by the 2D-VAR program demonstrated that the location of these moisture increases is dependent upon the placement and health of vegetation. Further analysis in Section 6.5 reinforced this dependency and generally confirms **H1**. This section showed that the probability of a pre-sunset maximum in q_v is largest along the WWB in the springtime and east of the WWB in the summertime. Subsequent tests illustrated that this probability also increases when surface wind speeds are small, the skies are not overcast, and when the soil moisture is high. Finally, the Mesonet data analyzed shows that **H2** may also be accepted, as the pre-sunset maximum in moisture also may generate a maximum in conditional instability. With the lateral evolution of moisture in the SGP AET now better characterized, the following chapter begins to incorporate the vertical dimension.

Table 6.2: Total number of AET cases available for analysis in each WWB-relative category.

Month	W-WWB	WWB	E-WWB
March	3888	6607	7128
April	3768	6400	6908
May	3900	6623	7150
June	3780	6420	6930
July	3906	6634	7161
August	3780	6420	6930

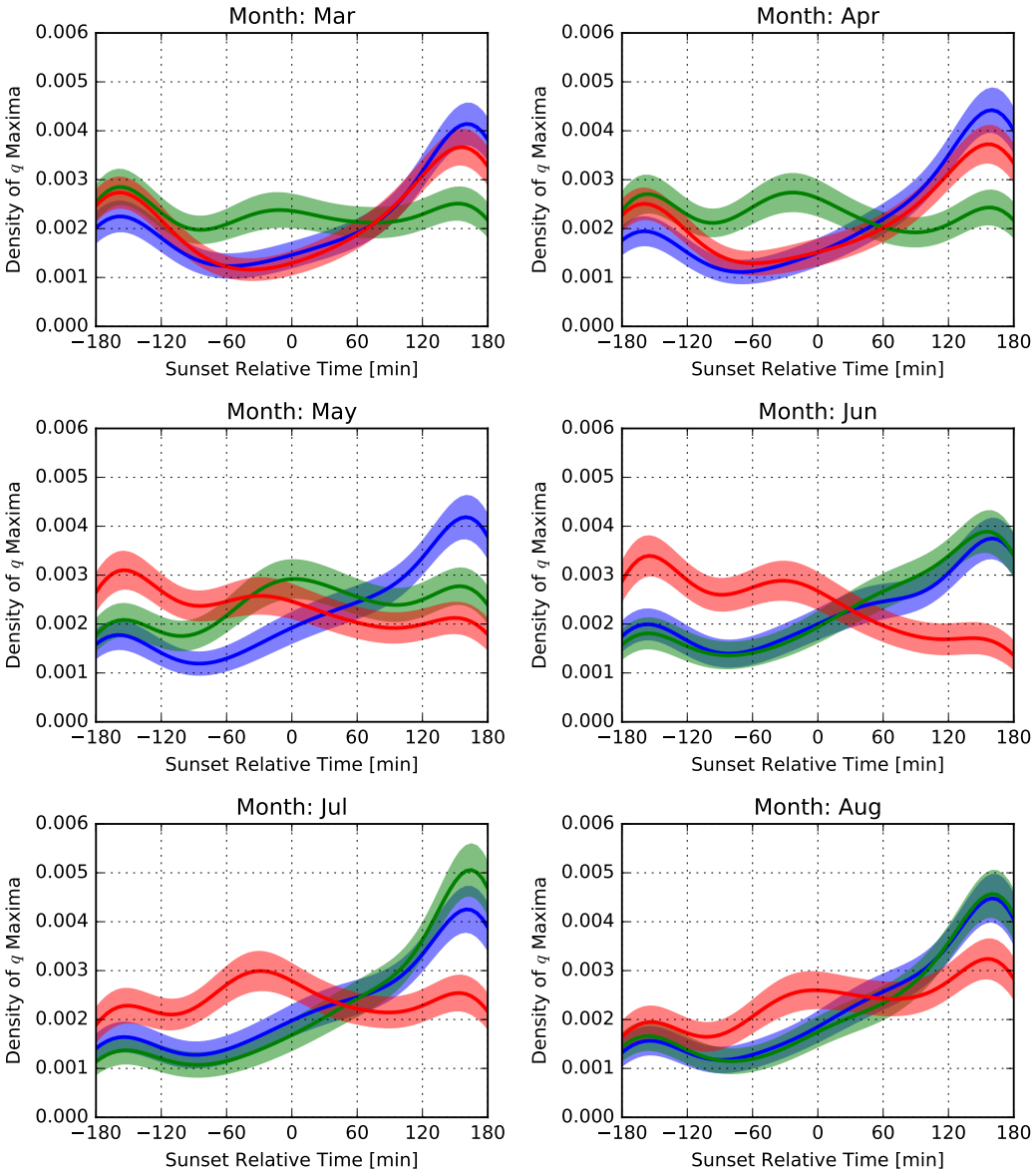

Figure 6.14: Bootstrapped probability density functions describing when q_v typically reaches a maxima in the AET time period. Individual panels show the PDFs of WWB-relative group for the months of March through August. The three thick lines indicate the mean PDFs for each group and follow the coloring scheme outlined in Figure 6.13 where blue is W-WWB sites, red is E-WWB sites, and green is WWB sites. Shading represents the 95% confidence intervals calculated via bootstrapping.

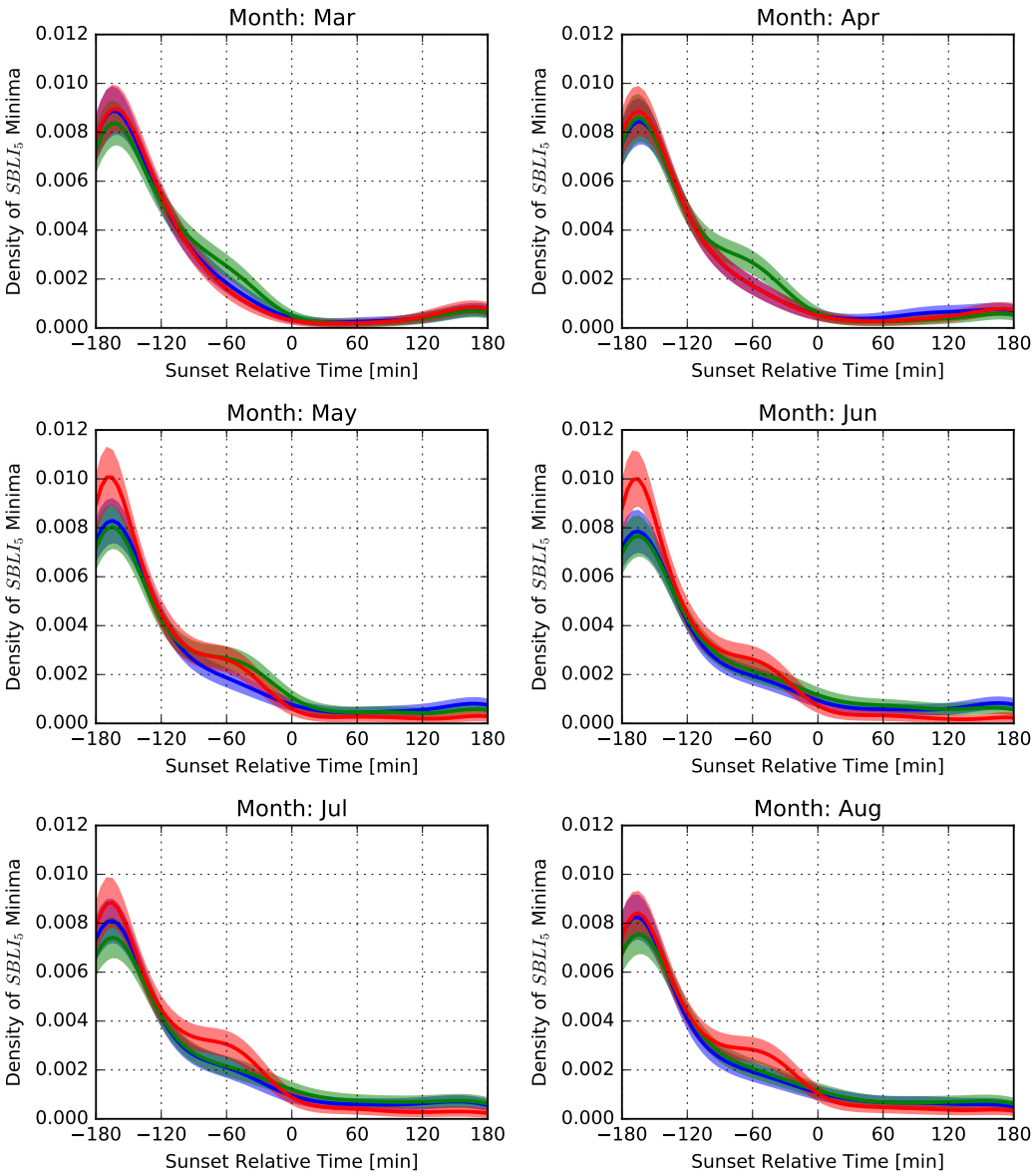

Figure 6.15: Similar to Figure 6.14, but for the 500-mb lifted index LI_5.

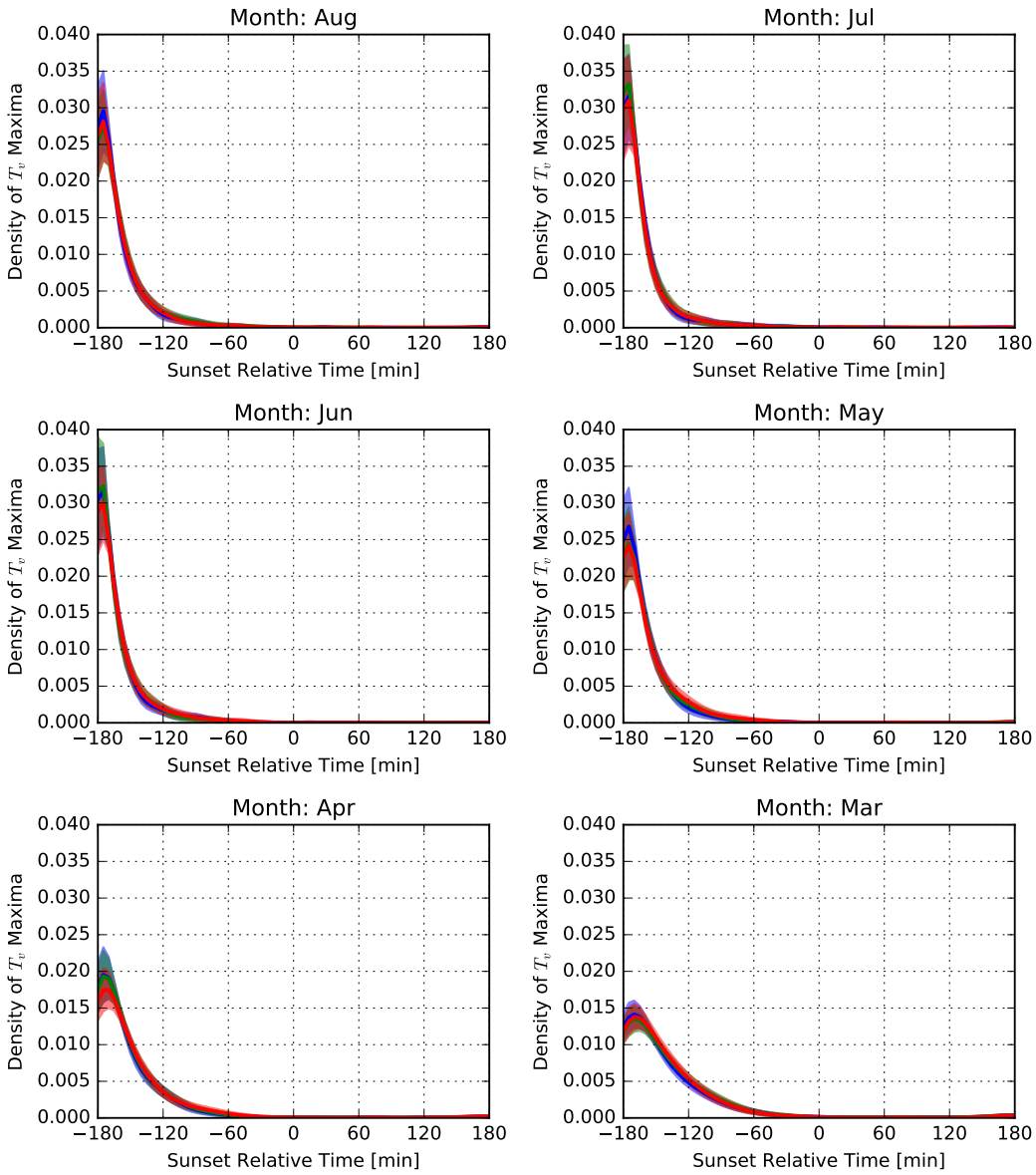

Figure 6.16: Similar to Figure 6.14, but for the surface virtual temperature T_v.

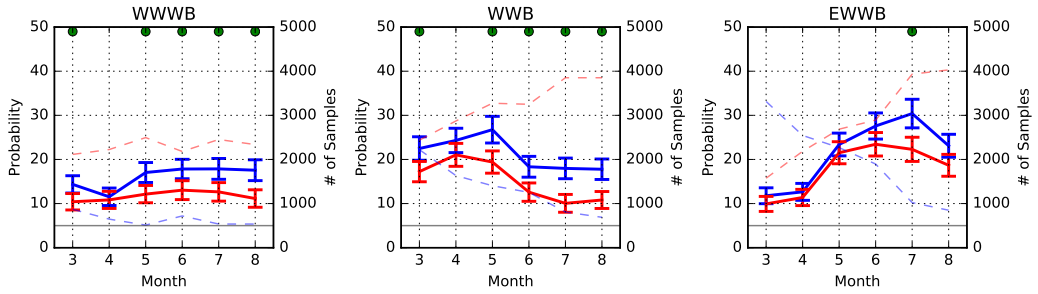

Figure 6.17: Plots illustrating how the probability of a q_v maxima prior to sunset is dependent upon fractional water index (FWI), time of year, and WWB-region. Solid lines depict the probability of the q_v maximum occurring within an hour and a half prior to sunset. Each panel indicates a WWB-region and the x-axis indicates each month. Blue indicates the category where the $FWI > 0.85$ while red indicates the category when $FWI < 0.85$. Error bars indicate the 95% confidence interval (CI) of those probabilities, computed by bootstrapping. Green dots indicate months where differences between the two distributions are statistically significant at the 95% CI. The dashed lines indicates the number of samples available for bootstrapping, while the horizontal solid gray line indicates the minimum number of samples for bootstrapping (500).

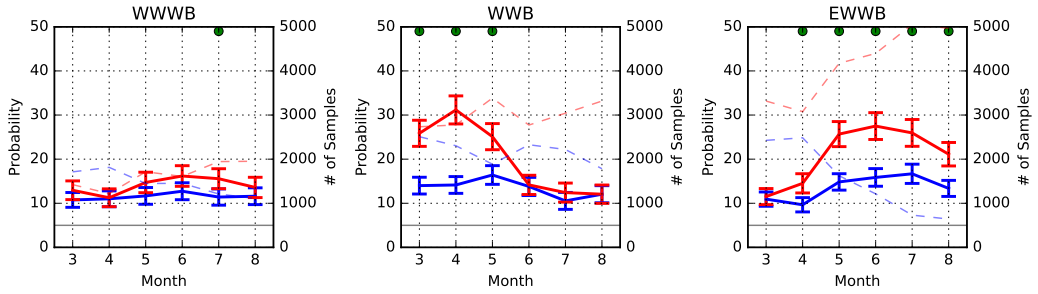

Figure 6.18: Similar to Figure 6.17, but for the dependency on surface wind instead of FWI. Red indicates cases where the average surface wind was less than 5 m/s, while blue were cases when the average surface wind was greater than 5 m/s.

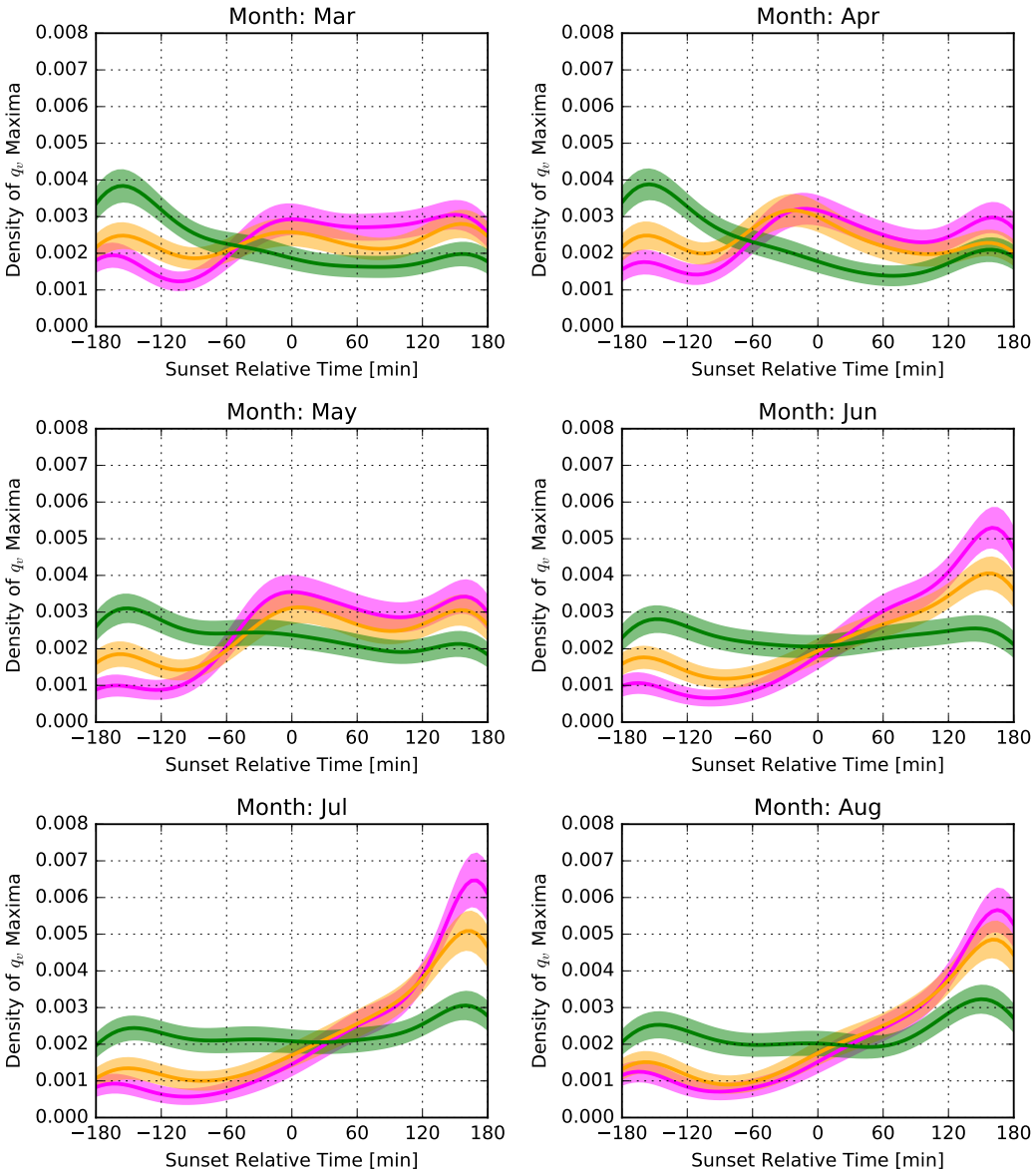

Figure 6.19: Similar to Figure 6.14, but with two exceptions. First, the PDFs shown are only using AET cases from the WWB category. Second, instead of WWB categories, the colors correspond to different cloud cover categories from the cloud detection algorithm described in Section 6.1. For the different PDFs, magenta indicates clear skies, orange indicates scattered skies, and green indicates cloudy skies.

Chapter 7

Vertical Evolution of Moisture

In the previous section, only surface observations were used to analyze the characteristics of AET q_v jumps across horizontal space. Now, the analysis turns to the vertical dimension. To do this, observations of AETs collected at the ARM SGP site are used. These observations are limited to only the summer months to investigate the environmental characteristics of the stronger q_v increases found in Chapter 6. Particularly, this chapter seeks to characterize q_v jumps in the vertical dimension. By expanding the analysis into the vertical, the vertical extent of these increases in moisture are determined (Question 1, Chapter 3). In addition, questions regarding the environmental characteristics present during these jumps and the impact of these jumps on conditional instability (Question 2, Chapter 3) will be assessed using the wide variety of instruments available at the ARM site.

This chapter consists of four sections. In the first section, the methodology to select 31 cases from data collected at the ARM SGP site between 2016 and 2017 is discussed. In the following three sections, three different approaches are taken to summarize the SGP AET data. First, the time denoting the start of the evening transition (t_{ET}) between the ECOR and EBBR instruments is compared. Next, the six of the selected cases are shown in detail to illustrate the range of variability in the evolution of the PBL during the AET. Finally,

composite plots of these cases are analyzed to summarize the common features appearing in observations taken at the ARM SGP site during the AET.

7.1 AET Cases from ARM Site

Up to this point, much of the data has been analyzed in a statistical framework to generalize the various trends of water vapor and instability during the AET. Due to the increase in variable types and independent variables (time and height) available to analyze the AET at the ARM site, the analysis strategy in this section was shifted towards analyzing individual AET cases with rises in q_v. To do this, an approach similar to Busse and Knupp (2012) was used to analyze a subset (31 cases) of the AET cases from the ARM site. Attention was paid to understanding common and atypical changes in moisture, wind speed and direction, vertical velocity variance, and conditional instability during the AET.

The 31 cases selected used criteria to account for synoptic influences and cloud cover present at the ARM site. First, only cases with scattered clouds or clear skies with increases in q_v before and after sunset were chosen. This criteria was chosen as Chapter 6 showed that increases in water vapor tended to occur in the pre-sunset hours most often in cloud-free or scattered skies. Second, priority was given to cases with conditional instability (parcels with CAPE greater than 0 J/kg) diagnosed from the AERIoe profiles. Doing so allowed a visual assessment of the changes in conditional instability. Finally, only cases showing consistent southerly winds throughout the AET were included to control for synoptic scale boundaries (e.g., cold fronts). During case selection, it was found that the cases that met these constraints of conditional instability, water

Table 7.1: The 31 individual cases analyzed from data collected at the SGP ARM site. Δq_v is the size of the jump over time in g/kg and was estimated from the surface-met time series. The depth Δz of the q_v jump is listed in km and was estimated from the AERIoe retrievals. The start time of the jump (t_{start}), the end time (t_{end}) and the ET time (t_{ET}) are listed in hours relative to local sunset. The last column represents the tendency in water vapor using Δq_v and $\Delta t = t_{end} - t_{start}$. The final rows represents the average (μ) and 1-σ standard deviation of the data in the columns.

Case	Date	t_{ET}	Δq_v	t_{start}	t_{end}	Δz	$\Delta q_z/\Delta t$
1	08-18-2016	-0.5	2.0	-0.9	-0.5	1.0	4.0
2	07-20-2016	-0.9	1.8	-1.8	-1.3	1.5	3.6
3	06-22-2017	-1.2	4.0	-3.5	0.0	1.0	2.0
4	06-16-2016	-1.8	5.0	-1.9	0.2	2.0	2.4
5	07-18-2017	-2.1	2.0	-0.8	0.5	1.0	1.5
6	07-20-2017	-1.1	2.0	-1.0	1.0	0.75	2.0
7	06-25-2016	-1.4	1.5	-3.5	3.0	1.2	0.2
8	06-28-2017	-1.1	2.0	-3.5	1.0	1.0	1.0
9	07-18-2017	-2.1	4.0	-3.0	1.0	1.0	1.0
10	07-19-2016	-1	4.0	-3.0	3.0	1.0	0.6
11	07-22-2016	-1.4	3.0	-1.0	3.0	0.25	0.8
12	07-31-2016	-2.4	4.0	-3.0	0.5	1.0	1.1
13	07-11-2017	-3	4.0	-1.0	2.0	1.0	1.3
14	07-12-2017	-2.2	2.5	-1.5	1.0	0.75	1.0
15	07-17-2017	-2.1	3.0	-3.0	1.0	1.0	0.8
16	08-03-2016	-2.2	2.5	-3.8	0.0	1.0	0.7
17	08-17-2016	-1.3	1.5	-1.8	0.5	1.0	0.7
18	08-04-2017	-0.7	1.7	-1.0	0.5	0.25	1.1
19	07-24-2016	-1.4	3.7	-3.5	3.0	0.75	0.5
20	06-20-2016	-1.6	2.0	-2.3	1.0	0.5	0.6
21	06-17-2016	-1.7	2.0	-2.5	0.5	1.5	0.7
22	06-15-2016	-1.6	4.2	-2.7	1.0	1.0	1.1
23	07-19-2016	-1	2.0	-3.0	2.0	0.75	0.4
24	07-19-2017	-1	4.0	-0.9	1.5	0.75	1.6
25	07-06-2017	-2.6	4.0	-1.5	0.0	0.5	2.7
26	08-01-2016	-2.5	3.0	-1.8	0.0	0.75	1.7
27	06-21-2016	-1.6	4.0	-1.0	3.0	0.5	1.0
28	07-23-2016	-1.2	3.5	-2.5	1.4	0.75	0.9
29	07-21-2016	-1.3	2.0	-1.5	1.0	1.0	0.8
30	07-04-2016	-2	3.5	-1.7	1.0	0.75	1.3
31	06-19-2016	-1.6	2.0	-1.0	0.0	0.75	2.0
μ:	–	-1.6	2.9	-2.1	1.0	0.9	1.3
$1-\sigma$:	–	0.6	1.0	1.0	1.1	0.3	0.9

vapor increases, mostly clear skies, and southerly winds are most often found in the summertime months. This is not surprising, as Chapter 6 indicated that northern Oklahoma experiences some of the largest increases in q_v during the AET after the harvest of the WWB. The filtering described in this section also help investigate the large q_v jumps and environmental characteristics that occur near the eastern edge of the WWB even though the wheat has been harvested (**H1**). This is also useful as two of the cases appearing in this dataset were also simulated by the LASSO project (Chapter 8). Although there were cases that had increases in q_v, but were outside this set criteria (e.g., northerly winds prior to the harvest), they are not considered at this time.

Table 7.1 lists these cases and the various characteristics of their evolution in q_v. To understand the evolution of turbulence relative to the surface-fluxes, the time of the ET (t_{ET}) from the ECOR was recorded. This variable was calculated via linear interpolation as the temporal resolution of the data is every 30-minutes. For each case, the beginning and ending times (t_{start}, t_{end}) of the q_v jump and magnitude of the q_v jump (Δq_v) was estimated by analyzing the RLID, AERIoe retrievals, and MET data. The depth of these jumps were also estimated by visual inspection of the AERIoe retrievals for each case and were found to occur over a 1 km depth on average. From these 31 cases, the average magnitude of these jumps in water vapor are on the order of $2.9 \pm 1\, g/kg$. The average rate at which q_v increases (1 g/kg/hr) in this data is similar to the rate of jumps found in past literature (e.g., Acevedo and Fitzjarrald 2001).

7.2 Identifying the Evening Transition

As the analysis of these cases uses the time of the evening transition as a benchmark of the AET, the heat flux data from the EBBR and ECOR data streams were compared. In this comparison, estimates of the time of the evening transition (t_{ET}) were derived from each dataset by using linear interpolation of the sensible heat flux time series. This comparison is illustrated in Figure 7.1. Quickly evident in this figure is the clustering of points around an hour and half prior to sunset, which is around the time in which q_v begins to increase per Chapter 6. Although both the ECOR and EBBR instruments typically agree on the general timeframe of the ET, the ECOR tends to place the ET earlier in the evening than the EBBR (10 minutes on average).

These differences between the ECOR and EBBR may be due to several different reasons. First, both the ECOR and the EBBR instruments are sampling different fields. While the ECOR primarily views contributions to the flux by the field south of the ARM site used to grow winter wheat, the EBBR sees contributions from grassland and pasture (Bagley et al. 2017). As many of the ETs with a southerly wind component also had an easterly component, it is possible that in these cases both the ECOR and EBBR were observing similar fetches and effectively identifying the same ET times. Another reason may be due to the differences in observing methods; the EBBR method enforces closure of the energy budget, while the ECOR does not. Despite these slight differences, only the ECOR is used in this chapter to determine the t_{ET} as Figure 7.1 suggests that t_{ET} is mostly insensitive to surface energy balance observing methods (e.g., ECOR vs EBBR).

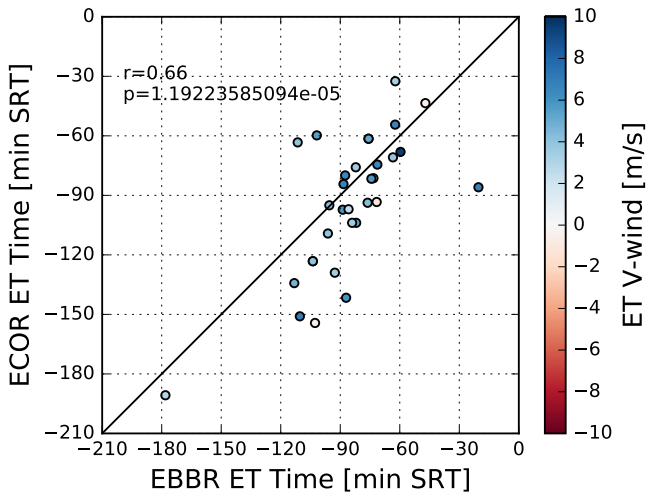

Figure 7.1: A comparison of the times of the evening transition (ET) relative to sunset observed by the ECOR and EBBR instruments for the 31 cases described in Table 7.1. Individual points are colored by the value of the meridional wind measured by the ECOR at the time of the ECOR's ET.

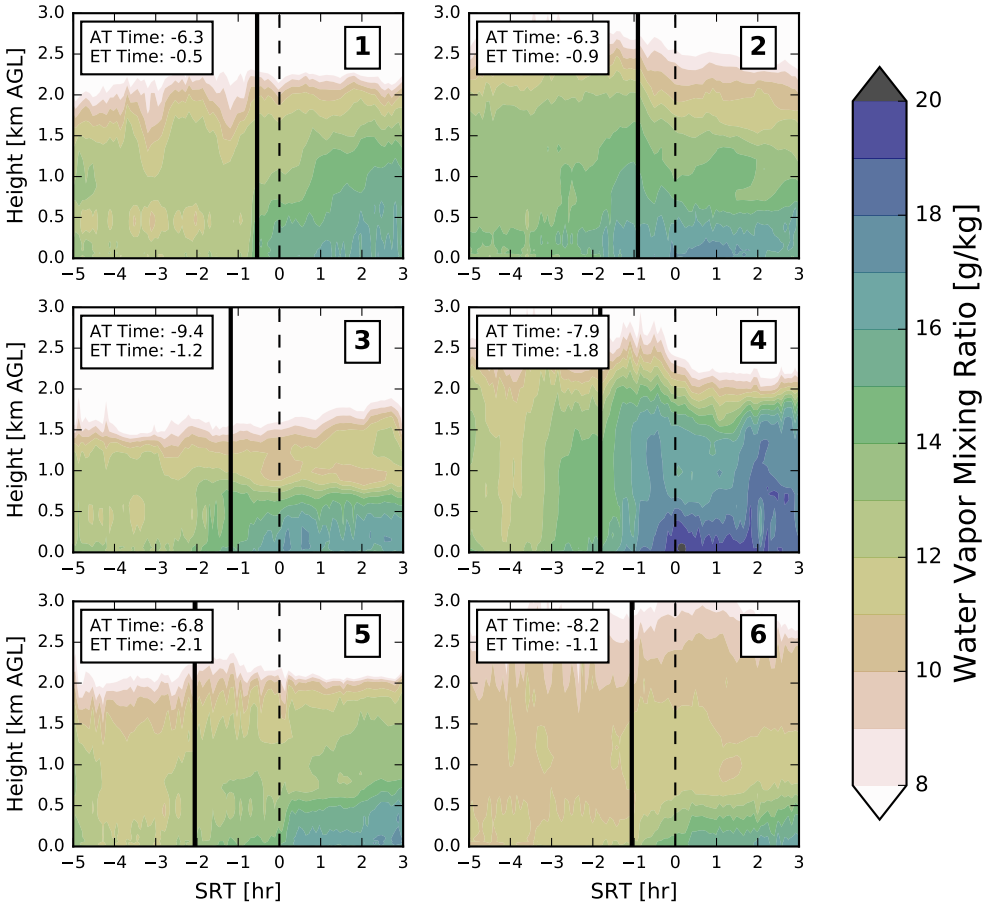

Figure 7.2: Time by height cross sections showing the evolution of water vapor mixing ratio from the AERIoe retrievals of the first six cases in Table 7.1. The vertical solid and dashed lines indicate the time of the ET and sunset, respectively. The y-axis is height above ground level and the x-axis is in sunset relative time, with 0 being the local sunset time (SRT). In the top left of each plot indicates the time of the afternoon transition (AT) and the evening transition (ET) in hours SRT.

7.3 AET Example Cases

Figure 7.2 illustrates the evolution of the vertical profile of q_v for the first six AET cases in Table 7.1. In all cases, the boundary layer prior to the start of the AET can be described as well-mixed, given the homogeneous profile of q_v. In Figure 7.2, the convective boundary layer (CBL) top is characterized by a strong vertical gradient, where q_v decreases approximately 3 g/kg over a 500-m layer. In Case 3 (Figure 7.2), this places the CBL top at approximately 1.4 km AGL 3-5 hours prior to sunset. For many of these cases (Cases 2 to 5), the increase in q_v within the decaying CBL begins at the beginning of the AET (starting 3 hours prior to sunset). The timing of these increases oppose the conceptual model put forth by Fitzjarrald and Lala (1989) and Acevedo and Fitzjarrald (2001), that suggests these increases in moisture begin after the sign of the sensible heat flux has reversed. In these shown cases, only Cases 1 and 6 display increases in q_v that begin at the evening transition. The behavior of q_v near the surface in these summertime cases is generally similar to the evolution discussed in Chapter 6.

The cases in Figure 7.2 also display variability in the number of increases in water vapor, the depth of the increases, and the rate of the increases. For Cases 1, 3, and 6, the water vapor tends to increase at a constant rate prior to sunset only once. However, Cases 4 and 5 tend to show instances in which rapid increases in q_v occur more than once. The magnitude of these increases are similar to the near-surface evolution in Figure 6.5 during the pre-sunset hours in the summer months. This is most apparent in Case 4, in which a 1.5 km deep increase of 3 g/kg occurs starting approximately 4 hours prior to sunset, and a subsequent increase of another 3 g/kg begins an hour and a half prior

to sunset. For Cases 1, 2, 3, and 4, the increases in moisture prior to sunset tend to occur over a layer 1 km in depth (see Table 7.1). Cases 4 and 6 show increases over depths larger and smaller than 1 km (approximately 2 km and 0.5 km, respectively). Finally, some of the largest differences in the rate of the q_v increase can be seen in Cases 1 and 5. In Case 5, the increase in moisture starting just before the evening transition increases at a rate of approximately 2 g/kg in 3 hours. However, Case 1 is more extreme. The increase in water vapor starting just prior to the evening transition occurs at a rate of 3 g/kg in 1 hour. These six cases show q_v increases at the SGP site may occur at different speeds, depths, and number of times that they occur.

As these cases occur in a mostly cloud-free sky with a slowly decreasing sensible heat flux, they have a somewhat general decay in turbulence within the CBL. Figure 7.3 depicts the evolution of vertical velocity variance ($\overline{w'^2}$) for the six cases analyzed. Prior to the AET, the DLID displays large $\overline{w'^2}$ throughout the CBL. In Case 4, $\overline{w'^2}$ of more than 1 m^2/s^2 extends from the surface to just above 2 km AGL, where the vertical gradient in q_v reaches a maximum (-5 to -4 hr SRT). For Cases 1,2,4,5, and 6, $\overline{w'^2}$ in the top half of the boundary layer undergoes a somewhat sharp reduction 1-2 hours prior to the evening transition. In Case 4, this occurs just shy of two hours prior to sunset. This decay in turbulence is similar to the downward trend observed using a radar wind profiler (RWP) in Wingo and Knupp (2015). Their analysis only began 3 hours prior to sunset and was limited to the lowest 200 m AGL, which makes a comparison between the cases here and their results complicated. However, this type of evolution of the turbulence is somewhat seen in RWP observations of AETs in northern Alabama (Busse and Knupp 2012). This rapid decay of

$\overline{w'^2}$ in cases 2-5 may depict the development of the pre-residual layer defined in Nilsson et al. (2016b) and Darbieu et al. (2015). Case 5 best shows this feature an hour and a half prior to the start of the evening transition. At that time, a 1 km layer of reduced turbulence develops downward below the CBL top. In some cases, the pre-residual layer appears distinct in the observations within the lower half of the CBL until the evening transition begins and $\overline{w'^2}$ becomes small everywhere within the former CBL.

Figure 7.3 also suggests that at least at the SGP site, there appears to be a time delay between the sharp reduction in turbulence and subsequent moisture increases. For Cases 4, 5, and 6, the difference between the time of $\overline{w'^2}$ reduction and the deep increase in moisture is approximately 1-2 hours. For Case 3, the $\overline{w'^2}$ reduction occurs about 2.45 hours prior to sunset while the increase in moisture over a depth of 750 meters occurs approximately 1.5 hours prior to sunset. This time delay occurred in Case 4 as well, however only with the second rapid increase in moisture starting about 1.5 hours prior to sunset. It should be noted that this assessment is based upon common visual features within these individual cases and can provide only a rough estimate of the time passed between the quick changes in $\overline{w'^2}$ and any increases in q_v. Thus, development of alternative methods to quantify this time delay are needed to better understand its variability.

However, the evolution of the low-level wind profile appears to have more common changes across the 6 cases. Figure 7.4 describes the evolution of the meridional component of the wind for these six cases. Southerly winds dominate the CBL for the entire time period analyzed, and throughout the entire period the v-wind tends to increase ($\partial v/\partial t > 0$). The increases in southerly

wind speed in the lowest 1 km of the atmosphere are most apparent after the evening transition occurs (Cases 1, 3, 4, 5 and 6). These accelerations in the low-level winds have been extensively documented at the ARM site (e.g., Stensrud1996) and are likely attributable to the Holton (1967) and Blackadar (1957) mechanisms creating nocturnal low-level wind maximums (Shapiro et al. 2016). In Case 5, however, the acceleration of the low-level winds does not occur immediately after the ET begins. Rather, the increase in low-level wind is more apparent after sunset. For all six cases considered here, southerly winds persist throughout the entire transitional period, as is expected from the case selection criteria.

The evolution of the zonal wind component, however, exhibits substantially more directional variation (Figure 7.5). For all six cases, the zonal wind component in the lowest 1 km exhibits either a reversal of the sign of the u-wind or an acceleration of the u-wind component towards the west. The timing of these changes in wind varies between the six cases. In Cases 1 and 3, the sign of the u-wind reverses prior to the evening transition and prior to the increases in q_v. For Case 1, this occurs about -2 hr SRT; for Case 3 this occurs approximately -3 hr SRT. In Case 4, an acceleration towards the west also occurs within the same time frame. Interestingly, these cases feature an acceleration of the wind to the west also occurring after the water vapor increases. This acceleration is most apparent in Cases 1, 2, 5, and 6. For example, the u-wind in the lowest 1 km of Case 1 increases to -5 m/s between -50 mins SRT to 60 minutes SRT. From Figure 7.5, it appears that backing of the low-level winds at the ARM SGP site may coincide with low-level increases in q_v during the AET.

With respect to the impacts of the increase in q_v on conditional instability, in each case, the places undergoing moistening also exhibit an increase in CAPE

with time (Figure 7.6). These increases generally occur on the order of 1000 J/kg with the more dramatic changes occurring in Case 5 with an increase of 2000 J/kg over 1.5 hours. Case 4 has the most intense changes in CAPE; parcels just above the surface nearly double to 5000 J/kg during the AET. These increases in instability occur despite reducing insolation as sunset approaches. However, the impacts of surface cooling and the development of the nocturnal inversion do impact the CAPE, albeit in a very shallow near-surface layer after sunset. This is best seen in the reduction of CAPE near the surface after sunset in Cases 2, 3, and 5. Despite this, these increases in moisture during the AET correlate strongly with increases in CAPE. This correlation strongly supports **H2**.

An additional test was performed using the AERIoe retrievals to infer causality by quantifying the impact of the moisture increases on CAPE. In this test, another set of calculations of CAPE were made using SHARPpy. This time, the q_v profile measured prior to the AET was assumed not to change with time. Figure 7.7 shows the difference in CAPE from this comparison. For these cases, the changes in moisture contributes 1000-3000 J/kg to the overall CAPE change. These tests suggest that these moisture increases do increase the conditional instability (**H2**). Without the shown increases in q_v cases, CAPE decreases everywhere throughout the AET (not shown). Generally, the increases in moisture that are far removed from the surface tend to retain their impact on CAPE longer, as they are not impacted by the near-surface cooling occurring during the AET.

A final test relevant to the impact of moisture on conditional instability was performed to understand the relationship between CIN and q_v changes at the

ARM site. Figure 7.8 shows that the q_v increases help improve the probability that parcels may become positively buoyant should lift be present. For all cases, the corresponding increases in moisture coincide with increases in CIN. This is easily apparent in Case 5, as the two increases in q_v (-3.5 hr SRT and -2 SRT) that increase the CAPE also reduce the CIN of parcels above 1 km AGL to nearly 0 J/kg. For Cases 1, 2, 4, and 6, these elevated increases in moisture remove all negative buoyancy inhibiting the parcel. Similar to the CAPE, these impacts of moisture are constrained to an elevated layer after sunset, due to the radiative cooling near the surface reducing the parcel equivalent potential temperature.

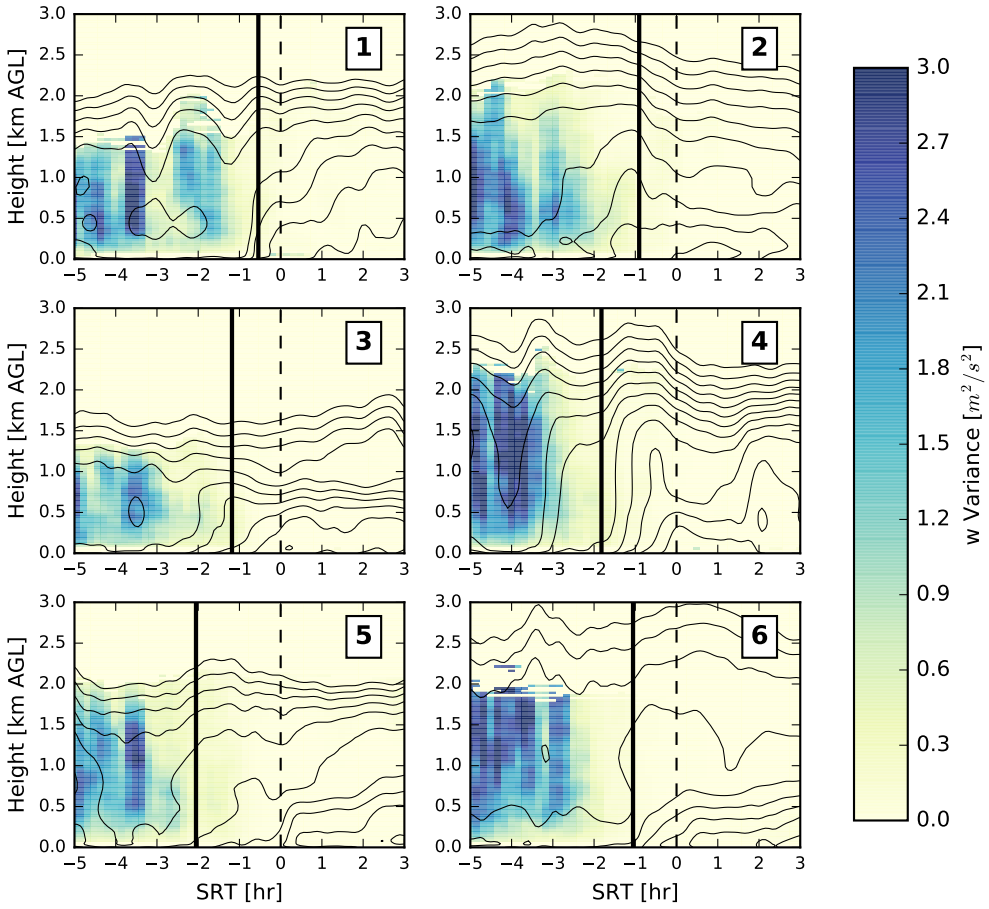

Figure 7.3: As in Figure 7.2, but for vertical velocity variance ($\overline{w'^2}$) from the DLID. The black contours indicate lines of constant mixing ratio (every 1 g/kg) from AERIoe smoothed by a 2D Gaussian smoother ($\sigma = 1.5$) to illustrate the moisture evolution relative to the turbulence decay. The topmost contour in each plot indicates the 8 g/kg line. $\overline{w'^2}$ is only shown if the signal to noise ratio is above 1 $m^2\,s^{-2}$

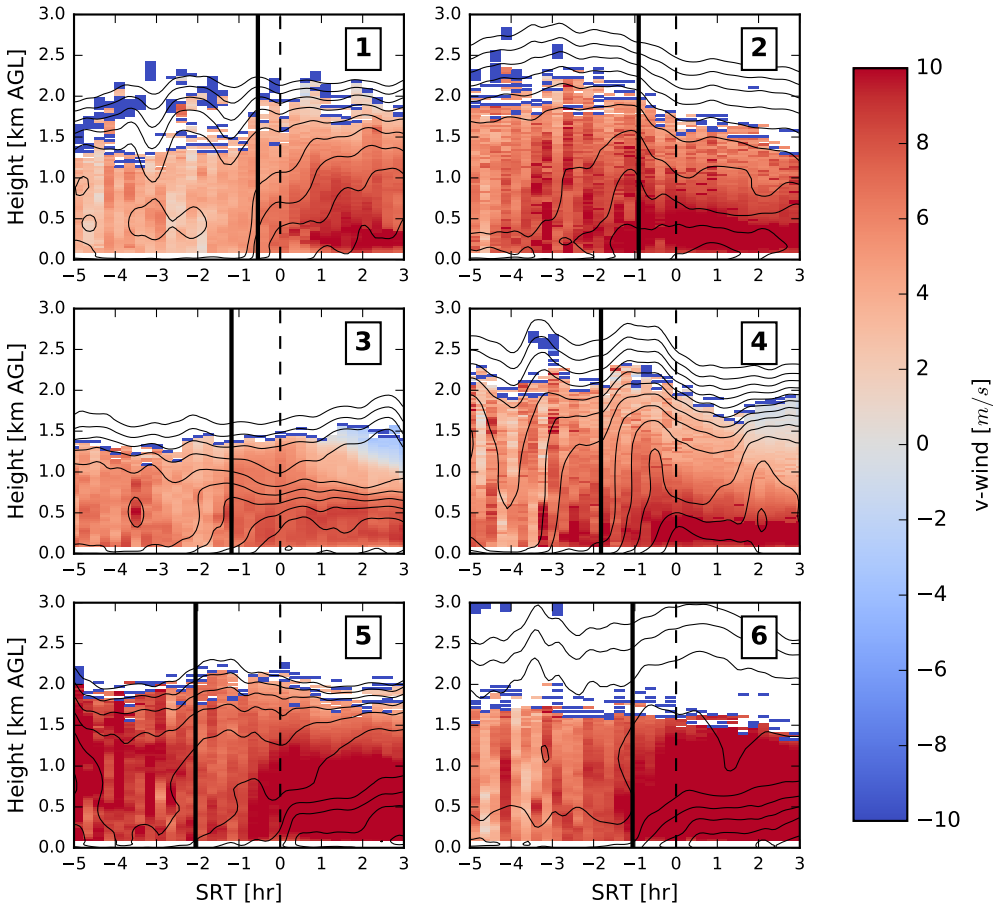

Figure 7.4: As in Figure 7.3, but for the meridional wind obtained from the DLID.

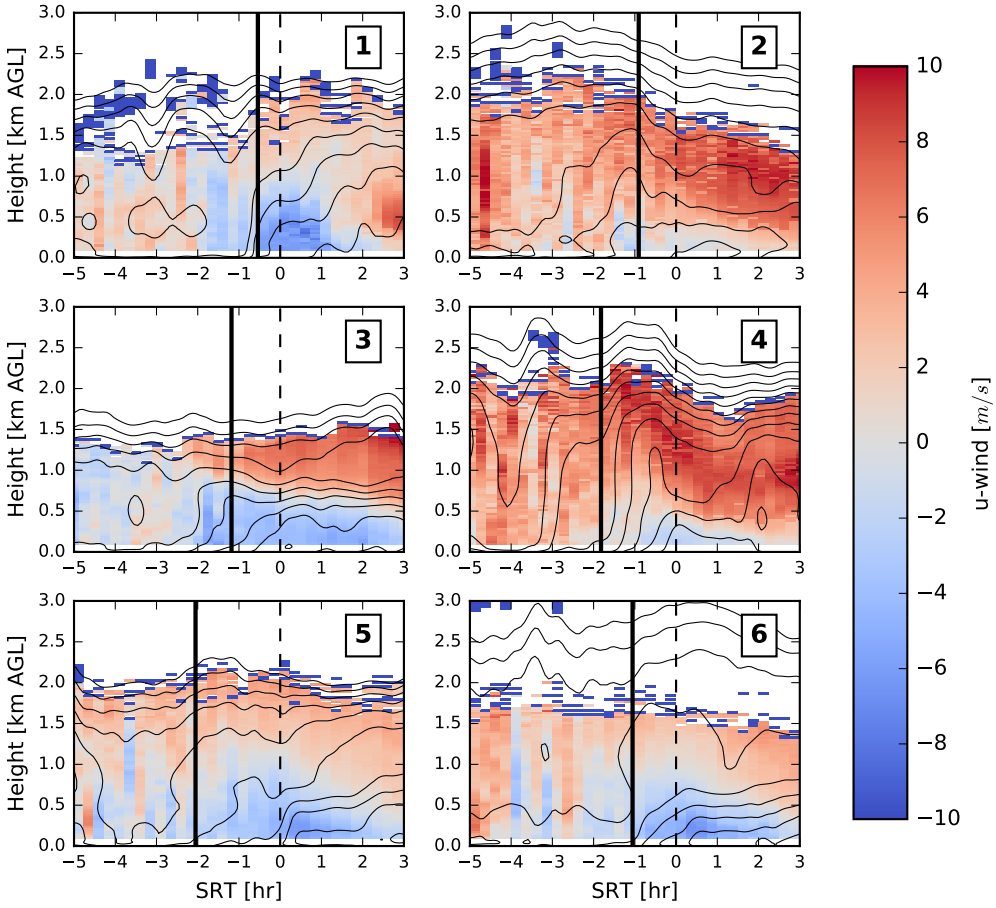

Figure 7.5: As in Figure 7.3, but for the zonal wind obtained from the DLID.

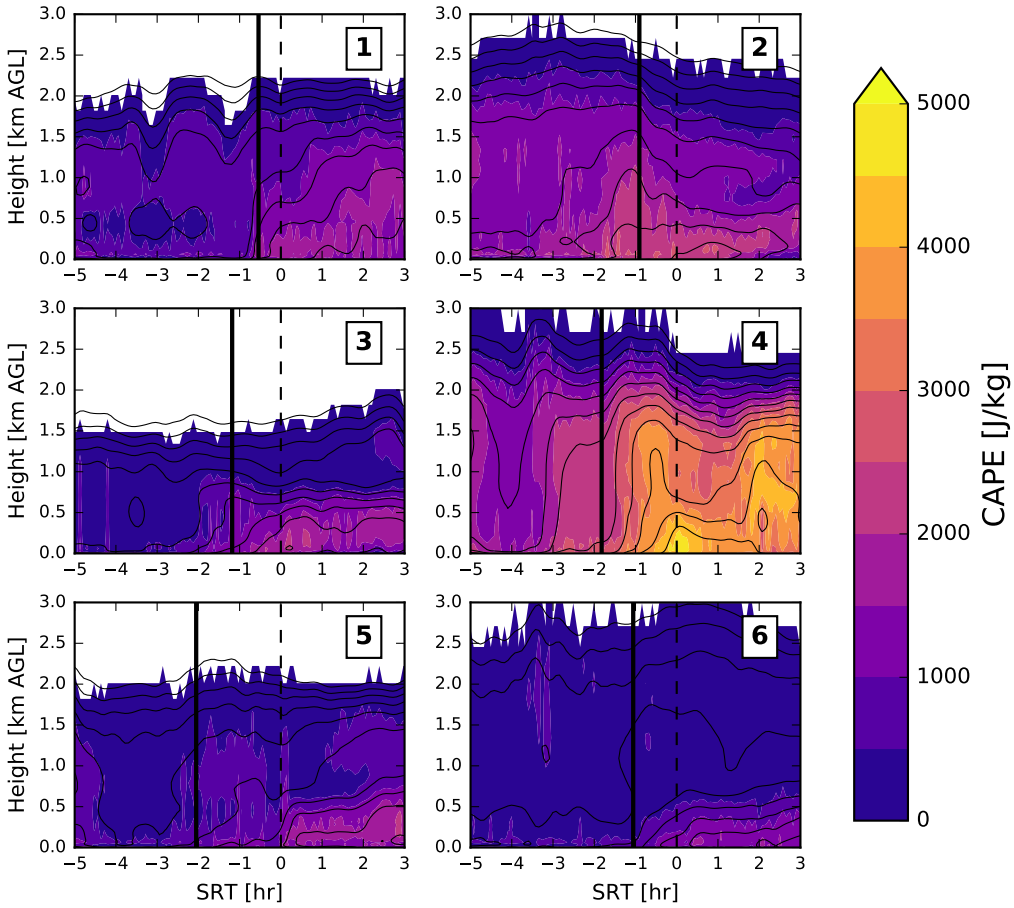

Figure 7.6: As in Figure 7.3, but for CAPE computed by lifting the parcels from every data point in the profile. Places where no contours exist (white) indicates absolutely stable parcels.

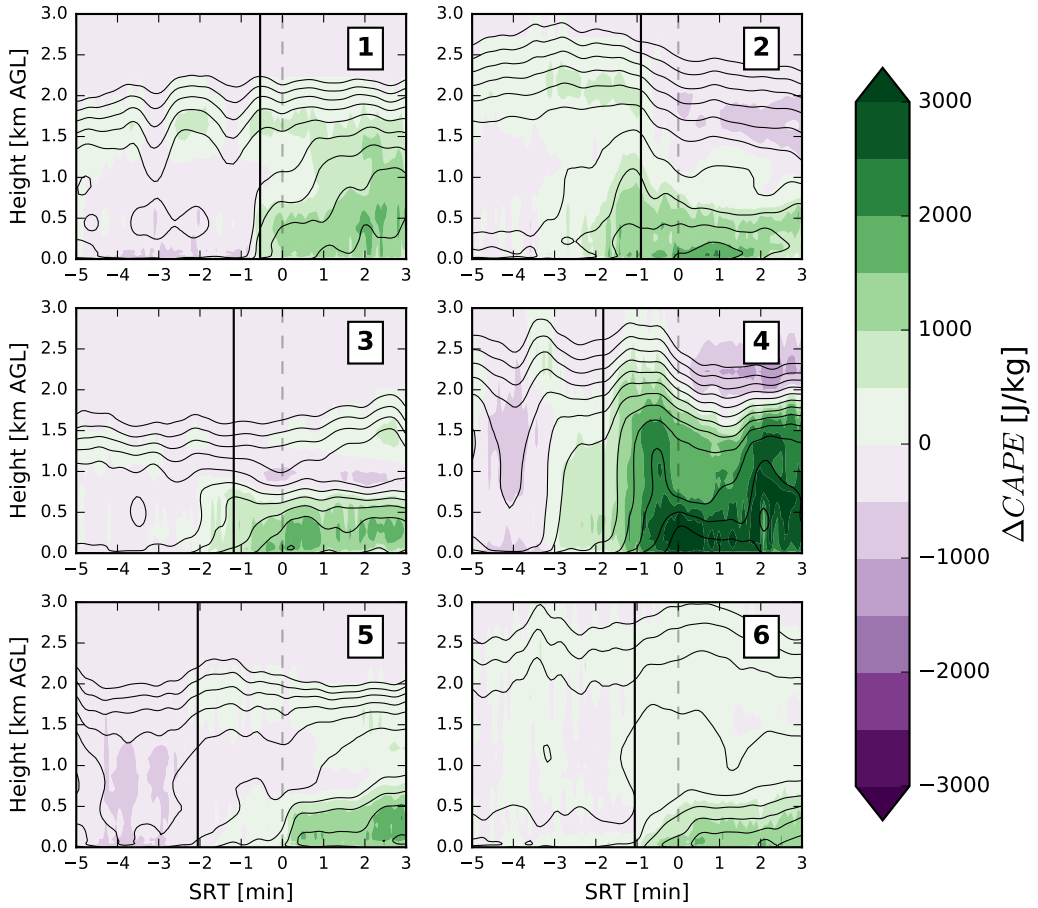

Figure 7.7: The difference between observed CAPE (Figure 7.6) and CAPE computed holding the water vapor profile 5 hours prior to sunset constant throughout the next 8 hours. Green indicates locations where changes in q_v contributed to an increase in CAPE despite changes to the temperature profile.

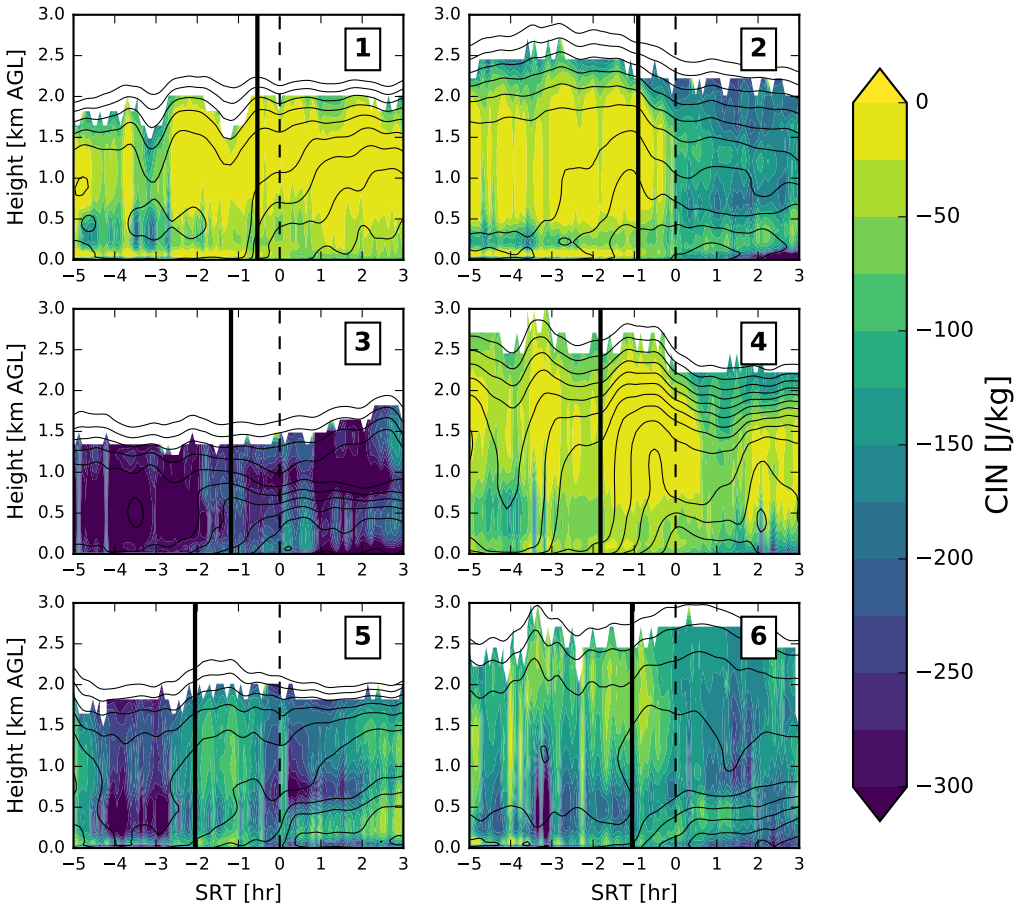

Figure 7.8: As in Figure 7.6, but for CIN.

7.4 Composite Plots and Discussion

To summarize the 31 cases analyzed, composite plots averaging the various datasets were constructed. Figure 7.9 illustrates the average evolution of the AET for several different variables. In Figure 7.9A, the evolution of the potential temperature profile generally shows the break down of a surface-based mixed layer about an hour prior to sunset and rises in q_v starting about 2-3 hours prior to sunset. However, AERIoe retrieves a thermodynamic profile in the lowest 500-m of the atmosphere in the first 3 hours of the period shown that deviates from a well-mixed layer. This difference is likely related to a known issue associated with AERIoe-retrieved near-surface temperature profiles. This bias was mentioned in Chapter 4 and was shown not to significantly impact the quality of AERIoe retrievals or conditional instability estimates from them.

Figure 7.9B shows the average evolution of water vapor before and during the AET. The lowest 500-m shows an increase in 3 g/kg, while aloft, the increase is weaker. These weaker changes aloft appear to be a consequence of the averaging acting to smooth the various depths of the observed moisture changes. However, the changes in the lowest 500-m appear to begin about 3.5 hours before sunset, while the changes aloft appear to occur two hours prior to sunset. The more rapid changes occur in the lowest 500-m about -1 hour prior to sunset. Both Figures 7.2 and 7.9 indicate that an upward bulge in q_v often appears 1 to 2 hours prior to sunset. Additional analysis of this maximum in q_v may be analyzed in future work on this topic.

In the cases described in the last section, a backing of the low-level winds ($\partial u/\partial t < 0$) coincident with accelerations of the meridional wind component

appeared. Figures 7.9C,D illustrate this evolution further and suggest this backing with time below 500-m between -2 hr SRT and 3 hr SRT occurs often in the selected AET cases. The layer over which the u-wind sign reverses becomes shallower with time after sunset. Figures 7.9E,F enable a consideration of how the decaying turbulence relates to changes in the wind profile. Figure 7.9E show the high values of vertical velocity variance at the beginning of the period and its subsequent decay. Similar to the cases discussed in the previous section, the average vertical velocity variance exhibits a similar decline in turbulence between 1 and 2 km AGL at -3.5 hr SRT. A similar reduction in the vertical velocity skewness (Figure 7.9F) appears later on (approaching 2 hours prior to sunset), suggesting that upward transport by turbulent eddies is decreasing with time. In the hours that turbulence is decaying (-4 to -2 hr SRT), the sign of the u-winds steadily reverses.

The evolution of the low-level wind profiles have been discussed in both Shapiro et al. (2016) and Bluestein et al. (2017). Similar to this study, Bluestein et al. (2017) sought to understand the AET changes within the question of the 6 o'clock magic phenomenon. In their study, they aimed to explain the anomalous turning of the low-level winds around sunset as it may modify the low-level wind shear to the point that storm characteristics change. Using WRF simulations, they attributed the backing of the winds close to the surface to changes in the momentum stress occurring throughout late afternoon (changes in friction, vertical mixing, and surface drag per Bell and Bosart, 1988, and Bluestein and Crawford, 1997). They also mentioned that a similar evolution of the wind profile could be reproduced using the Shapiro et al. (2016) model of the NLLJ. At first glance, the wind profiles in Figure 7.9C,D appear similar to the developing NLLJ in Shapiro et al. (2016). However, the acceleration

of the low-level winds shown in Figure 4 of Shapiro et al. (2016) beginning at sunset do not occur at the same time as Figure 7.9. Instead, the observed low-level accelerations begin on average about 2 hours prior to sunset. This timing difference may be due to the use of a sawtooth and step function to describe the evolution of buoyancy and turbulent diffusivity in the Shapiro et al. (2016) model. Resolving these differences are outside the goals of this study.

Figure 7.9G illustrates the evolution of surface fluxes with time. The evolution of the surface fluxes suggest that during these AETs, a period exists that while the sensible heat flux may be negative, the latent heat flux is still positive. This result indicates that when considering surface fluxes, AETs in the SGP are similar to those described in Fitzjarrald and Lala (1989) and Acevedo and Fitzjarrald (2001). However, similar to Busse and Knupp (2012), using only the time of the evening transition to describe the evolution of the PBL is too simplistic. Figure 7.9 and the cases discussed in Section 7.3 shows that prior to the evening transition, turbulence has already undergone a noticeable decrease in intensity, low-level winds have backed, and moistening throughout the PBL has already begun. Because of this, the ET does not appear to be a threshold that controls the evolution of the SGP AET. Instead, both the changes encompassing the entire AET must be considered.

With respect to conditional instability, average plots of the 31 cases considered appear similar to the six cases shown in the last section. Figure 7.10A,B shows the average evolution of CAPE and CIN throughout the AET. Most notable in these plots are a maximum in CAPE appearing in the first four hours of the AET (-3 to 1 hr SRT). After sunset, a layer of parcels exhibiting large CAPE (greater than 1500 J/kg) appears just above the surface. These times

where CAPE is larger tends to also have CIN values closer to 0 J/kg. In Figure 7.10B, a layer of parcels with small CIN appears in the two hours prior to sunset above 500 m AGL. After sunset, parcels near the surface tend to undergo a large increase in CIN. When moisture is considered not to change throughout the 8 hour period depicted in Figure 7.10, CAPE undergoes a constant decrease throughout the lowest 2 km AGL (Figure 7.10C). For CIN though, Figure 7.10D suggests that prior to sunset, keeping q_v constant generates parcels with even less CIN than in Figure 7.10B. As these experiments have less moisture throughout the profile, the virtual temperature at the capping inversion is cooler and is therefore less resistant to lifted parcels. However, about an hour prior to sunset, differences appear, and the impact of the additional moisture on CIN throughout the former CBL is large (approximately a 150 J/kg difference).

These composite plots also offer a return to the primary motivation of this work: the evolution of low-level wind shear relative to moisture during the AET and its possible impact on storms. Figures 7.10 and 7.9 suggest that these increases in water vapor between -3 and 1 hr SRT create increases in CAPE and enable parcels to have smaller inhibition for a longer period of time (CIN doesn't decrease as rapidly). Both environmental changes are favorable for storm intensification, likelihood for tornadogenesis, and increasing storm longevity (Bunkers et al. 2006a,b; Ziegler et al. 2010; Thompson et al. 2003, 2012b; Markowski and Richardson 2014). Interestingly though, when the timing of increases in low-level shear (Figure 7.9H) is compared to instability (Figure 7.10A,B), differences appear. While increases to CAPE/CIN and q_v appear between -3 hr to 1 hr SRT, rapid increases in the bulk wind difference between 0-500 m occur later (between -1 to 2 hr SRT). The rapid increase in shear between

-1 hr SRT (approx. 7:30 PM local time) and 2 hr SRT (approx. 9:30 PM local time) appear similar to the changes in shear between 7 PM and 10 PM local time modeled by Bluestein et al. (2017) (see their Figure 13). In addition, Figure 7.9H also suggests that when considering only shear, environments supportive of tornadoes occur on average after sunset, as the 0-500 m BWD begins to exceed 6 m/s (Esterheld and Giuliano 2008). While there is some temporal overlap, these composite charts suggest that on average at the SGP site in the summertime, increases in moisture precede increases in low-level shear during the AET. These changes suggest that the environmental changes to convective ingredients that favor the longevity and intensification of deep, moist convection may exhibit a dependence on time. More research is needed to clarify this temporal dependence.

In summary, this analysis of the data collected at the ARM SGP site in northern Oklahoma adds additional considerations to **H1** and **H2**. It is clear that these increases in moisture occurring during the AET do increase conditional instability, and in some cases, quite dramatically. However, in the analysis with the RLID data at the beginning of this chapter, it is apparent that **H1** requires additional testing. The largest and deepest increases in water vapor that were observed from the ARM SGP dataset were present only after the winter wheat had been harvested. As of now, this lack of support for **H1** suggests additional investigation is needed to clarify why these rapid and deep increases occur at the ARM site despite the harvested fields present in the summer months.

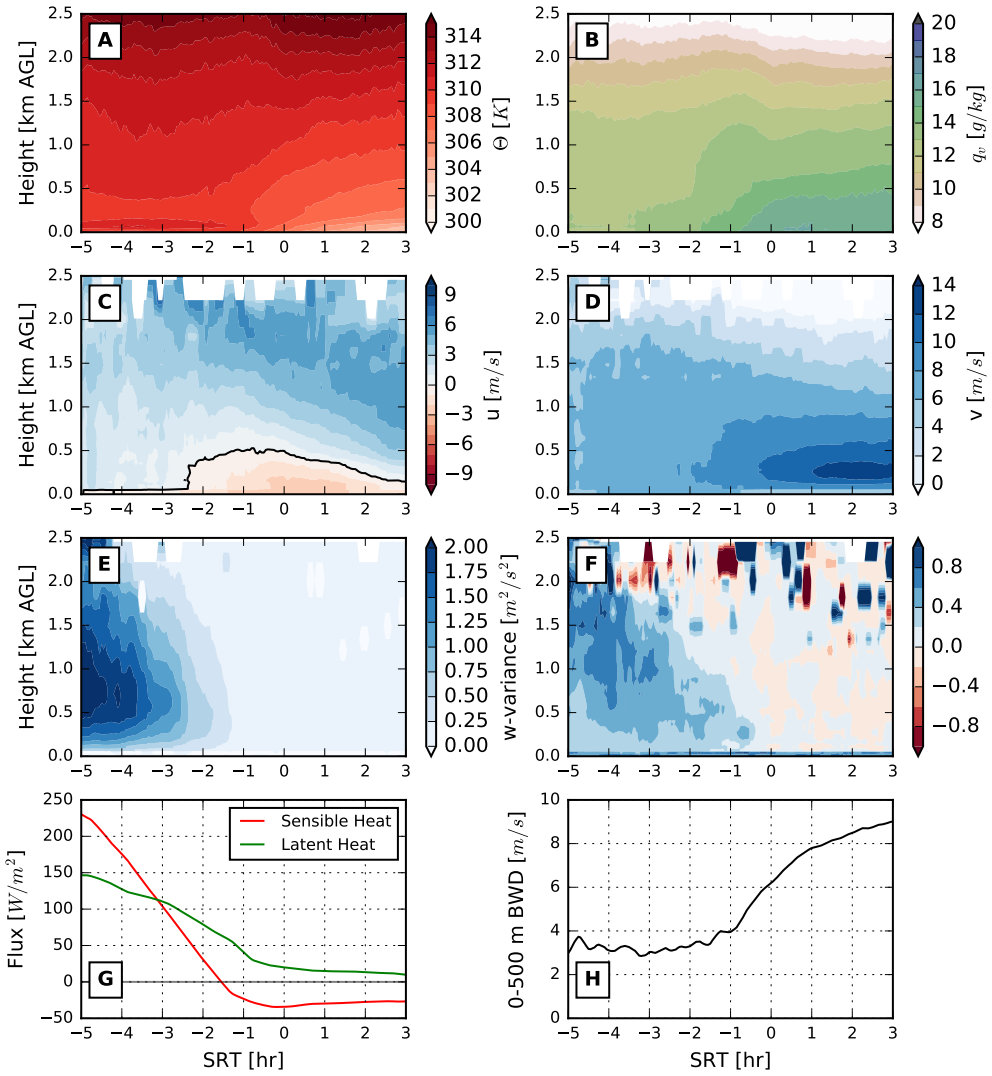

Figure 7.9: Composite plots showing the average evolution of variables during the AET using the 31 AET cases listed in Table 7.1. A and B indicate the potential temperature and q_v profiles from the AERIoe retrievals. C and D show the zonal and meridional winds from the DLID. E and F show the variance and skewness of vertical velocity from the DLID. Skewness is reported as unitless from the DLID. G and H show the average sensible and latent heat fluxes from the ECOR dataset and the bulk wind difference (BWD) between 0 and 500-m from the MET and DLID wind observations.

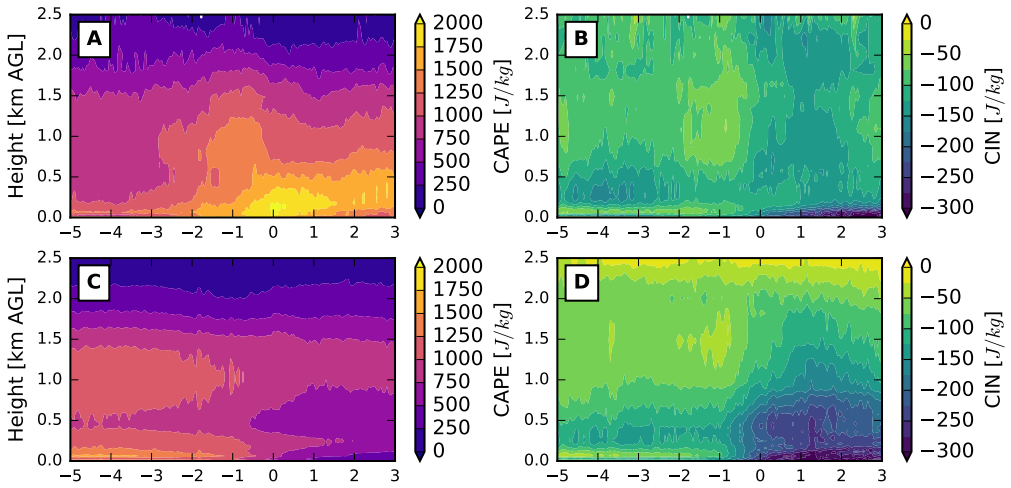

Figure 7.10: Similar to Figure 7.9 but showing the average evolution of CAPE and CIN (A, B), and the average evolution of CAPE and CIN assuming that the water vapor profile at the beginning of the observed period (-5 hours prior to sunset) did not change for the entire 8 hour period shown (C, D).

Chapter 8

Processes Affecting Moisture during the AET

With both the vertical and horizontal dimensions of q_v jumps in the SGP AET characterized, it remains to be answered as to the reasons why these jumps occur at the ARM site. Although numerous other studies (Fitzjarrald and Lala 1989; Acevedo and Fitzjarrald 2001; Bonin et al. 2013; Wingo and Knupp 2015) argue that q_v jumps occur due to the turbulent moisture flux convergence term, the vertical depth and density discontinuity-like nature (Margules 1906; Margules et al. 2016) of these jumps warrant a reassessment of this hypothesis. In order to quantify and assess the relative contributions of moisture advection and turbulent moisture flux convergence on the moisture evolution during the AET, the combination of an extended remote sensing network at the ARM SGP and numerical simulations are used to analyze two cases from the last chapter (7-20-2016 and 8-18-2016). These two cases are selected as they were included in the composite analysis in the last chapter and were two cases provided in the LASSO Alpha 2 release. These simulations and observations aim to build upon the work of Acevedo and Fitzjarrald (2001) with the goal of using more representative values of water vapor advection present in LES. Quantifying more realistic values of water vapor advection present will enable better comparisons between the contributions of advection and turbulent flux convergence on q_v. In this chapter, the hypothesis (**H3**) that advection is responsible for the increases in q_v at the ARM SGP site is tested.

The data created in Chapter 6 strongly suggests that the ARM site is an ideal location to study the transport of moisture gradients created by different land surface properties during the AET. Composite maps using 2D-VAR analyses (see Chapter 6) from before and after the WWB harvest indicates that moisture advection and moisture gradients in the SGP AET are dependent upon the timing of the WWB harvest (Figures 8.1 and 8.2). Prior to the harvest (Figure 8.1), the largest values of moisture advection and moisture gradients during the AET tend to occur on the western edge of the WWB, far away from the ARM site. After the harvest (Figure 8.2), moisture advection and moisture gradients appear towards the eastern edge of the WWB. Because of this shift, a local maximum in moisture advection now often occurs over the ARM site in the hours around sunset. Although plots illustrating moisture advection from other months are not shown in this dissertation, this shift in where moisture advection occurs in the AET is quite distinct between the months before and after the WWB harvest. Because of the location of the ARM site relative to this shift, this analysis will focus only on AET cases occurring after the WWB harvest (Chapter 7). This focus will seek to clarify why large, 1 km-deep q_v increases occur during the AET at the ARM site.

The following sections describe the method and results for the experiments used to answer this question. In the first section, a network of sites hosting additional ARM remote sensors that spans across the eastern border of the WWB is introduced. The processing steps used for this data are also summarized. Next, this data is used to quantify the magnitude of water vapor advection across the WWB. In addition, the data is used to also quantify the cross-WWB flow and q_v gradient. With an expectation of the magnitude of q_v advection near the C1

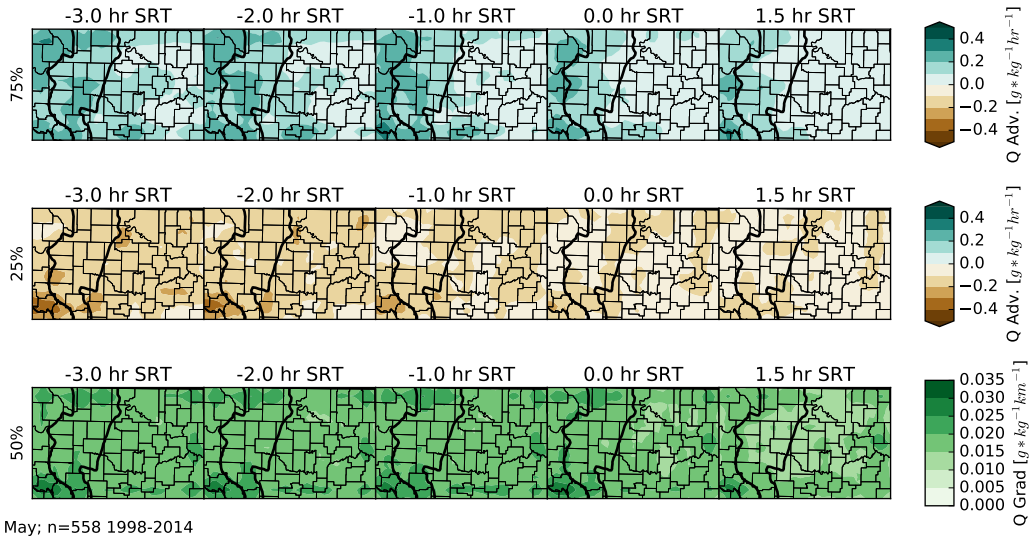

Figure 8.1: Composite 2D-VAR analyses from the Oklahoma Mesonet data (Chapter 6) showing how the distribution of moisture advection and moisture gradient magnitudes evolve throughout May AETs in Oklahoma. The top and middle rows indicate the 75% and 25% percentiles of moisture advection, respectively. The bottom row shows the median moisture gradient magnitude. The columns indicate time in sunset relative time (SRT) and the bold black lines denote the boundaries of the WWB.

site in hand, this study will turn towards analyzing the results from the LASSO runs to understand the key processes (advection or turbulence moisture flux convergence) that facilitate the 1-km deep increases in q_v observed at the ARM site. In the final section of this chapter, a conceptual model to explain these rapid increases in q_v at the ARM site is introduced that synthesizes the results from the previous chapters.

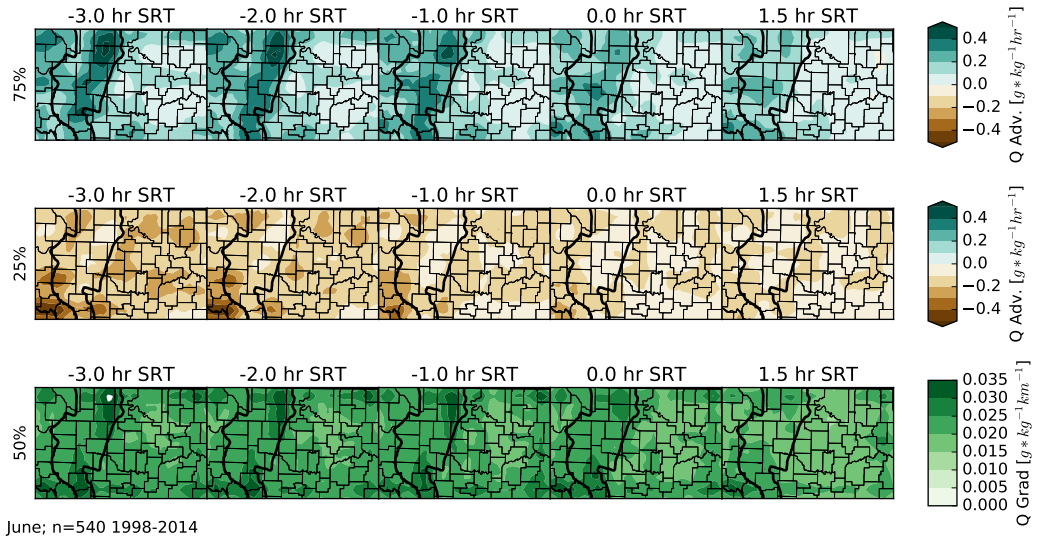

Figure 8.2: Similar to Figure 8.1, but for the month of June.

8.1 Experiment Setup and Methods

Figure 8.3 shows the location of the ARM SGP Central Facility (C1) site in northern Oklahoma. The overlay in the image shows the MODIS NDVI 8-Day Rolling average product from 31 May 2017 to illustrate the ARM site's location relative to the spatial differences in vegetation caused by the harvest of the winter wheat belt (WWB). The sharp decrease in brightness of the green pixels (NDVI is increasing) just southeast of the C1 site indicates this sharp boundary in land surface properties. Visually, this boundary is approximately 15-20 km southeast of the C1 site and denotes the eastern edge of the WWB. Although the MODIS NDVI product is from 2017, similar datasets and papers (e.g., McPherson et al. 2004) suggest that this boundary has not significantly changed and is applicable to 2016.

The ARM Extended Facilities (E32, E37, and E39) indicate locations where ARM instrumentation similar to the C1 site (e.g., AERI, DLID, MET) is also deployed. With the exception of the RLID data, similar processing steps to

those described in Chapter 4 and 5 were used on the AERI and DLID data to obtain high-frequency boundary layer soundings. This exception is required as RLIDs were not deployed to the extended facilities and therefore cannot be included in AERIoe retrievals at the Extended Facilities (Turner and Blumberg, 2018, in review). Because of this, AERIoe retrievals only used AERI spectra, surface MET data, and RAP profiles to obtain profiles of temperature and humidity. While this reduced the vertical resolution of the retrievals and increased the level-to-level correlation of the retrieval error covariance matrix compared to those at the C1 facility, retrieval characteristics were similar to those described in Blumberg et al. (2017b). Comparisons of the retrievals performed at Central and Extended Facilities did not suggest that these differences in retrieval configuration created any spurious horizontal gradients in temperature or humidity, suggesting that the AERIoe retrievals from the Extended Facilities produced reasonable results that could be used for additional analysis.

The distribution of these sites with respect to the WWB enables a look at the cross-WWB flow; the land-surface contrasts apparent in Figure 8.3 may enable the development of a vegetation breeze (Segal and Arritt 1992). Vegetation breezes are similar to sea breezes, and both fall under the category of a nonclassical mesoscale circulation (NCMC). NCMCs are primarily forced by diurnally driven differences in the surface sensible heat flux. NCMCs have been shown to assist in the development of convective clouds and storms (e.g., Anthes 1984; Yan and Anthes 1988; Carleton et al. 2008; Wang et al. 2011). Past studies of vegetation breezes have used both an observational and modeling strategy (McPherson 2007). However, observations of vegetation breezes often do not match the strength of those produced in idealized simulations (Garcia-Carreras et al. 2011). Reconciling these differences are difficult as larger-scale flows may

mask the circulation (Segal et al. 1988) and the land surface characteristics may not compare well to those depicted in idealized simulations. Because the scale of the WWB is on the order of 100-km wide and past work has shown that this length scale is most effective to develop circulations that can develop deep, moist convection, the presence of vegetation breezes during the AET is important to consider (McPherson 2007).

Zhuojia and Xinyuan (1995) studied the evolution of vegetation breezes over the diurnal cycle using numerical simulations of a wheat/arid land-surface boundary. Their simulations indicated that during the daytime, a 1-km deep horizontal gradient of temperature and water vapor developed along the land-surface boundary. In addition, a mesoscale circulation developed, transporting air from the wheat to the arid area. After sunset though, the circulation rapidly decreased and eventually vanished. In another simulation performed by the same authors, the circulation that developed in the daytime reversed after sunset, creating a flow from the arid land-surface to the wheat. When applied to the ARM site, these simulations indicate that a diurnal oscillation may be present along the edge of the WWB in calm conditions.

The ARM site is equipped to analyze the presence of vegetation breezes along the border of the WWB. Evidence of this circulation may be found by analyzing the DLID winds at the C1 (harvested wheat) and the E39 (native vegetation) sites. Given the diurnal oscillation of the low-level flow predicted by Zhuojia and Xinyuan (1995), if a vegetation breeze is the dominant process across the eastern WWB boundary, there should be a reversal of the low-level wind direction from westerly to easterly as the PBL undergoes the AET. Consideration of how vegetation breezes evolve along the WWB presents a possible extension of our understanding of the processes ongoing during the ARM AET. Such changes

in diurnal wind direction and may create an oscillation of moisture across the land-surface boundary.

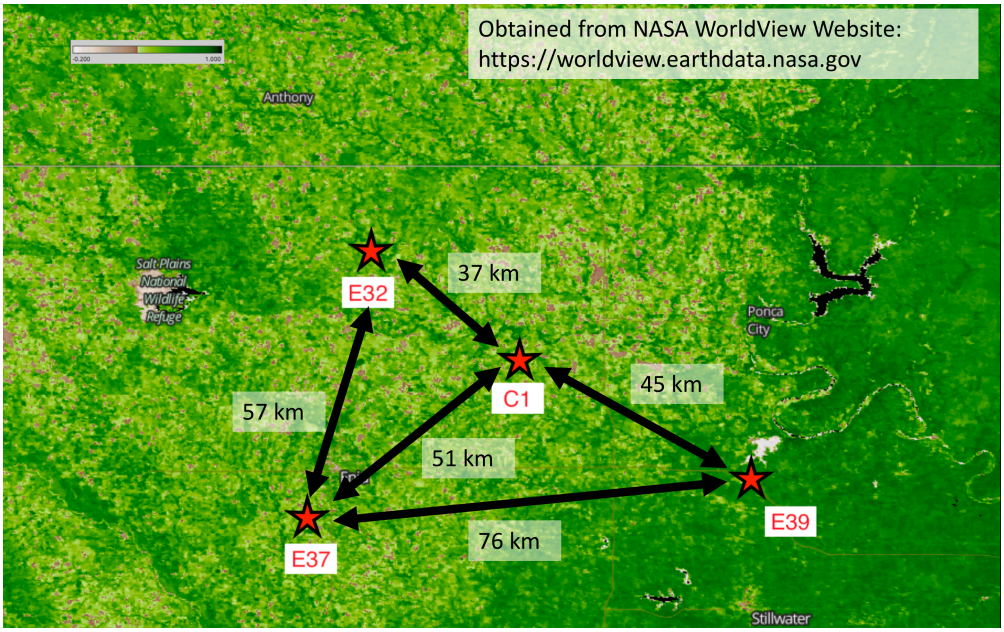

Figure 8.3: Selected ARM observation sites used in understanding the processes relevant to q_v jumps occurring in the 2016-2017 SGP dataset analyzed in the last chapter. C1 indicates the location of the ARM SGP Central Facility, while E37, E32, and E39 are the ARM extended facilities surrounding the C1 site. Black arrows and distances indicate the distances calculated between the different sites. These site locations are overlaid on the MODIS Rolling Average 8-Day NDVI dataset for May 31st, 2017 to illustrate the distribution of the sites relative to healthy vegetation and the eastern WWB boundary. The boundaries of the WWB can be roughly found in Figure 6.6.

8.2 Gradients in q_v and Momentum Across the WWB Border

The first step in the tests to assess **H3** was to estimate the water vapor advection across the WWB from the DLID and AERIoe data generated at the C1 and E39 sites. To do this, the AERIoe and DLID data were linearly interpolated to a uniform height and time grid (about 0.2 to 1.0 km AGL, $\Delta z = 0.01$ km and between -5 hr SRT and 3 hr SRT, $\Delta t = 5$ min SRT). The C1 and E39 DLID winds were then projected onto the C1-E39 cross section, which is roughly a 20 degree angle relative to the east-west axis. Next, these projected winds were averaged to illustrate the average cross-WWB flow (v_{C1-E39}). After that, the AERIoe profiles of q_v from C1 and E39 were forward differenced to calculate the horizontal q_v gradient ($\nabla_h q_v$) between C1 and E39. Finally, estimates of the $\nabla_h q_v$ and v_{C1-E39} were averaged across 33 cases during the summer months. A majority of the cases included in this dataset overlapped with those selected in Table 7.1, but not all of the cases used in the last chapter were able to be used. This was due to missing AERI and DLID data in the surrounding ARM Extended Facilities. Regardless, these two profiling sites show the average summertime conditions along the eastern edge of the WWB.

Figure 8.5 shows the results from the averaging the AERIoe retrievals and DLID observations. Negative values of v_{C1-E39} indicates a wind with a component towards the harvested WWB (e.g., flowing towards the west) while positive values indicates a component away from the WWB. On average, the wind across the WWB is on the order of -5 to -6 m/s -5 to -2 hr prior to sunset. Approaching 1 hour prior to sunset, the C1 wind begins to accelerate, reaching nearly

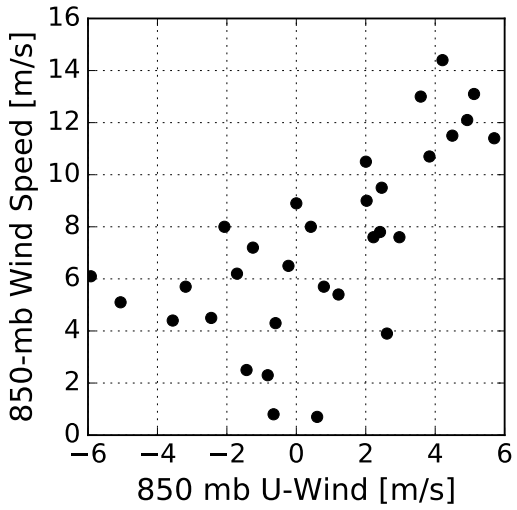

Figure 8.4: The 850-mb wind speed and zonal component wind speed for the 33 summertime cases. Each point represents the wind observed from the 23 UTC radiosonde launched during each case.

10-15 m/s after sunset. For the q_v gradient (Figure 8.5, bottom), a positive $\nabla_h q_v$ indicates a gradient where q_v increases towards the E39 site. For much of the time before sunset, a moisture gradient between the C1 and E39 sites is present. In some cases analyzed, this gradient is on the order of 3 g/kg across the WWB boundary. The gradient in the hours prior to sunset occurs often in this dataset, as the hatching in Figure 8.5 indicates places where the q_v gradient vector still points towards E39 if the $1 - \sigma$ perturbation is added to this plot. In the hour prior to sunset, the moisture gradient tends to vanish in the lowest 500-m. Aloft, the $\nabla_h q_v$ vector still points east, but not as strongly as before.

These results suggest that on average, the ARM data does not depict conditions similar to the vegetation breezes simulated in Zhuojia and Xinyuan (1995). Although the expected daytime cross-WWB flow from the healthy vegetation to the harvested WWB does occur, this flow does not reverse after sunset. However, an expected 1-km deep moisture gradient along the edge of the WWB does develop during the daytime (Figure 8.5). This discrepancy may be due to

the large-scale flow masking any circulations that do develop. Figure 8.4 shows that while the 850-mb winds may be occasionally weak, most cases considered in this chapter have a noticeable cross-WWB flow. Figure 8.4 indicates that the zonal wind speeds at the ARM site are often outside of those specified in the Zhuojia and Xinyuan (1995) simulations (e.g., weak geostrophic winds near 0 m/s). Given that the orientation of the WWB is not aligned perfectly along a north-south axis, meridional winds also contribute to a stronger cross-WWB flow. These observations suggest that for these cases, vegetation breezes at the ARM site are unlikely, and cannot be determined with enough certainty in these conditions. Additional research is needed to clarify if and how vegetation breezes develop along the border of the WWB.

Next, the average conditions in Figure 8.5 are used to create an estimate of the expected q_v advection values. Figure 8.6 shows estimates of this term by creating various combinations of the average cross-WWB winds with the across WWB gradient of q_v in Figure 8.5. Given the average orientation of these vectors, the q_v advection most often may be found to be moistening the PBL as opposed to drying. The rate of moistening by advection in Figure 8.6 is anywhere between -0.8 to 1.6 g/kg/hr. These plots suggest that the moisture advection term is on the order of 1 g/kg/hr.

Compared to Figures 8.1 and 8.2, the estimates in Figure 8.6 are slightly larger. 2D-VAR indicates that the distribution of moisture advection is slightly less than the estimates generated by the ARM network. This difference may be due to the smoothing that occurs when the recursive filter is applied when the 2D-VAR method is applied to the Oklahoma Mesonet data. This problem

is similar to the aforementioned issue of variational algorithms (e.g., 3D-VAR) in filtering out the smaller-scale features from the data.

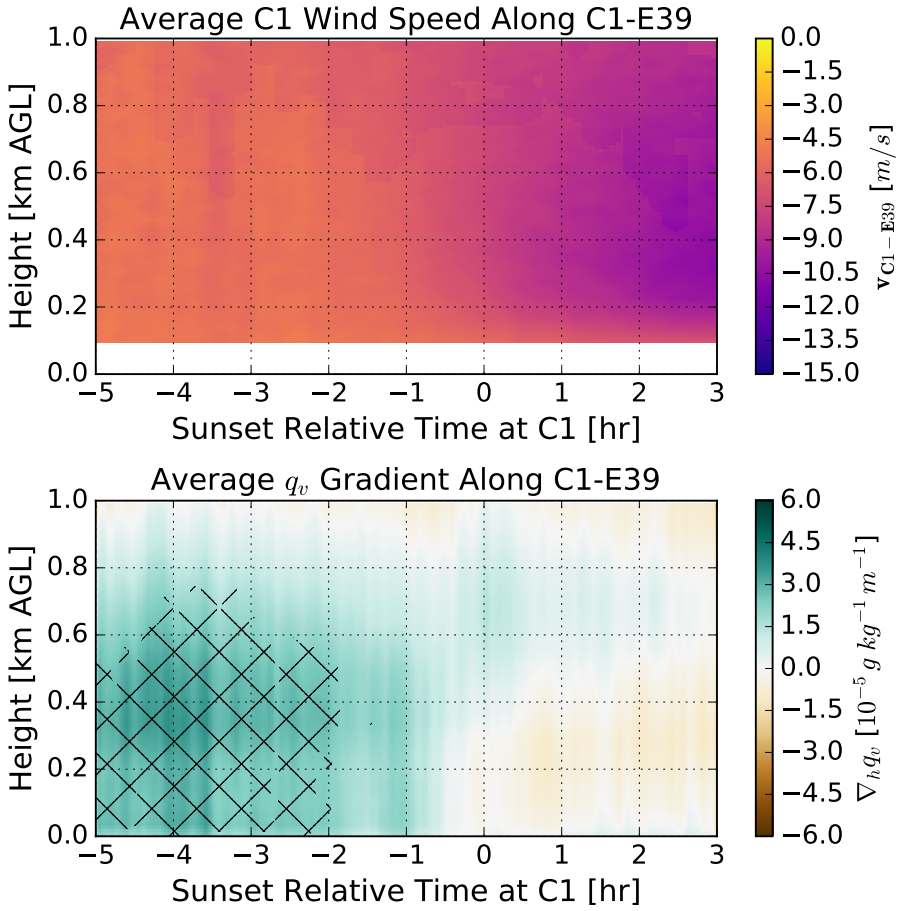

Figure 8.5: Two plots denoting the average wind and moisture conditions across the WWB using 31 cases from the summertime. The top plot shows the average C1 wind component tangent (v_{C1-E39}) to the C1-E39 WWB cross section while the bottom plot shows the average horizontal q_v gradient ($\nabla_h q_v$). Hatching on the lower plot indicates the times and heights when the $1 - \sigma$ $\nabla_h q_v$ indicates a positive value across the WWB, suggesting that the distribution of $\nabla_h q_v$ is shifted towards positive values at these times.

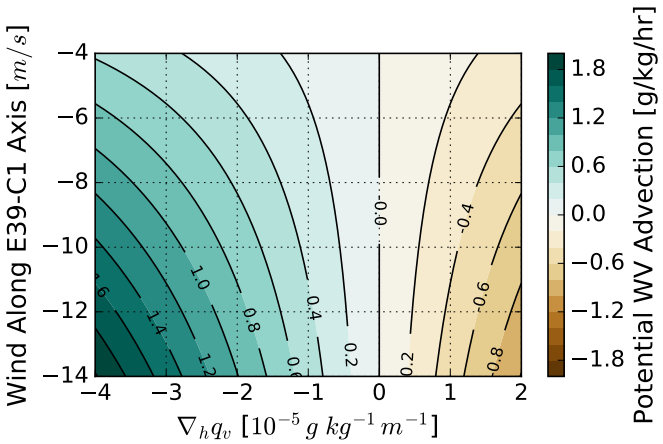

Figure 8.6: Estimates of the water vapor advection term at the C1 site generated by combining various average estimates of ∇q_v and v_{C1-E39} from Figure 8.5.

8.3 Profiles of q_v Advection

Next, the profile of horizontal water vapor advection ($\mathbf{V} \cdot \nabla q_v$) was directly calculated during the AET time period. This calculation used both AERIoe retrievals and DLID VAD products from the C1, E37, and E39 sites. Advection was calculated by using the equation from Michael (1994), which is a form of Green's theorem:

$$\int \mathbf{V} \cdot \nabla_h q_v \, da = \oint q_v \mathbf{V} \cdot \mathbf{n} \, ds = \sum \overline{q_{vi}} (\overline{U_i} \Delta y_i - \overline{V_i} \Delta x_i). \tag{8.1}$$

Here, $\mathbf{V}$ is the height dependent 2-D horizontal wind vector derived from the DLID VAD algorithm, and q_v is the water vapor mixing ratio being advected that was retrieved from AERIoe. $\mathbf{n}$ is the unit vector normal to the individual line elements, ds, along the specified polygon (in this case a triangle). On the right hand side is the equation used to calculate the area-averaged advection of q_v in discrete coordinates. Overbars indicate the arithmetic means along each linear segment i of the polygon sides (e.g., $\overline{q_{vi}}$ indicates the average value of q_v along segment i). U and V are the x and y components of the wind vector $\mathbf{V}$. Δx_i and Δy_i are the projections of each polygon side on the x and y axes. To isolate advection, the result on the right hand side of the equation is divided by the area of the polygon, computed by $\int da$.

Prior to each calculation of water vapor advection, the AERIoe and DLID data from each site was gridded to a uniform height grid (about 0.2 to 1.0 km AGL, $\Delta z = 0.01$ km) and time grid ($\Delta t = 5$ min) using nearest neighbor interpolation. This height grid was created to look at the q_v advection between approximately 0.25-1 km AGL as the moisture increases found in Chapter 7

appeared at these depths. Because the elevation changes between the various ARM sites, the height grid considered was not extended to the surface.

As both AERIoe and the DLID VAD algorithms provide estimates of the $1-\sigma$ uncertainty of their temperature, water vapor, and wind products, the uncertainties in these observations can be propagated through Equation 8.1. To do this, a set of 500 water vapor advection profiles were created using Monte Carlo sampling of the AERIoe and DLID data. The method used is similar to the method of calculating the uncertainty of convection indices discussed in Chapter 5. When cases are analyzed individually, the advection values computed in this manner were found to be mostly noisy, and are not included for this reason.

However, a signal is extracted by averaging the profiles of moisture advection computed from these 33 cases. This provides both an estimate of the typical depth and timing of changes to the moisture advection term. Immediately, it is clear that the order of magnitude of advection calculated this way is similar to that estimated by Figure 8.6. The layer of positive water vapor advection that develops coincides well with the composite changes in q_v in Chapter 7, Figure 7.9b. The order of magnitude of q_v advection is also the same order of magnitude of the average estimates of the local tendency of water vapor (1.3 g/kg/hr) listed in Table 7.1. However, Figure 8.6 only suggests this layer of moisture advection occurs over a depth of 500-m AGL while the average depth of the observed q_v increases is over 1 km. This is an artifact of the averaging to create this Figure, and some individual cases suggest that the advection layer reaches 1 km. While these experiments have not controlled for the turbulent moisture flux convergence term, the similarities between the cases discussed in

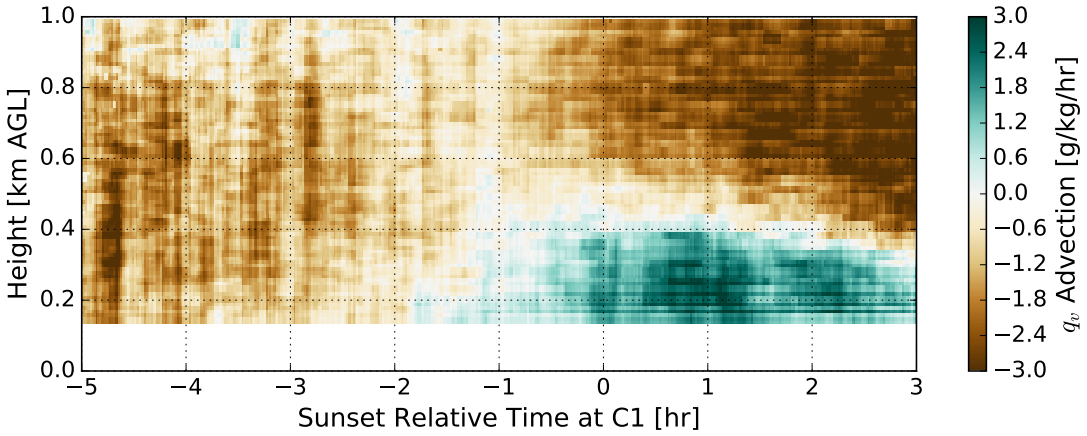

Figure 8.7: Average q_v advection from the same 31 cases used in Figure 8.5. Advection was calculated using the C1-E39-E37 triangle and Equation 8.1.

Chapter 7 and the estimates of q_v advection so far suggest strong circumstantial evidence that advection is the driving process behind the 1-km jumps in q_v at the ARM site after the wheat harvest.

8.4 LES Results

To compare advection to the turbulent moisture flux convergence term, two AET cases (8-18-2016 and 7-20-2016) are analyzed using the LASSO dataset. Because LASSO uses periodic boundary conditions and a homogeneous lower boundary, these simulations are unable to simulate any circulation due to the contrasting vegetation shown in Figure 8.3. Table 8.1 describes the various forcing datasets, microphysics packages, and models that encompass the 12 member LASSO ensemble used. For all members, the Morrison 2-moment microphysics scheme is used. Ensemble diversity was primarily provided by a combination of the MSDA, VARANAL, and ECMWF datasets. However, only MSDA or ECMWF were used to specify the large-scale forcing for the ensemble. For 4 of

the LASSO members, the ARM Radar Wind Profilers (RWP) data was assimilated into MSDA. This configuration overall used 3 different types of advective forcing: MSDA without RWP, MSDA with RWP, and ECWMF.

These three various forcing datasets represent the large-scale forcing at the ARM site. Additional diversity was also included by considering different spatial sizes of the forcing. These various sizes are depicted relative to the WWB and the ARM Central Facility in Figure 8.8. The largest scale, 300 km $\times$ 300 km, represents the domain of the VARANAL dataset. This spatial area encompasses a significant area of the SGP relative to WWB (Figure 8.8). Due to its size, it is not used in the LASSO runs as the large-scale forcing. Rather, it is only used to provide forcing at the lower boundary of the domain. The smaller areas that are used by the ECMWF (114 km $\times$ 114 km and 16 km $\times$ 16 km) and MSDA (150 km $\times$ 150 km and 75 km $\times$ 75 km) better represent conditions along the the eastern edge of the WWB. More importantly for future applications of the LASSO and this study, the MSDA 75 km grid best encompasses the contrasting land surface properties and the various Extended Facilities surrounding the ARM site.

Because a 75 km grid encompasses the contrast in land-surface differences, and the MSDA methodology considers the horizontal surface moisture gradients present across this contrast, it is expected that the MSDA forcing datasets will best represent the advection of moisture through the C1 site. This expectation is also supported by the conclusions in Vogelmann et al. (2015). In this paper, Vogelmann et al. (2015) used LASSO-prototype configurations, SCMs, and observations to study boundary layer cloud processes at the ARM SGP site. By

Table 8.1: The configuration of each member of the 12-member SAM ensemble used in analyzing the 8-18-2016 and 7-20-2016 cases. The columns indicate the member ID number, the model core, the dataset for the large-scale forcing, the scale of the large-scale forcing, the surface forcing dataset, and the microphysics package. Asterisks indicate the MSDA forcing dataset that included the assimilation of the ARM RWP wind profiles.

ID No	Model	Large-Scale	Scale	Surface	Microphysics
101	SAM	ECMWF	16 km	ECMWF	Morrison 2-MOM
102	SAM	ECMWF	114 km	ECMWF	Morrison 2-MOM
104	SAM	MSDA	75 km	MSDA	Morrison 2-MOM
105	SAM	MSDA	150 km	MSDA	Morrison 2-MOM
107	SAM	ECMWF	16 km	VARANAL	Morrison 2-MOM
108	SAM	ECMWF	114 km	VARANAL	Morrison 2-MOM
110	SAM	MSDA	75 km	VARANAL	Morrison 2-MOM
111	SAM	MSDA	150 km	VARANAL	Morrison 2-MOM
120	SAM	MSDA*	75 km	MSDA	Morrison 2-MOM
121	SAM	MSDA*	150 km	MSDA	Morrison 2-MOM
123	SAM	MSDA*	75 km	VARANAL	Morrison 2-MOM
124	SAM	MSDA*	150 km	VARANAL	Morrison 2-MOM

using this ensemble of "best estimate" forcing datasets, they found that out of the three cases considered, the LES runs forced using MSDA better reproduced the PBL evolution during the transitional periods (e.g., the AET), as they were better able to reproduce the near-surface moisture advection.

The large-scale horizontal water vapor advection forcing in the LASSO ensembles are shown in Figures 8.9 and 8.10. In both cases, the four MSDA forcing datasets show similar values in the water vapor advection and timing of the advection. However, the larger-scale MSDA forcing data (150 km) shows slightly smaller q_v advection values than the 75 km MSDA data. In all MSDA datasets, positive q_v advection begins over a layer that extends between 1.0 to 1.5 km AGL two hours prior to sunset, somewhat similar to the composite q_v advection values in Figure 8.7. These values and depths in Figures 8.9 and 8.10 prior to sunset are on the same order of magnitude (0.6-1.0 g/kg/hr) as the values in Figure 8.7.

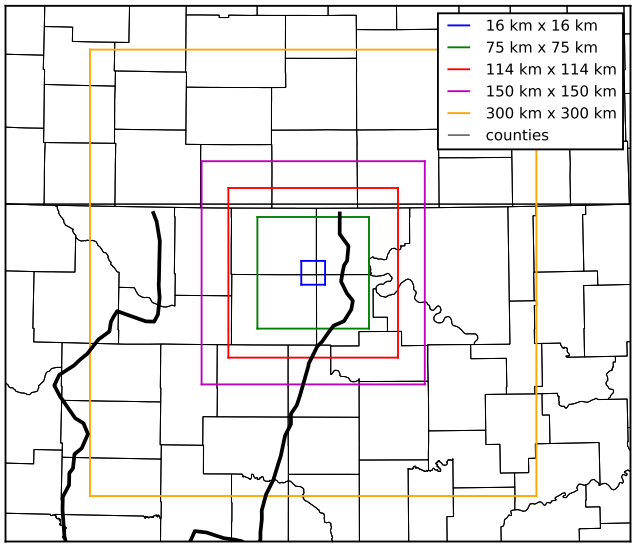

Figure 8.8: A map of the Southern Great Plains area with various sizes representing the large-scale forcing of the area. All forcing areas are centered around the ARM SGP Central Facility site. Solid black contours denote the boundaries of the WWB from McPherson et al. (2004).

In contrast, the ECMWF forcing is more inconsistent across forcing scales. While the 114 km forcing is between -0.2 to -0.4 g/kg/hr, the 16 km forcing varies strongly between -1 g/kg/hr and 1 g/kg/hr. Despite these discrepancies, values of q_v advection beginning an hour or two before sunset over 1 km are the correct order of magnitude. Compared to the ECMWF, the advective forcing from the MSDA seems more realistic in its timing, sign, depth, and order of magnitude when compared to Figure 8.7. However, both the MSDA and ECMWF datasets show similar magnitudes of advection to the values depicted in Figure 8.7 and 8.6. Despite the variability of the forcing datasets, if the turbulent moisture flux convergence values within the LASSO simulations are less than the modeled water vapor advection values, then **H3** (advection is the cause) can be accepted.

Figure 8.11 illustrates the test of this conditional statement. In this figure, the individual terms of the water vapor tendency equation computed from each

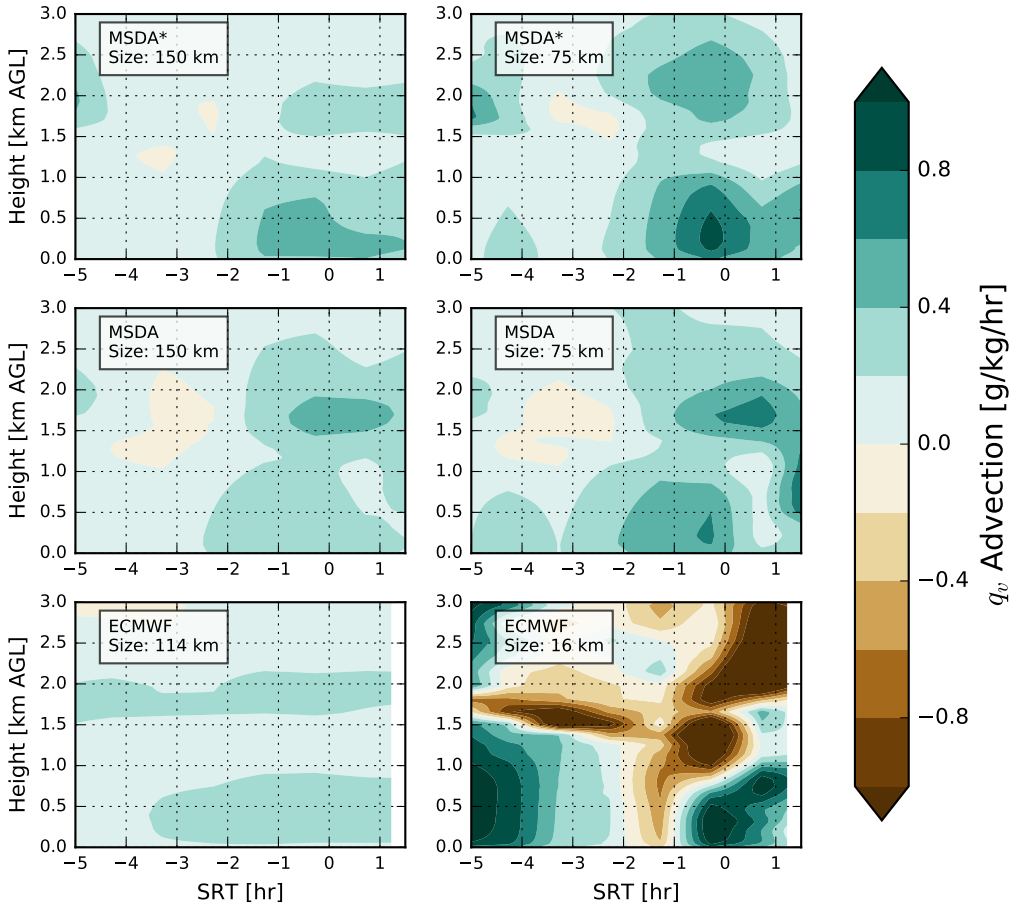

Figure 8.9: Horizontal q_v large-scale advection from the six forcing datasets used in the LASSO ensemble. The forcing shown is for the 2016-08-18 LASSO runs. The top two rows indicate the MSDA 150 and 75 km forcing with and without the ARM RWP data assimilated. The bottom row is the ECMWF 114 and 16 km forcing.

SAM run are averaged together to depict the likely evolution of each term. For both cases, the local changes to water vapor indicate drying throughout the CBL during the first three hours of the period (Figure 8.11, top row). The average magnitude of the drying is on the order of -0.3 g/kg/hr. As the LASSO simulations approach two hours prior to sunset, the PBL begins rapidly moistening at an increasing rate. For the 8-18-2016 case, the local tendency of q_v reaches nearly 0.4-0.6 g/kg/hr in the lowest 800-meters. In comparison,

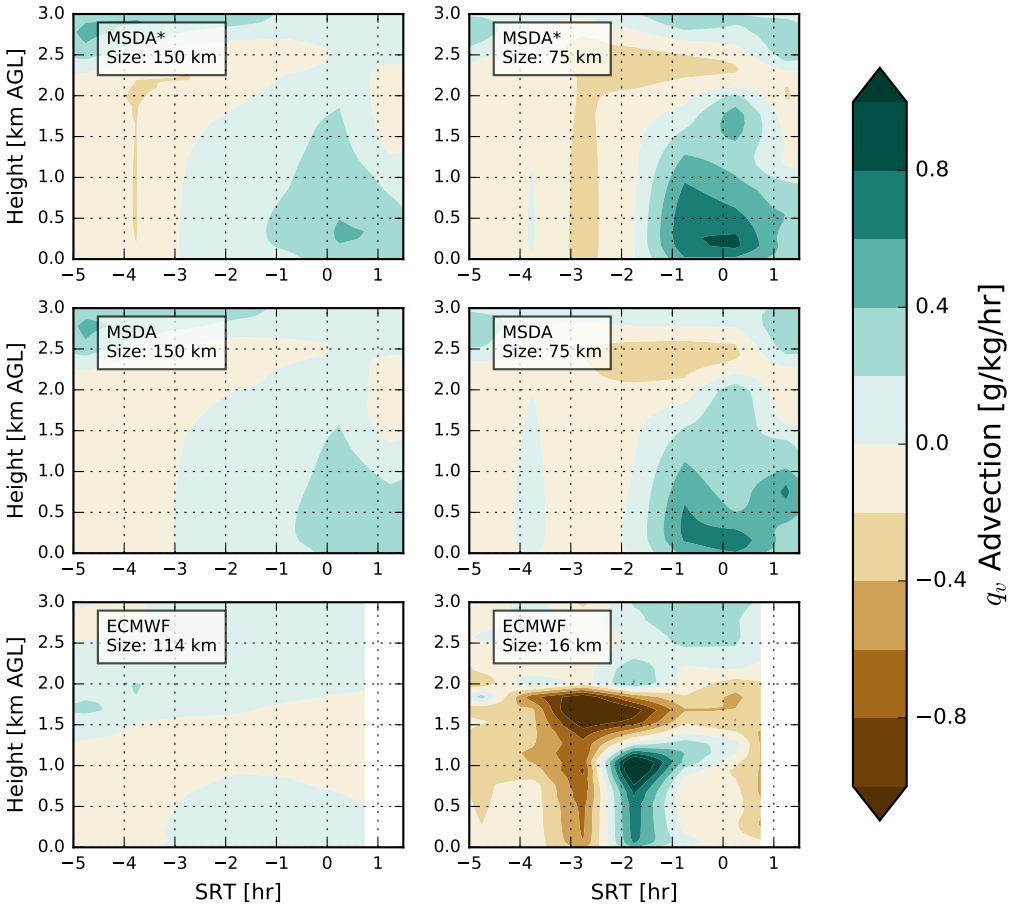

Figure 8.10: Similar to Figure 8.9, but for the 2016-07-20 case.

the 7-20-2016 case reaches a maximum of 0.4 g/kg/hr in the lowest 400-meters. When the average contribution from q_v advection (Figure 8.11, bottom row) is considered, it is clear that the increases in q_v over the lowest 1km are primarily driven by advection (**H3** is true).

So, where does the turbulent water vapor flux convergence term contribute to the decaying CBL? The second row of Figure 8.11 suggests that this term only plays a role in the lowest 100-m of the simulation. For both AET cases, the sign of this term undergoes a reversal similar to the local tendency of q_v (top row, Figure 8.11), however the change to a positive value that begins on average at -1 to -1.5 hr SRT does not extend deep enough into the PBL to

account for the larger changes in water vapor aloft. Individual inspection of the 12 LASSO runs also confirms this conclusion. Importantly, this term does contribute positively to the increase in water vapor and may account for the near-surface increases within the ARM data (0 to 100-m AGL). In addition, the presence of a positive value for this term during this time period confirms past research that has attributed AET moisture increases to this term (e.g., Fitzjarrald and Lala (1989); Acevedo and Fitzjarrald (2001); Busse and Knupp (2012); Bonin et al. (2013); Wingo and Knupp (2015)). From these simulations it is clear that the turbulent moisture flux convergence contributes to the lowest 100-m, but the deeper increases in q_v are attributable to advection.

As it stands, the LASSO ensemble does not have the diversity in surface forcing to help understand the relationship between evapotranspiration and the turbulent moisture flux convergence term. This may be done in future experiments by varying the surface forcing within the LASSO runs systematically to reveal how this term may vary across different AETs. Regardless, the results in Figure 8.11 indicate that **H3** cannot be rejected; the increases in these simulations throughout the lowest 1 km are primarily due to horizontal advection with some contributions by the turbulence moisture flux convergence term near the surface.

When the local q_v tendency (top row) and the contributions from large-scale vertical velocity from the forcing datasets to vertical advection are considered (bottom row), the impact of horizontal advection on q_v on these simulations is further emphasized (Figure 8.11). Vertical q_v advection from these simulations is small; only on the order of 0.2 g/kg/hr and cannot account for the 1-km deep increases in moisture either. This further illustrates that horizontal q_v advection

is the primary cause of the 1-km deep moisture rise throughout the decay of convectively generated turbulence in these LASSO simulations.

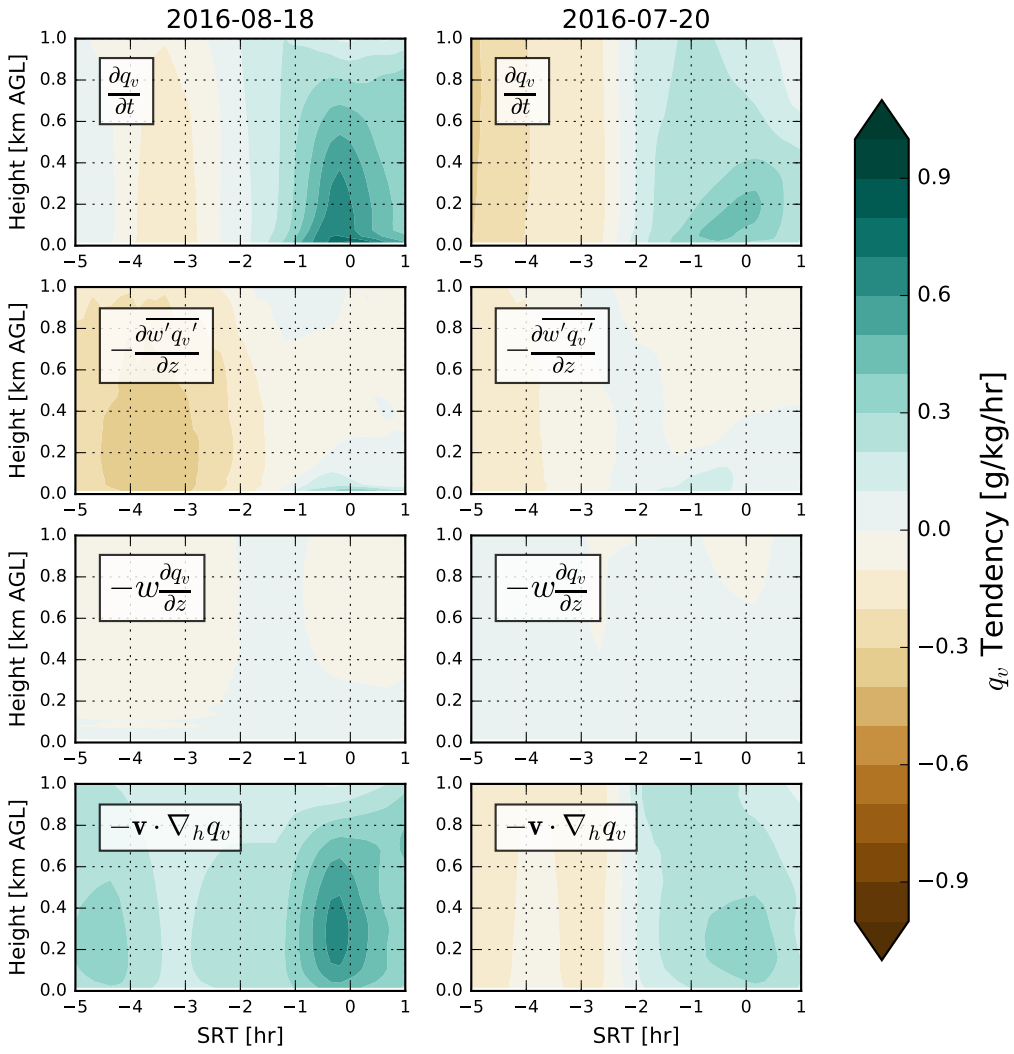

Figure 8.11: Average contributions from the local tendency of water vapor (1st row) the turbulent moisture flux convergence (2nd row), large-scale vertical advection (3rd row), and large-scale horizontal advection (4th row) for the two cases (08-18-2016, left) and (07-20-2016, right) using the SAM ensemble. The local tendency of q_v is computed by performing finite differencing on the 10-minute q_v output (forward and backwards near the edges, central everywhere else.)

8.5 SGP Summer AET Conceptual Model

From the combination of LASSO simulations and ARM observations, a basic conceptual model can be constructed to tie together the spatiotemporal aspects of the summertime AET SGP q_v changes discussed in Chapter 6 and 7. In this section, the results from the past few chapters are synthesized to generate a conceptual model for the AET q_v changes over the WWB after the WWB has been harvested. This model is illustrated using the observations and LASSO simulations discussed in this study.

As was mentioned in Chapter 6, increases in moisture persist over the WWB in the summer months throughout the entire AET (before and after sunset). In the cases analyzed at the ARM site in Chapter 7, it was established that these increases in q_v are not limited to the near-surface; these increases can occur over depths of 1 km. It was also found that these q_v increases tend to begin an hour or two after the CBL turbulence begins to weaken. The decrease in the surface sensible heat flux through the AET, which is due to the decrease in the downwelling shortwave radiative flux, leads to a decay in the turbulent motions in the CBL (Figure 7.9). Proof of causality of this relationship was not shown in this research, but rather assumed via the consensus of numerous past work and texts (e.g. Stull 1988; Sorbjan 1997).

This decay in turbulence also coincides with changes to the low-level wind profile. In Chapter 7, wind profiles derived from the DLID demonstrated that as the turbulence weakens, the winds in the lowest 500-m back with time, often acquiring an easterly component ($\partial u/\partial t < 0$). The meridional winds during this time also begin to accelerate ($\partial v/\partial t > 0$). Similarly, these changes in the wind profile due to changes in turbulent mixing within the PBL during the

AET have also been discussed in past literature (Blackadar 1957; Holton 1967; Maddox 1993; Shapiro et al. 2016; Bluestein et al. 2017).

However, this research indicates that interaction of these changes during the AET near the harvested WWB is important to the redistribution of moisture and conditional instability in northern Oklahoma. As was shown in Figures 8.1, 8.2, and 8.5, two environmental conditions are commonly present during summertime AETs: 1) a gradient in q_v oriented across the eastern boundary of the WWB and 2) flow across this gradient creating positive moisture advection. For the 8-18-2016 case, this gradient shows a change of 3 g/kg between the C1 and E39 sites prior to the surge of moisture westward (Figure 8.12, top row). Development of this gradient is not new knowledge either; McPherson et al. (2004) and McPherson and Stensrud (2005) used Oklahoma Mesonet data and WRF simulations to identify and simulate the effects of the WWB on the daytime mesoscale environment (e.g., different CBL top heights), albeit with a focus on the WWB prior to its harvest.

Figure 8.13 summarizes what happens when the turbulence decays in the presence of this gradient and describes how the moisture tendency equation terms evolve with time prior to the AET period (-5 to -3 hr SRT) and during the AET. Prior to the AET, q_v advection is present due to low-level southerly winds, and mixing at the capping inversion acts to dry the PBL. In the LASSO runs, this mixing can act to balance or even reverse the contributions from advection. Prior to the AET, the conceptual model and dynamics of the CBL can be utilized (Stull 1988). As the turbulence decays faster, two changes occur that enable more effective transport of moisture over the WWB. First, modifications to the low-level wind profile (e.g., backing) orient the low level winds in a direction more normal to the eastern WWB boundary. This reorientation of

the winds acts to increase the advection of q_v during the AET. Second, as identified from the LASSO runs (Figure 8.11, second row), the decay of turbulence throughout the AET coincides with a reduction of entrainment of q_v at the top of the PBL. This acts to increase the turbulent moisture flux convergence term in the positive direction and reduce drying within the PBL. On 8-18-2016, this process acted to produce a rapid surge in moisture and instability westward (Figure 8.12). Given the WWB's orientation, both changes in advection and turbulent q_v flux convergence act in conjunction to increase the contribution of q_v advection to the PBL moisture increasing over the harvested WWB.

The results presented within this chapter help clarify the processes at work that enable the observed increases in water vapor during summertime AETs. Using the ARM network of AERI and DLID instruments, cross-WWB flow towards the harvested wheat was found. In addition, a 1-km deep moisture gradient was also found to be present along the eastern edge of the WWB. Additional analysis revealed that this cross-WWB flow enables moisture advection over the lowest 1 km during the AET. When combined with LASSO simulations, it becomes clear that the 500 to 1000-m increases of water vapor depicted by the ARM observations are a consequence of water vapor advection. These simulations also indicate that the turbulent moisture flux convergence terms only contribute to the moistening of the lowest 100-meters. Prior to the start of the AET, this term decays with time and reduces the amount of drying within the PBL driven by mixing. From a closer look at the evolution of the PBL presented by the LASSO runs, it appears that the decaying turbulence in the hours prior to sunset enables water vapor advection to rapidly moisten the lowest 1-km at the ARM site.

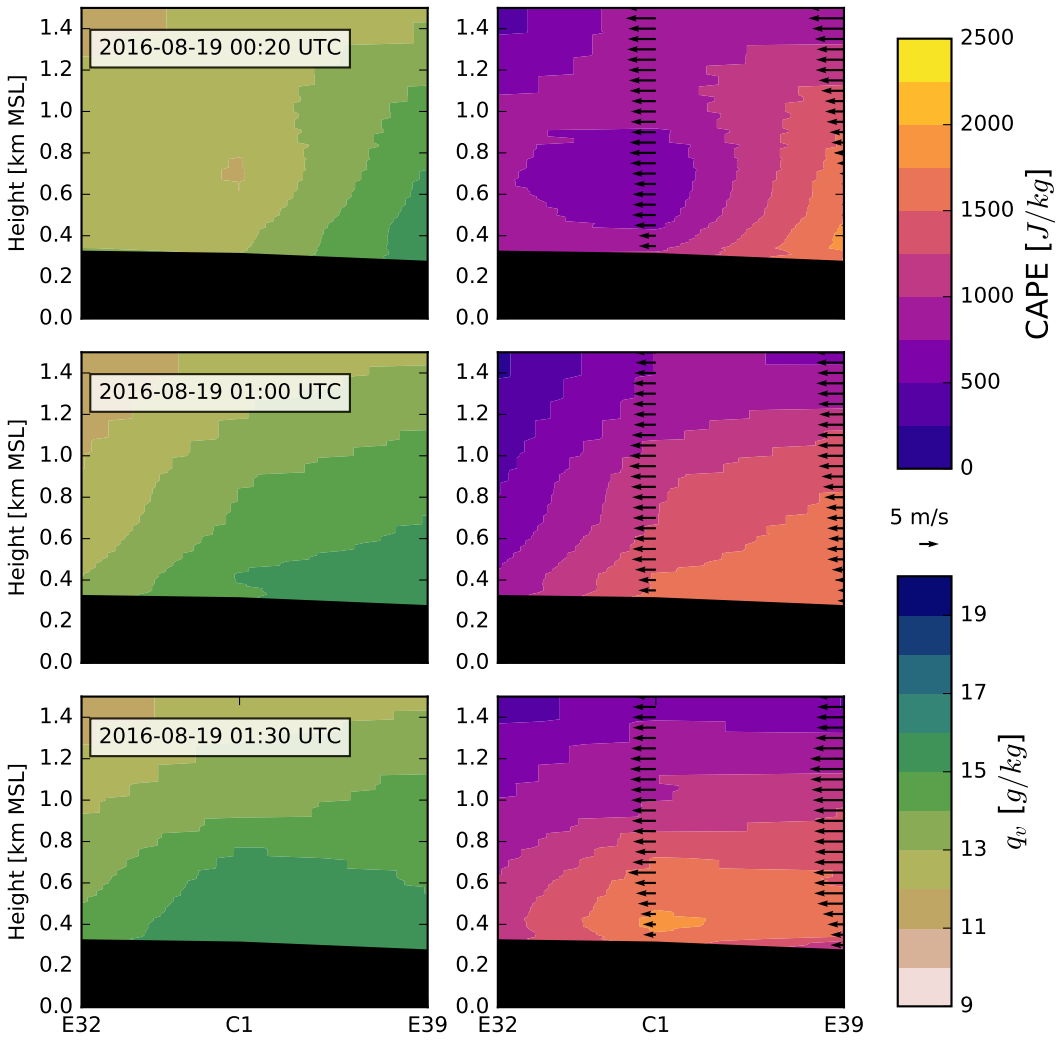

Figure 8.12: The evolution of the horizontal cross section from the ARM E32-C1-E39 sites for the 8-18-2016 case during the surge in moisture across the WWB. The left column indicates the q_v profile, while the right indicates the CAPE profile. Arrows in the CAPE plot indicates the cross-WWB wind vector at the C1 and E39 sites. From top to bottom the time of the cross sections moves from 00:20 to 1:00 to 1:30 UTC. Black indicates the ground.

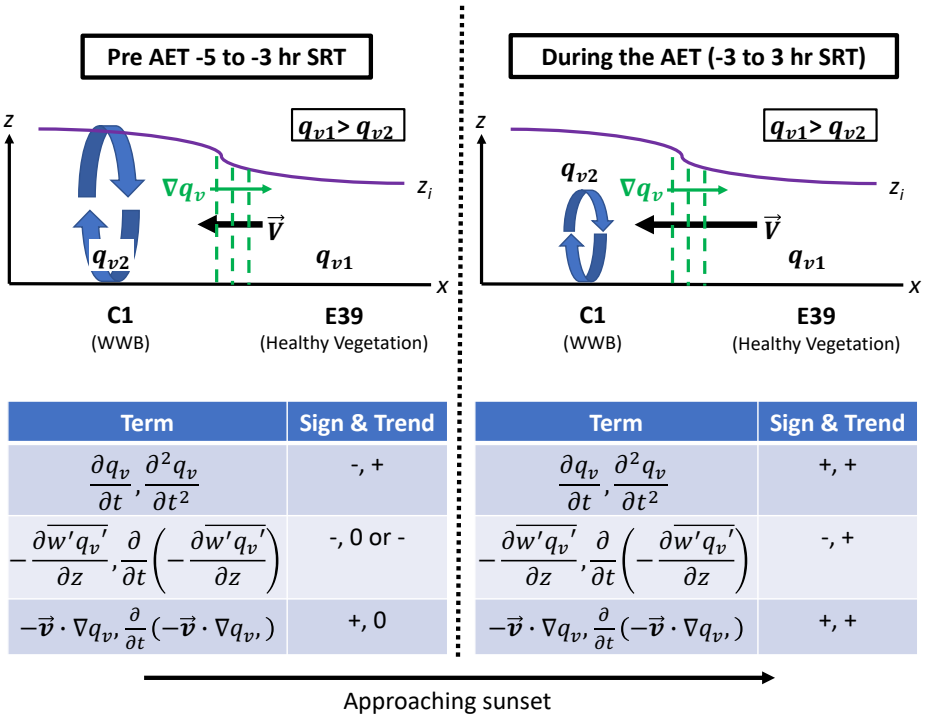

Term	Sign & Trend
$\frac{\partial q_v}{\partial t}, \frac{\partial^2 q_v}{\partial t^2}$	-, +
$-\frac{\partial \overline{w'q_v'}}{\partial z}, \frac{\partial}{\partial t}\left(-\frac{\partial \overline{w'q_v'}}{\partial z}\right)$	-, 0 or -
$-\vec{v}\cdot\nabla q_v, \frac{\partial}{\partial t}(-\vec{v}\cdot\nabla q_v,)$	+, 0

Term	Sign & Trend
$\frac{\partial q_v}{\partial t}, \frac{\partial^2 q_v}{\partial t^2}$	+, +
$-\frac{\partial \overline{w'q_v'}}{\partial z}, \frac{\partial}{\partial t}\left(-\frac{\partial \overline{w'q_v'}}{\partial z}\right)$	-, +
$-\vec{v}\cdot\nabla q_v, \frac{\partial}{\partial t}(-\vec{v}\cdot\nabla q_v,)$	+, +

Approaching sunset

Figure 8.13: An illustration showing the cross section along the WWB between the ARM sites C1 and E39 and how turbulence, winds, and moisture change before (left) and during the AET (right). The bottom table shows the sign of the relevant terms of the moisture tendency equation and their second derivatives in both stages. The blue circulation over the WWB represents the mixing ongoing throughout the day (left) and reduced mixing later on (right). The length of the black arrow indicates the wind speed along the WWB cross section, which accelerates per Figure 8.5. z_i indicates the CBL top which varies across the WWB per McPherson and Stensrud (2005).

Chapter 9

Conclusions and Future Work

This dissertation began with a discussion of the four ingredients relevant to deep, moist convection: instability, shear, lift, and moisture. From a survey of past literature discussing the evolution of the PBL during the AET (e.g., Wingo and Knupp 2015; Busse and Knupp 2012; Blackadar 1979; Mead and Thompson 2011), it is clear that as the sun sets, the spatiotemporal distribution of these ingredients is significantly modified as the PBL transitions from the CBL to a stable boundary layer (SBL). To skillfully forecast precipitation systems and meteorological hazards in the evening and at night, and in particular the evolution of deep, moist convection, a solid scientific understanding of how the AET modifies these ingredients is important.

When current literature is reviewed, several open questions appear regarding how moisture evolves during the AET in the SGP. Although several papers have documented rapid rises in near-surface q_v occurring during the AET, many of these studies have focused on geographical regions outside the SGP (e.g., northern Alabama, Busse and Knupp 2012, New York state Fitzjarrald and Lala 1989). To date, only one study has documented these q_v increases in the vertical during the SGP AET (Bonin et al. 2013) and the number of AET cases discussed in their study do not reach the levels needed to generalize its conclusions to other instances in the SGP. However, many studies attribute these increases in q_v to the stratification of turbulence (turbulent moisture flux

convergence becomes large) that occurs with the loss of insolation during the AET. Considering the increased risk of harm to society by deep, moist convection in the evening and nighttime hours (e.g., Kis and Straka 2010; Mead and Thompson 2011; Anderson-Frey et al. 2016) in the Southern Great Plains, it is clear that improving our understanding of how moisture evolves during the AET can be beneficial to a wide variety of scientific and non-scientific communities.

In an attempt to improve this understanding, this dissertation addressed the following questions by testing three hypotheses:

1. What is the spatiotemporal evolution of water vapor (q_v) in the Southern Great Plains during the AET?

   H1: AET increases in q_v can be found where vegetation is present.

2. How do these jumps in moisture change the parcel conditional instability?

   H2: Jumps in q_v may act to increase the conditional instability of parcels within the changing PBL.

3. What processes facilitate these jumps in q_v?

   H3: Jumps in q_v are caused by advection of q_v rather than the turbulent moisture flux convergence term.

During the course of this study, hypotheses **H2** and **H3** were accepted. However, tests of **H1** required additional modifications to this hypothesis. In some of the tests of **H1**, increases in water vapor similar to those found in past literature (e.g., Acevedo and Fitzjarrald 2001) were found to occur over vegetation and do manifest themselves as a maximum in q_v in the hours prior to sunset. This was primarily tested using Oklahoma Mesonet data and the 2D-VAR program (Spencer and Gao 2004). Monthly analyses primarily showed

that q_v increases prior to sunset are often focused along the SGP WWB, and had a strong seasonal cycle. Such increases were also found to occur east of the WWB, coinciding with the growth of vegetation between April and May. However, **H1** was not completely supported as the data collected showed that surface q_v increases occur along the WWB both before and after the harvest of winter wheat. In fact, increases along the WWB after the harvest both are significantly larger (1-4 g/kg) and occur over a depth of 1 km (Chapter 7). The presence of strong and deep increases in q_v over the AET, despite no vegetation present, suggests that further investigation was needed to understand these results (Chapter 8). The experiments attempting to answer this first question indicate that the changes to q_v during the AET displays a dependence upon vegetation, environmental characteristics, and can impact the atmosphere far above the surface layer.

During tests of **H2**, a maximum in conditional instability was found occurring around sunset in both ARM and Oklahoma Mesonet observations. With the Oklahoma Mesonet observations, a maximum in conditional instability was found 1.5 hours prior to sunset at sites where vegetation was present. This maximum was attributed to increases in moisture as a significant majority of the Oklahoma Mesonet stations analyzed indicated temperature was falling throughout the AET and therefore cannot account for increases in conditional instability. When analyzing the ARM profile data, the analysis of the 31 cases indicates that over the harvested-WWB, this maximum in instability generally extends to parcels throughout the lowest 1 km for several hours. In one case, the increases in instability were rapid and dramatic, as the CAPE increased from 2000 J/kg to nearly 5000 J/kg in 3 hours. In many of the tests performed, it was found

that increases in q_v play a significant role in modifying conditional instability during the AET, therefore leading to an acceptance of **H2**.

In Chapter 8, the final question was addressed and **H3** was tested. In these tests, a combination of LES runs at the ARM SGP site and observations obtained from a network of AERI and DLIDs deployed near the eastern edge of the WWB were used. This combined observation and modeling strategy was used to quantify the contributions of advection and turbulent moisture flux convergence to the evolution of moisture after the wheat was harvested. Initially, moisture advection across the eastern boundary of the WWB was estimated from observations to be between 0.6 g/kg/hr to 3 g/kg/hr during the AET. Additional observations indicate that this advection was facilitated by a moisture gradient that develops during the daytime across the eastern edge of the WWB. A subsequent evaluation of the various large-scale forcings specified in the LES runs suggested that the forcing datasets replicate the observed changes in the sign of water vapor advection but underestimated the observed magnitude of advection after sunset. Regardless, analysis of the LASSO model output revealed that even with this underestimation, the turbulent moisture flux convergence term neither provides the correct magnitude nor the correct depth to account for the deep changes in q_v occurring during the AET. Advection, however, as LES forcing and observational datasets demonstrated, does explain the increases in q_v over 1 km at the ARM site. This test using the LES, AERI, and DLID observations suggests that at least for the two cases that were considered, **H3** can be accepted.

The results from this work suggests that in the SGP, the redistribution of moisture and subsequent changes in conditional instability begins prior to sunset as turbulence decays throughout the AET. In fact, the balance between the

decay of turbulence and increasing advection accounts for the moisture changes observed over the WWB, even when the wheat is not actively growing. This reasoning explains why **H1** is only valid for some of the experiments performed. While this diurnal variation of the moisture across the SGP has been discussed in past literature (Parsons et al. 1991; Sun and Wu 1992) in the context of the dryline, this work extends this movement to other moisture gradients such as those related to vegetation differences in the SGP. While these papers discuss the regional variations of q_v via the dryline, this work contributes to the current knowledge by demonstrating the timing of the various atmospheric changes (e.g., decay of turbulence) that occur to modify moisture on the local scale.

9.1 Future Work

The results from this research indicate three possible directions in which future studies could go. Between Chapters 6 and 7, the direction of this research shifted to focus on the summer months. Instead, the analysis strategies used in Chapter 7 and Chapter 8 could be also shifted to focus on explaining and documenting the AET moisture changes over the WWB prior its harvest. Given the reduced advection in the 2D-VAR analyses, this change will likely require a more focused investigation on the turbulent moisture flux convergence term and its relationship to evapotranspiration near the surface. Doing so will require introducing a statement of causality to **H1**. This return to the near-surface should also include a discussion of the impact recent precipitation may have on q_v jumps, as even barren, wet soil may contribute to an increase in latent heat fluxes. Such a study was suggested back in Chapter 8 and could be performed by systematically varying the surface fluxes specified to the LASSO runs.

Next, future studies could explore if any of the results from this study can be generalized to other locations and scenarios. As this study was concentrated in Oklahoma, it is important to mention that these results are somewhat localized. Given the wide geographical area of the WWB across the Great Plains (Figure 9.1), other field projects could deploy similar ARM-like remote sensors (e.g., Wagner et al. 2018, in review) to other states where moisture gradients develop to test the ideas discussed in this study. While **H3** passed the tests developed in this study because the moisture gradients nearby were facilitated by land-surface contrasts, the land-surface is not the only mechanism that can develop such gradients in the atmosphere. Because of this reason, tests are needed to see if the changes between the turbulent moisture flux convergence term and advection in the decaying CBL are applicable to other horizontal gradients in the atmosphere (e.g., fronts, drylines). Such tests could reveal various local moisture sources, such as those found in Erlingis Lamers (2017). Considering this line of thought and the results of Wingo (2015) and Jones and Bannon (2002) suggesting low-level convergence increases during the AET near boundaries, it seems that the air near boundaries may regularly undergo a horizontal contraction during the AET. This process may enable a zone where the various ingredients (lift, moisture, and instability) become sufficient to develop deep, moist convection and additionally explain why the development of deep, moist convection tends to begin near sunset. Such tests should key in on the spatial variability of surface fluxes, as prior work discussed describes how coupled the surface is to PBL turbulence (e.g., Turner et al. (2018)).

Lastly, and relevant to the primary motivations of this work (6 o'clock magic), future work could address the question of the impact of these moisture jumps on pre-existing deep, moist convection. This study limited itself to

describing only the environmental changes of the moisture and the impact on conditional instability. While these environmental characteristics can be used to infer storm properties (Thompson et al. 2012a), the environmental changes shown in this research need to be observed and simulated in environments with storms already present to directly understand their impact on deep, moist convection. This line of inquiry may demonstrate that accurate modeling of the release of moisture from the edge of the WWB may be critical to achieve skillful forecasts of nighttime convection in the SGP. Future studies could include a field project focused on observing or model changes to the environment upstream of daytime convection during the AET. On the regional scale, hypothetical shifts in the status and location of the WWB could also be simulated using the WRF to help understand the impact the land-surface has on seasonal precipitation patterns in the SGP.

Finally, the results from this study and the next steps discussed offer an intriguing ethical and philosophical line of thought. It is clear from this and past research that the choices by humans to modify the land surface properties does create noticeable differences in the properties of the atmosphere. Should causality be found between modifications of the land-surface and short-term hazardous weather events, how does this change liability? For atmospheric scientists, perhaps forecasting an atmosphere where every gas regularly changes phase would be an easier problem to work through.

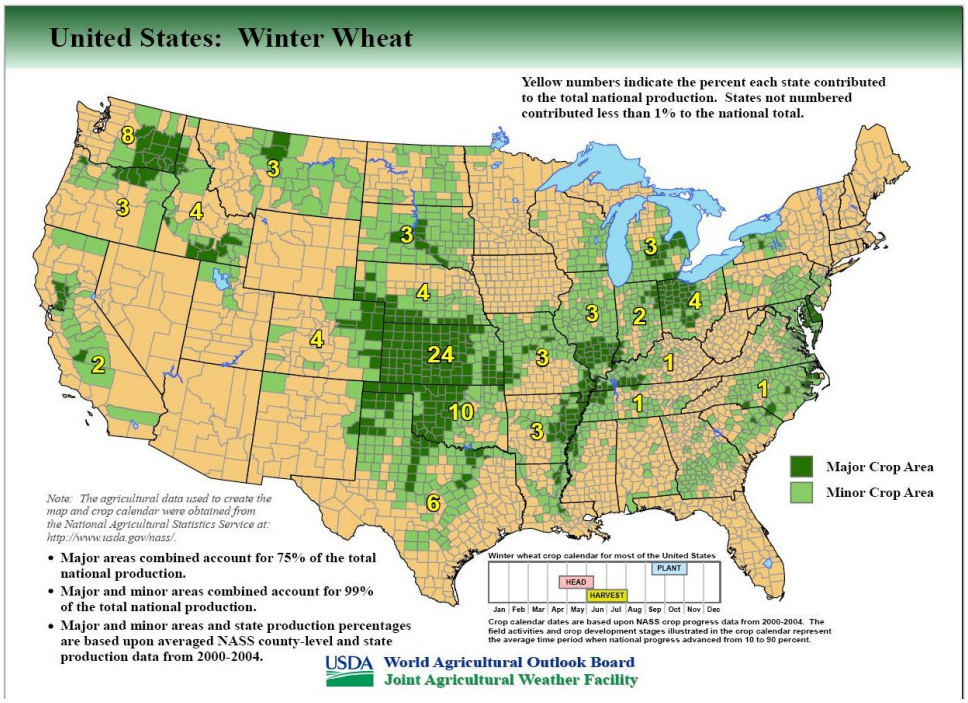

Figure 9.1: Geographical locations of where winter wheat is grown in the United States. Data used for this map is constructed using the National Agriculture Statistics Service, and the map was constructed by the U.S. Department of Agriculture. Image URL: https://www.usda.gov/media/blog/2013/03/7/usda-releases-new-maps-identifying-major-crop-producing-areas-united-states

Reference List

Acevedo, O. C. and D. R. Fitzjarrald, 2001: The Early Evening Surface-Layer Transition: Temporal and Spatial Variability. *Journal of the Atmospheric Sciences*, **58**, 2650–2667, doi:10.1175/1520-0469(2001)058¡2650:TEESLT¿2.0.CO;2.
URL http://journals.ametsoc.org/doi/abs/10.1175/1520-0469%282001%29058%3C2650%3ATEESLT%3E2.0.CO%3B2

Ahlgrimm, M. and R. Forbes, 2014: Improving the representation of low clouds and drizzle in the ecmwf model based on arm observations from the azores. *Monthly Weather Review*, **142**, 668–685.

Anderson-Frey, A. K., Y. P. Richardson, A. R. Dean, R. L. Thompson, and B. T. Smith, 2016: Investigation of Near-Storm Environments for Tornado Events and Warnings. *Weather and Forecasting*, **31**, 1771–1790, doi:10.1175/WAF-D-16-0046.1.
URL http://journals.ametsoc.org/doi/10.1175/WAF-D-16-0046.1

Anthes, R. A., 1984: Enhancement of convective precipitation by mesoscale variations in vegetative covering in semiarid regions. *Journal of Climate and Applied Meteorology*, **23**, 541–554.

Bagley, J. E., L. M. Kueppers, D. P. Billesbach, I. N. Williams, S. C. Biraud, and M. S. Torn, 2017: The influence of land cover on surface energy partitioning and evaporative fraction regimes in the U.S. Southern Great Plains. *Journal of Geophysical Research: Atmospheres*, **122**, 5793–5807, doi:10.1002/2017JD026740.
URL http://doi.wiley.com/10.1002/2017JD026740

Balling Jr, R. C., 1985: Warm season nocturnal precipitation in the great plains of the united states. *Journal of climate and applied meteorology*, **24**, 1383–1387.

Barnes, S. L., 1964: A Technique for Maximizing Details in Numerical Weather Map Analysis. *Journal of Applied Meteorology*, **3**, 396–409, doi:10.1175/1520-0450(1964)003¡0396:ATFMDI¿2.0.CO;2.
URL http://journals.ametsoc.org/doi/abs/10.1175/1520-0450%281964%29003%3C0396%3AATFMDI%3E2.0.CO%3B2

— 1994: Applications of the Barnes Objective Analysis Scheme. Part I: Effects of Undersampling, Wave Position, and Station Randomness. *Journal of Atmospheric and Oceanic Technology*, **11**, 1433–1448, doi:10.1175/1520-0426(1994)011¡1433:AOTBOA¿2.0.CO;2.

URL http://journals.ametsoc.org/doi/abs/10.1175/1520-0426%281994%29011%3C1433%3AAOTBOA%3E2.0.CO%3B2

Beare, R. J., J. M. Edwards, and A. J. Lapworth, 2006: Simulation of the observed evening transition and nocturnal boundary layers: Large-eddy simulation. *Quarterly Journal of the Royal Meteorological Society*, **132**, 81–99, doi:10.1256/qj.05.64.
URL http://doi.wiley.com/10.1256/qj.05.64

Benjamin, S. G., D. Dévényi, S. S. Weygandt, K. J. Brundage, J. M. Brown, G. a. Grell, D. Kim, B. E. Schwartz, T. G. Smirnova, T. L. Smith, and G. S. Manikin, 2004: An Hourly Assimilation–Forecast Cycle: The RUC. *Monthly Weather Review*, **132**, 495–518, doi:10.1175/1520-0493(2004)132¡0495:AHACTR¿2.0.CO;2.
URL http://journals.ametsoc.org/doi/abs/10.1175/1520-0493(2004)132%3C0495%3AAHACTR%3E2.0.CO%3B2

Benjamin, S. G., S. S. Weygandt, J. M. Brown, M. Hu, C. R. Alexander, T. G. Smirnova, J. B. Olson, E. P. James, D. C. Dowell, G. A. Grell, H. Lin, S. E. Peckham, T. L. Smith, W. R. Moninger, J. S. Kenyon, and G. S. Manikin, 2016: A North American Hourly Assimilation and Model Forecast Cycle: The Rapid Refresh. *Monthly Weather Review*, **144**, 1669–1694, doi:10.1175/MWR-D-15-0242.1.
URL http://journals.ametsoc.org/doi/10.1175/MWR-D-15-0242.1

Blackadar, A., 1979: High resolution models of the planetary boundary layer. *Advances in environmental science and engineering*.
URL https://scholar.google.com/scholar?q=blackadar+1979&btnG=&hl=en&as_sdt=0%2C37#0

Blackadar, A. K., 1957: Boundary Layer Wind Maxima and Their Significance for the Growth of Nocturnal Inversions. *Bulletin of the American Meteorological Society*, **38**, 283–290.
URL https://scholar.google.com/scholar?hl=en&q=blackadar+1957&btnG=&as_sdt=1%2C37&as_sdtp=#0

Blay-Carreras, E., E. R. Pardyjak, D. Pino, D. C. Alexander, F. Lohou, and M. Lothon, 2014: Countergradient heat flux observations during the evening transition period. *Atmospheric Chemistry and Physics*, **14**, 9077–9085, doi:10.5194/acp-14-9077-2014.
URL http://www.atmos-chem-phys.net/14/9077/2014/

Bluestein, H. B., 1992: *Synoptic-dynamic Meteorology in Midlatitudes: Observations and theory of weather systems*, volume 2. Taylor & Francis.

— 2015: *Severe Convective Storms and Tornadoes: Observations and Dynamics*. Springer Publishing Company, Incorporated, 1st edition.

Bluestein, H. B., G. S. Romine, R. Rotunno, D. W. Reif, and C. C. Weiss, 2017: On the anomalous counterclockwise turning of the surface wind with time in the plains of the united states. *Monthly Weather Review*.

Blumberg, W., K. Halbert, T. Supinie, P. Marsh, R. Thompson, and J. Hart, 2017a: Sharppy: An open-source sounding analysis toolkit for the atmospheric sciences. *Bulletin of the American Meteorological Society*, **98**, doi:10.1175/BAMS-D-15-00309.1.

Blumberg, W., D. Turner, U. Löhnert, and S. Castleberry, 2015: Ground-based temperature and humidity profiling using spectral infrared and microwave observations. Part II: Actual retrieval performance in clear-sky and cloudy conditions. *Journal of Applied Meteorology and Climatology*, **54**, doi:10.1175/JAMC-D-15-0005.1.

Blumberg, W. G., 2013: Developing a statistical thermodynamic retrieval for ground-based infrared spectrometers.

Blumberg, W. G., T. J. Wagner, D. D. Turner, and J. J. Correia, 2017b: Quantifying the Accuracy and Uncertainty of Diurnal Thermodynamic Profiles and Convection Indices Derived from the Atmospheric Emitted Radiance Interferometer. *Journal of Applied Meteorology and Climatology*, **56**, 2747–2766, doi:10.1175/JAMC-D-17-0036.1.
URL http://journals.ametsoc.org/doi/10.1175/JAMC-D-17-0036.1

Bolton, D., 1980: The Computation of Equivalent Potential Temperature. *Monthly Weather Review*, **108**, 1046–1053, doi:10.1175/1520-0493(1980)108¡1046:TCOEPT¿2.0.CO;2.
URL http://journals.ametsoc.org/doi/abs/10.1175/1520-0493%281980%29108%3C1046%3ATCOEPT%3E2.0.CO%3B2

Bonin, T., W. Blumberg, P. Klein, and P. Chilson, 2015: Thermodynamic and Turbulence Characteristics of the Southern Great Plains Nocturnal Boundary Layer Under Differing Turbulent Regimes. *Boundary-Layer Meteorology*, **157**, doi:10.1007/s10546-015-0072-2.

Bonin, T., P. Chilson, B. Zielke, and E. Fedorovich, 2013: Observations of the Early Evening Boundary-Layer Transition Using a Small Unmanned Aerial System. *Boundary-Layer Meteorology*, **146**, 119–132, doi:10.1007/s10546-012-9760-3.
URL http://link.springer.com/10.1007/s10546-012-9760-3

Bonner, W. D., 1968: Climatology of the Low Level Jet. *Monthly Weather Review*, **96**, 833–850, doi:10.1175/1520-0493(1968)096¡0833:COTLLJ¿2.0.CO;2.
URL http://journals.ametsoc.org/doi/abs/10.1175/1520-0493(1968)096%3C0833:COTLLJ%3E2.0.CO;2

Bosart, L. F. and H. B. Bluestein, 2008: *Synoptic-dynamic meteorology and weather analysis and forecasting : a tribute to Fred Sanders*. American Meteorological Society, 423 pp.
URL https://bookstore.ametsoc.org/catalog/book/synopticdynamic-meteorology-and-weather-analysis-and-forecasting

Brock, F. V., K. C. Crawford, R. L. Elliott, G. W. Cuperus, S. J. Stadler, H. L. Johnson, and M. D. Eilts, 1995: The Oklahoma Mesonet: A Technical Overview. *Journal of Atmospheric and Oceanic Technology*, **12**, 5–19, doi:10.1175/1520-0426(1995)012¡0005:TOMATO¿2.0.CO;2.
URL http://journals.ametsoc.org/doi/abs/10.1175/1520-0426(1995)012%3C0005:TOMATO%3E2.0.CO%3B2

Brooks, H., 2013: Severe thunderstorms and climate change. *Atmospheric Research*, **123**, 129 – 138, doi:https://doi.org/10.1016/j.atmosres.2012.04.002, 6th European Conference on Severe Storms 2011. Palma de Mallorca, Spain.
URL http://www.sciencedirect.com/science/article/pii/S0169809512000968

Brooks, H. E., 2007: Ingredients-Based Forecasting. *Atmospheric Convection: Research and Operational Forecasting Aspects*, Springer Vienna, Vienna, 133–140.
URL http://link.springer.com/10.1007/978-3-211-69291-2_12

Bunkers, M. J., M. R. Hjelmfelt, and P. L. Smith, 2006a: An observational examination of long-lived supercells. part i: Characteristics, evolution, and demise. *Weather and forecasting*, **21**, 673–688.

Bunkers, M. J., J. S. Johnson, L. J. Czepyha, J. M. Grzywacz, B. A. Klimowski, and M. R. Hjelmfelt, 2006b: An observational examination of long-lived supercells. part ii: Environmental conditions and forecasting. *Weather and forecasting*, **21**, 689–714.

Busse, J. and K. Knupp, 2012: Observed Characteristics of the Afternoon–Evening Boundary Layer Transition Based on Sodar and Surface Data. *Journal of Applied Meteorology and Climatology*, **51**, 571–582, doi:10.1175/2011JAMC2607.1.
URL http://journals.ametsoc.org/doi/abs/10.1175/2011JAMC2607.1

Cadeddu, M., J. Liljegren, and D. Turner, 2013: The atmospheric radiation measurement (arm) program network of microwave radiometers: Instrumentation, data, and retrievals. *Atmospheric Measurement Techniques*, **6**, 2359.

Carleton, A. M., D. J. Travis, J. O. Adegoke, D. L. Arnold, and S. Curran, 2008: Synoptic circulation and land surface influences on convection in the midwest us "corn belt" during the summers of 1999 and 2000. part ii: Role of vegetation boundaries. *Journal of Climate*, **21**, 3617–3641.

Chan, P. and K. Hon, 2011: Application of ground-based, multi-channel microwave radiometer in the nowcasting of intense convective weather through instability indices of the atmosphere. *Meteorologische Zeitschrift*, **20**, 431–440, doi:10.1127/0941-2948/2011/0276.
URL http://www.schweizerbart.de/papers/metz/detail/20/76280/Application_of_ground_based_multi_channel_microwav?af=crossref

Cimini, D., M. Nelson, J. Güldner, and R. Ware, 2015: Forecast indices from a ground-based microwave radiometer for operational meteorology. *Atmospheric Measurement Techniques*, **8**, 315–333, doi:10.5194/amt-8-315-2015.
URL http://www.atmos-meas-tech.net/8/315/2015/

Clough, S. and P. Brown, 1994: Residual analysis of surface spectral radiances between instrument observations and line-by-line calculations. ... *Radiation* ....
URL https://education.arm.gov/publications/proceedings/conf04/extended_abs/clough_sa.pdf

Clough, S., M. Shephard, E. Mlawer, J. Delamere, M. Iacono, K. Cady-Pereira, S. Boukabara, and P. Brown, 2005: Atmospheric radiative transfer modeling: a summary of the aer codes. *Journal of Quantitative Spectroscopy and Radiative Transfer*, **91**, 233–244.

Clough, S. A., M. J. Iacono, and J.-l. Moncet, 1992: Line-by-line calculations of atmospheric fluxes and cooling rates: Application to water vapor. *Journal of Geophysical Research*, **97**, 15761, doi:10.1029/92JD01419.
URL https://scholar.google.com/scholar?q=clough+et+al+1992+cooling+rate&btnG=&hl=en&as_sdt=0%2C37#0

Coffer, B. E. and M. D. Parker, 2015: Impacts of increasing low-level shear on supercells during the evening transition. *Monthly Weather Review*, 1–9, doi:10.1175/MWR-D-14-00328.1.
URL http://journals.ametsoc.org/doi/abs/10.1175/MWR-D-14-00328.1

Cook, D., 2016a: Eddy correlation flux measurement system handbook. Technical report, DOE ARM Climate Research Facility, Washington, DC (United States).

— 2016b: Energy balance bowen ratio (ebbr) handbook. Technical report, DOE ARM Climate Research Facility, Washington, DC (United States).

Darbieu, C., F. Lohou, M. Lothon, J. Vilà-Guerau de Arellano, F. Couvreux, P. Durand, D. Pino, E. G. Patton, E. Nilsson, E. Blay-Carreras, and B. Gioli, 2015: Turbulence vertical structure of the boundary layer during the afternoon transition. *Atmospheric Chemistry and Physics*, **15**, 10071–10086, doi:10.5194/acp-15-10071-2015.
URL http://www.atmos-chem-phys.net/15/10071/2015/

Davies-Jones, R., 2008: An Efficient and Accurate Method for Computing the Wet-Bulb Temperature along Pseudoadiabats. *Monthly Weather Review*, **136**, 2764–2785, doi:10.1175/2007MWR2224.1.
URL http://journals.ametsoc.org/doi/abs/10.1175/2007MWR2224.1

Deardorff, J. W., 1980: Stratocumulus-capped mixed layers derived from a three-dimensional model. *Boundary-Layer Meteorology*, **18**, 495–527.

Delamere, J. S., S. A. Clough, V. H. Payne, E. J. Mlawer, D. D. Turner, and R. R. Gamache, 2010: A far-infrared radiative closure study in the Arctic: Application to water vapor. *Journal of Geophysical Research*, **115**, D17106, doi:10.1029/2009JD012968.
URL http://doi.wiley.com/10.1029/2009JD012968

Diffenbaugh, N. S., M. Scherer, and R. J. Trapp, 2013: Robust increases in severe thunderstorm environments in response to greenhouse forcing. *Proceedings of the National Academy of Sciences*, **110**, 16361–16366, doi:10.1073/pnas.1307758110.
URL http://www.pnas.org/content/110/41/16361.abstract

Doswell, C. a., 1987: The Distinction between Large-Scale and Mesoscale Contribution to Severe Convection: A Case Study Example.

Doswell, C. A., H. E. Brooks, and R. A. Maddox, 1996: Flash Flood Forecasting: An Ingredients-Based Methodology. *Weather and Forecasting*, **11**, 560–581, doi:10.1175/1520-0434(1996)011¡0560:FFFAIB¿2.0.CO;2.
URL http://journals.ametsoc.org/doi/abs/10.1175/1520-0434%281996%29011%3C0560%3AFFFAIB%3E2.0.CO%3B2

Doswell, C. A. and E. N. Rasmussen, 1994: The Effect of Neglecting the Virtual Temperature Correction on CAPE Calculations. *Weather and Forecasting*, **9**, 625–629, doi:10.1175/1520-0434(1994)009¡0625:TEONTV¿2.0.CO;2.

URL http://journals.ametsoc.org/doi/abs/10.1175/1520-0434%281994%29009%3C0625%3ATEONTV%3E2.0.CO%3B2

Doswell III, C. A. and P. M. Markowski, 2004: Is buoyancy a relative quantity? *Monthly weather review*, **132**, 853–863.

Edwards, J. M., R. J. Beare, and A. J. Lapworth, 2006: Simulation of the observed evening transition and nocturnal boundary layers: Single-column modelling. *Quarterly Journal of the Royal Meteorological Society*, **132**, 61–80, doi:10.1256/qj.05.63.
URL http://doi.wiley.com/10.1256/qj.05.63

Edwards, R., A. R. Dean, R. L. Thompson, and B. T. Smith, 2012: Convective Modes for Significant Severe Thunderstorms in the Contiguous United States. Part III: Tropical Cyclone Tornadoes. *Weather and Forecasting*, 120807113027001, doi:10.1175/WAF-D-11-00117.1.
URL http://journals.ametsoc.org/doi/abs/10.1175/WAF-D-11-00115.1

Edwards, R. and L. R. Lemon, 2002: 7.1 proactive or reactive: The severe storm threat to large event venues.

Endo, S., A. M. Fridlind, W. Lin, A. M. Vogelmann, T. Toto, A. S. Ackerman, G. M. McFarquhar, R. C. Jackson, H. H. Jonsson, and Y. Liu, 2015: Racoro continental boundary layer cloud investigations: 2. large-eddy simulations of cumulus clouds and evaluation with in situ and ground-based observations. *Journal of Geophysical Research: Atmospheres*, **120**, 5993–6014.

Erlingis Lamers, J., 2017: Moisture sources for flash floods in the united states.

Esterheld, J. M. and D. J. Giuliano, 2008: Discriminating between Tornadic and Non-Tornadic Supercells: A New Hodograph Technique. *E-Journal of Severe Storms Meteorology*, **3**, 1–50.
URL http://www.ejssm.org/ojs/index.php/ejssm/article/view/33/37

Feltz, W. F. and J. R. Mecikalski, 2002: Monitoring High-Temporal-Resolution Convective Stability Indices Using the Ground-Based Atmospheric Emitted Radiance Interferometer (AERI) during the 3 May 1999 Oklahoma–Kansas Tornado Outbreak. *Weather and Forecasting*, **17**, 445–455, doi:10.1175/1520-0434(2002)017¡0445:MHTRCS¿2.0.CO;2.
URL http://journals.ametsoc.org/doi/abs/10.1175/1520-0434(2002)017%3C0445:MHTRCS%3E2.0.CO%3B2

Feltz, W. F., W. L. Smith, H. B. Howell, R. O. Knuteson, H. Woolf, and H. E. Revercomb, 2003: Near-Continuous Profiling of Temperature, Moisture, and

Atmospheric Stability Using the Atmospheric Emitted Radiance Interferometer (AERI). *Journal of Applied Meteorology*, **42**, 584–597, doi:10.1175/1520-0450(2003)042¡0584:NPOTMA¿2.0.CO;2.
URL http://journals.ametsoc.org/doi/abs/10.1175/1520-0450(2003)042%3C0584:NPOTMA%3E2.0.CO%3B2

Feltz, W. F., W. L. Smith, R. O. Knuteson, H. E. Revercomb, H. M. Woolf, and H. B. Howell, 1998: Meteorological Applications of Temperature and Water Vapor Retrievals from the Ground-Based Atmospheric Emitted Radiance Interferometer (AERI). *Journal of Applied Meteorology*, **37**, 857–875, doi:10.1175/1520-0450(1998)037¡0857:MAOTAW¿2.0.CO;2.

Feng, S., Z. Li, Y. Liu, W. Lin, M. Zhang, T. Toto, A. M. Vogelmann, and S. Endo, 2015: Development of fine-resolution analyses and expanded large-scale forcing properties: 2. scale awareness and application to single-column model experiments. *Journal of Geophysical Research: Atmospheres*, **120**, 667–677.

Ferziger, J. H., J. R. Koseff, and S. G. Monismith, 2002: Numerical simulation of geophysical turbulence. *Computers & fluids*, **31**, 557–568.

Fitzjarrald, D. R. and G. G. Lala, 1989: Hudson Valley Fog Environments. *Journal of Applied Meteorology*, **28**, 1303–1328, doi:10.1175/1520-0450(1989)028¡1303:HVFE¿2.0.CO;2.
URL http://journals.ametsoc.org/doi/abs/10.1175/1520-0450%281989%29028%3C1303%3AHVFE%3E2.0.CO%3B2

Flower, W. D., 1937: *An investigation into the variation of the lapse rate of temperature in the atmosphere near the ground at Ismailia, Egypt*. Meteorological Office.

Fritschen, L., P. Qian, E. Kanemasu, D. Nie, E. Smith, J. Stewart, S. Verma, and M. Wesely, 1992: Comparisons of surface flux measurement systems used in fife 1989. *Journal of Geophysical Research: Atmospheres*, **97**, 18697–18713.

Gao, J., M. Xue, K. Brewster, and K. K. Droegemeier, 2004: A Three-Dimensional Variational Data Analysis Method with Recursive Filter for Doppler Radars. *Journal of Atmospheric and Oceanic Technology*, **21**, 457–469, doi:10.1175/1520-0426(2004)021¡0457:ATVDAM¿2.0.CO;2.
URL http://journals.ametsoc.org/doi/abs/10.1175/1520-0426%282004%29021%3C0457%3AATVDAM%3E2.0.CO%3B2

Garcia-Carreras, L., D. J. Parker, and J. H. Marsham, 2011: What is the mechanism for the modification of convective cloud distributions by land surface–induced flows? *Journal of the Atmospheric Sciences*, **68**, 619–634.

Gavilán, P. and J. Berengena, 2007: Accuracy of the bowen ratio-energy balance method for measuring latent heat flux in a semiarid advective environment. *Irrigation Science*, **25**, 127–140.

Grant, A. L. M., 1997: An observational study of the evening transition boundary-layer. *Quarterly Journal of the Royal Meteorological Society*, **123**, 657–677, doi:10.1002/qj.49712353907.
URL `http://doi.wiley.com/10.1002/qj.49712353907`

Gratz, J. and E. Noble, 2006: Lightning safety and large stadiums. *Bulletin of the American Meteorological Society*, **87**, 1187–1194.

Gustafson, W. I., A. M. Vogelmann, X. Cheng, S. Endo, B. Krishna, Z. Li, T. Toto, and H. Xiao, 2017: Description of the lasso alpha 1 release. Technical report, DOE Office of Science Atmospheric Radiation Measurement (ARM) Program (United States).

Gustafson Jr, W. and A. Vogelmann, 2015: Les arm symbiotic simulation and observation (lasso) implementation strategy. Technical report, DOE Office of Science Atmospheric Radiation Measurement (ARM) Program (United States); Pacific Northwest National Laboratory (PNNL), Richland, WA (United States).

Halbert, K., W. Blumberg, and P. Marsh, 2015: Sharppy: Fueling the python cult. *Fifth Symp. on Advances in Modeling and Analysis Using Python*.

Han, Y. and E. Westwater, 2000: Analysis and improvement of tipping calibration for ground-based microwave radiometers. *Geoscience and Remote Sensing, ...*.
URL `http://ieeexplore.ieee.org/xpls/abs_all.jsp?arnumber=843018`

Hart, J. and W. Korotky, 1991: The sharp workstation v1. 50 users guide. *NOAA/National Weather Service*.

Haugland, M. J. and K. C. Crawford, 2005: The Diurnal Cycle of Land–Atmosphere Interactions across Oklahoma's Winter Wheat Belt. *Monthly Weather Review*, **133**, 120–130, doi:10.1175/MWR-2842.1.
URL `http://journals.ametsoc.org/doi/abs/10.1175/MWR-2842.1`

Hewison, T. J., 2007: 1D-VAR Retrieval of Temperature and Humidity Profiles From a Ground-Based Microwave Radiometer. *IEEE Transactions on Geoscience and Remote Sensing*, **45**, 2163–2168, doi:10.1109/TGRS.2007.898091.
URL `http://ieeexplore.ieee.org/document/4261055/`

Hocker, J. E. and J. B. Basara, 2008: A 10-year spatial climatology of squall line storms across Oklahoma. *International Journal of Climatology*, **28**, 765–775, doi:10.1002/joc.1579.

Holdridge, D., J. Prell, M. Ritsche, and R. Coulter, 2011: Balloon-borne sounding system handbook. *Atmospheric Radiation Measurement Climate Research Facility, Dept. of Energy, ARM TR-029*, **27**.

Holton, J. R., 1967: The diurnal boundary layer wind oscillation above sloping terrain. *Tellus*, **19**, 200–205, doi:10.3402/tellusa.v19i2.9766.
URL https://www.tandfonline.com/doi/full/10.3402/tellusa.v19i2.9766

Iacono, M. J., J. S. Delamere, E. J. Mlawer, M. W. Shephard, S. A. Clough, and W. D. Collins, 2008: Radiative forcing by long-lived greenhouse gases: Calculations with the aer radiative transfer models. *Journal of Geophysical Research: Atmospheres*, **113**.

Illston, B. G., J. B. Basara, C. A. Fiebrich, K. C. Crawford, E. Hunt, D. K. Fisher, R. Elliott, and K. Humes, 2008: Mesoscale monitoring of soil moisture across a statewide network. *Journal of Atmospheric and Oceanic Technology*, **25**, 167–182.

Jensen, D. D., D. F. Nadeau, S. W. Hoch, and E. R. Pardyjak, 2016: Observations of near-surface heat-flux and temperature profiles through the early evening transition over contrasting surfaces. *Boundary-Layer Meteorology*, **159**, 567–587.

Jones, E., T. Oliphant, P. Peterson, et al., 2001: SciPy: Open source scientific tools for Python. [Online; accessed ¡today¿].
URL http://www.scipy.org/

Jones, P. A. and P. R. Bannon, 2002: A mixed-layer model of the diurnal dryline. *Journal of the Atmospheric Sciences*, **59**, 2582–2593, doi:10.1175/1520-0469(2002)059¡2582:AMLMOT¿2.0.CO;2.
URL https://doi.org/10.1175/1520-0469(2002)059<2582:AMLMOT>2.0.CO;2

Kalnay, E., M. Kanamitsu, R. Kistler, W. Collins, D. Deaven, L. Gandin, M. Iredell, S. Saha, G. White, J. Woollen, Y. Zhu, A. Leetmaa, R. Reynolds, M. Chelliah, W. Ebisuzaki, W. Higgins, J. Janowiak, K. C. Mo, C. Ropelewski, J. Wang, R. Jenne, and D. Joseph, 1996: The NCEP/NCAR 40-Year Reanalysis Project. *Bulletin of the American Meteorological Society*, **77**, 437–471, doi:10.1175/1520-0477(1996)077¡0437:TNYRP¿2.0.CO;2.
URL http://journals.ametsoc.org/doi/abs/10.1175/1520-0477%281996%29077%3C0437%3ATNYRP%3E2.0.CO%3B2

Khairoutdinov, M. F. and D. A. Randall, 2003: Cloud resolving modeling of the arm summer 1997 iop: Model formulation, results, uncertainties, and sensitivities. *Journal of the Atmospheric Sciences*, **60**, 607–625.

Kis, A. K. and J. M. Straka, 2010: Nocturnal Tornado Climatology*. *Weather and Forecasting*, **25**, 545–561, doi:10.1175/2009WAF2222294.1.
URL http://journals.ametsoc.org/doi/abs/10.1175/2009WAF2222294.1

Knuteson, R. O., H. E. Revercomb, F. a. Best, N. C. Ciganovich, R. G. Dedecker, T. P. Dirkx, S. C. Ellington, W. F. Feltz, R. K. Garcia, H. B. Howell, W. L. Smith, J. F. Short, and D. C. Tobin, 2004: Atmospheric Emitted Radiance Interferometer. Part II: Instrument performance. *Journal of Atmospheric and Oceanic Technology*, **21**, 1777–1789, doi:10.1175/JTECH-1663.1.
URL http://journals.ametsoc.org/doi/abs/10.1175/JTECH-1663.1

Koch, S. E., M. Desjardins, and P. J. Kocin, 1983: An interactive Barnes objective map analysis scheme for use with satellite and conventional data. *Journal of Climate and Applied Meteorology*, **22**, 1487–1503, doi:10.1175/1520-0450(1983)022¡1487:AIBOMA¿2.0.CO;2.
URL http://journals.ametsoc.org/doi/abs/10.1175/1520-0450(1983)022%3C1487:AIBOMA%3E2.0.CO%3B2

Koch, S. E., R. Ware, H. Jiang, Y. Xie, S. E. Koch, R. Ware, H. Jiang, and Y. Xie, 2016: Rapid Mesoscale Environmental Changes Accompanying Genesis of an Unusual Tornado. *Weather and Forecasting*, **31**, 763–786, doi:10.1175/WAF-D-15-0105.1.
URL http://journals.ametsoc.org/doi/10.1175/WAF-D-15-0105.1

Küchler, N., D. Turner, U. Löhnert, and S. Crewell, 2016: Calibrating ground-based microwave radiometers: Uncertainty and drifts. *Radio Science*, **51**, 311–327.

Kyle, H. L., P. E. Ardanuy, and E. J. Hurley, 1985: The status of the nimbus-7 earth-radiation-budget data set. *Bulletin of the American Meteorological Society*, **66**, 1378–1388.

Kyrouac, J. and A. Theisen, 2017: Biases of the MET Temperature and Relative Humidity Sensor (HMP45) Report. Technical report, DOE Office of Science Atmospheric Radiation Measurement (ARM) Program (United States).
URL http://www.osti.gov/servlets/purl/1366737/

Lenschow, D. H., V. Wulfmeyer, and C. Senff, 2000: Measuring second- through fourth-order moments in noisy data. *Journal of Atmospheric and Oceanic Technology*, **17**, 1330–1347, doi:10.1175/1520-0426(2000)017¡1330:MSTFOM¿2.0.CO;2.
URL http://journals.ametsoc.org/doi/abs/10.1175/1520-0426(2000)017%3C1330:MSTFOM%3E2.0.CO;2

Lhermitte, R. M., 1961: Precipitation motion by pulse doppler radar. *Proc. 9th Weather Radar Conf., 1961*.

Li, Z., Y. Chao, J. D. Farrara, and J. C. McWilliams, 2013: Impacts of distinct observations during the 2009 prince william sound field experiment: A data assimilation study. *Continental Shelf Research*, **63**, S209–S222.

Li, Z., S. Feng, Y. Liu, W. Lin, M. Zhang, T. Toto, A. M. Vogelmann, and S. Endo, 2015: Development of fine-resolution analyses and expanded large-scale forcing properties: 1. methodology and evaluation. *Journal of Geophysical Research: Atmospheres*, **120**, 654–666.

Löhnert, U. and O. Maier, 2012: Operational profiling of temperature using ground-based microwave radiometry at Payerne: prospects and challenges. *Atmospheric Measurement Techniques*, **5**, 1121–1134, doi:10.5194/amt-5-1121-2012.
URL `http://www.atmos-meas-tech.net/5/1121/2012/`

Löhnert, U., D. D. Turner, and S. Crewell, 2009: Ground-Based Temperature and Humidity Profiling Using Spectral Infrared and Microwave Observations. Part : Simulated Retrieval Performance in Clear-Sky Conditions. *Journal of Applied Meteorology and Climatology*, **48**, 1017–1032, doi:10.1175/2008JAMC2060.1.
URL `http://journals.ametsoc.org/doi/abs/10.1175/2008JAMC2060.1`

Lothon, M., F. Lohou, D. Pino, F. Couvreux, E. R. Pardyjak, J. Reuder, J. Vilà-Guerau de Arellano, P. Durand, O. Hartogensis, D. Legain, P. Augustin, B. Gioli, D. H. Lenschow, I. Faloona, C. Yagüe, D. C. Alexander, W. M. Angevine, E. Bargain, J. Barrié, E. Bazile, Y. Bezombes, E. Blay-Carreras, A. van de Boer, J. L. Boichard, A. Bourdon, A. Butet, B. Campistron, O. de Coster, J. Cuxart, A. Dabas, C. Darbieu, K. Deboudt, H. Delbarre, S. Derrien, P. Flament, M. Fourmentin, A. Garai, F. Gibert, A. Graf, J. Groebner, F. Guichard, M. A. Jiménez, M. Jonassen, A. van den Kroonenberg, V. Magliulo, S. Martin, D. Martinez, L. Mastrorillo, A. F. Moene, F. Molinos, E. Moulin, H. P. Pietersen, B. Piguet, E. Pique, C. Román-Cascón, C. Rufin-Soler, F. Saïd, M. Sastre-Marugán, Y. Seity, G. J. Steeneveld, P. Toscano, O. Traullé, D. Tzanos, S. Wacker, N. Wildmann, and A. Zaldei, 2014: The BLLAST field experiment: Boundary-Layer Late Afternoon and Sunset Turbulence. *Atmospheric Chemistry and Physics*, **14**, 10931–10960, doi:10.5194/acp-14-10931-2014.
URL `http://www.atmos-chem-phys.net/14/10931/2014/`

Maddox, R. A., 1993: Diurnal low-level wind oscillation and storm-relative helicity. *The Tornado: Its Structure, Dynamics, Prediction, and Hazards*,

591–598.
URL http://doi.wiley.com/10.1029/GM079p0591

Mahrt, L., 2017: The near-surface evening transition. *Quarterly Journal of the Royal Meteorological Society*, doi:10.1002/qj.3153.
URL http://doi.wiley.com/10.1002/qj.3153

Mahrt, L., J. Sun, W. Blumen, T. Delany, and S. Oncley, 1998: Nocturnal Boundary Layer Regimes. *Boundary-Layer Meteorology*, **88**, 255–278.

Margules, M., 1906: Uber temperaturschichtung in stationar bewegter und ruhender luft. *Meteorologische Zeitschrift.*, **23**, 243–254.

Margules, M., E. Volken, A. M. Giesche, and S. Brönnimann, 2016: On temperature stratification in resting and non-accelerated moving air. *Meteorologische Zeitschrift*, **25**, 795–804.

Markowski, P. and Y. Richardson, 2011: *Mesoscale meteorology in midlatitudes*, volume 2. John Wiley & Sons.

Markowski, P. M. and Y. P. Richardson, 2014: The Influence of Environmental Low-Level Shear and Cold Pools on Tornadogenesis: Insights from Idealized Simulations. *Journal of the Atmospheric Sciences*, **71**, 243–275, doi:10.1175/JAS-D-13-0159.1.
URL http://journals.ametsoc.org/doi/abs/10.1175/JAS-D-13-0159.1

Markowski, P. M., Y. P. Richardson, P. M. Markowski, and Y. P. Richardson, 2014: The Influence of Environmental Low-Level Shear and Cold Pools on Tornadogenesis: Insights from Idealized Simulations. *Journal of the Atmospheric Sciences*, **71**, 243–275, doi:10.1175/JAS-D-13-0159.1.
URL http://journals.ametsoc.org/doi/abs/10.1175/JAS-D-13-0159.1

Markowski, P. M., J. M. Straka, and E. N. Rasmussen, 2002: Direct Surface Thermodynamic Observations within the Rear-Flank Downdrafts of Nontornadic and Tornadic Supercells. *Monthly Weather Review*, **130**, 1692–1721, doi:10.1175/1520-0493(2002)130¡1692:DSTOWT¿2.0.CO;2.
URL http://journals.ametsoc.org/doi/abs/10.1175/1520-0493(2002)130%3C1692%3ADSTOWT%3E2.0.CO%3B2

Maschwitz, G., U. Löhnert, S. Crewell, T. Rose, and D. D. Turner, 2013: Investigation of ground-based microwave radiometer calibration techniques at 530 hPa. *Atmospheric Measurement Techniques*, **6**, 2641–2658, doi:10.5194/amt-6-2641-2013.
URL http://www.atmos-meas-tech.net/6/2641/2013/

Masiello, G., C. Serio, and P. Antonelli, 2012: Inversion for atmospheric thermodynamical parameters of iasi data in the principal components space. *Quarterly Journal of the Royal Meteorological Society*, **138**, 103–117.

McPherson, R. A., 2007: A review of vegetation—atmosphere interactions and their influences on mesoscale phenomena. *Progress in Physical Geography*, **31**, 261–285.

McPherson, R. a., C. a. Fiebrich, K. C. Crawford, R. L. Elliott, J. R. Kilby, D. L. Grimsley, J. E. Martinez, J. B. Basara, B. G. Illston, D. a. Morris, K. a. Kloesel, S. J. Stadler, A. D. Melvin, A. J. Sutherland, H. Shrivastava, J. D. Carlson, J. M. Wolfinbarger, J. P. Bostic, and D. B. Demko, 2007: Statewide monitoring of the mesoscale environment: A technical update on the Oklahoma Mesonet. *Journal of Atmospheric and Oceanic Technology*, **24**, 301–321, doi:10.1175/JTECH1976.1.
URL http://journals.ametsoc.org/doi/abs/10.1175/JTECH1976.1

McPherson, R. A. and D. J. Stensrud, 2005: Influences of a Winter Wheat Belt on the Evolution of the Boundary Layer. *Monthly Weather Review*, **133**, 2178–2199, doi:10.1175/MWR2968.1.
URL http://journals.ametsoc.org/doi/abs/10.1175/MWR2968.1

McPherson, R. A., D. J. Stensrud, and K. C. Crawford, 2004: The Impact of Oklahoma's Winter Wheat Belt on the Mesoscale Environment. *Monthly Weather Review*, **132**, 405–421, doi:10.1175/1520-0493(2004)132¡0405:TIOOWW¿2.0.CO;2.
URL http://journals.ametsoc.org/doi/abs/10.1175/1520-0493%282004%29132%3C0405%3ATIOOWW%3E2.0.CO%3B2

Mead, C. M. and R. L. Thompson, 2011: Environmental characteristics associated with nocturnal significant-tornado events in the central and southern Great Plains. *Electronic Journal of Severe Storms Meteorology*, **6**, 1–35.

Means, L. L., 1944: *The nocturnal maximum occurrence of thunderstorms in the midwestern states*. Master's thesis, University of Chicago, Department of Physics.

Mellor, G. L. and T. Yamada, 1982: Development of a turbulence closure model for geophysical fluid problems. *Reviews of Geophysics*, **20**, 851, doi:10.1029/RG020i004p00851.
URL ftp://ftp.icess.ucsb.edu/pub/org/lakemix/matlibrary/users/dturney/2009_08_24_WritingPaperWithSally/related_papers/Mellor_Yamada_1982_MixedLayerTurbulenceClosure.pdf

Michael, P., 1994: Estimating advective tendencies from field measurements. *Monthly weather review*, **122**, 2202–2209.

Mlawer, E. J., V. H. Payne, J.-L. Moncet, J. S. Delamere, M. J. Alvarado, and D. C. Tobin, 2012: Development and recent evaluation of the MT_CKD model of continuum absorption. *Philosophical transactions. Series A, Mathematical, physical, and engineering sciences*, **370**, 2520–56, doi:10.1098/rsta.2011.0295. URL `http://www.ncbi.nlm.nih.gov/pubmed/22547231`

Mlawer, E. J., S. J. Taubman, P. D. Brown, M. J. Iacono, and S. A. Clough, 1997: Radiative transfer for inhomogeneous atmospheres: Rrtm, a validated correlated-k model for the longwave. *Journal of Geophysical Research: Atmospheres*, **102**, 16663–16682.

Moller, A. R., C. a. Doswell, M. P. Foster, and G. R. Woodall, 1994: The Operational Recognition of Supercell Thunderstorm Environments and Storm Structures.

Monin, A. and A. Obukhov, 1954: Basic laws of turbulent mixing in the surface layer of the atmosphere. *Contrib. Geophys. Inst. Acad. Sci. USSR*, **151**, e187.

Morris, V., 2005: Total sky imager (tsi) handbook. Technical report, Citeseer.

Morris, V. R., 2016: Ceilometer (ceil) instrument handbook. Technical report, DOE Office of Science Atmospheric Radiation Measurement (ARM) Program (United States).

Morrison, H., J. Curry, and V. Khvorostyanov, 2005: A new double-moment microphysics parameterization for application in cloud and climate models. part i: Description. *Journal of the Atmospheric Sciences*, **62**, 1665–1677.

Morrison, H., G. Thompson, and V. Tatarskii, 2009: Impact of cloud microphysics on the development of trailing stratiform precipitation in a simulated squall line: Comparison of one-and two-moment schemes. *Monthly Weather Review*, **137**, 991–1007.

Nasser, S. M. and T. B. Pulimood, 2009: Allergens and thunderstorm asthma. *Current allergy and asthma reports*, **9**, 384–390.

Newsom, R., 2012: Doppler lidar (dl) handbook. Technical report, DOE Office of Science Atmospheric Radiation Measurement (ARM) Program (United States).

Newsom, R. K., D. D. Turner, and J. E. M. Goldsmith, 2013: Long-term evaluation of temperature profiles measured by an operational raman lidar. *Journal of Atmospheric and Oceanic Technology*, doi:10.1175/JTECH-D-12-00138.1.

Nieuwstadt, F. T. M. and R. a. Brost, 1986: The Decay of Convective Turbulence.

Nilsson, E., F. Lohou, M. Lothon, E. Pardyjak, L. Mahrt, and C. Darbieu, 2016a: Turbulence kinetic energy budget during the afternoon transition – Part 1: Observed surface TKE budget and boundary layer description for 10 intensive observation period days. *Atmospheric Chemistry and Physics*, **16**, 8849–8872, doi:10.5194/acp-16-8849-2016.
URL http://www.atmos-chem-phys.net/16/8849/2016/

Nilsson, E., M. Lothon, F. Lohou, E. Pardyjak, O. Hartogensis, and C. Darbieu, 2016b: Turbulence kinetic energy budget during the afternoon transition – Part 2: A simple TKE model. *Atmospheric Chemistry and Physics*, **16**, 8873–8898, doi:10.5194/acp-16-8873-2016.
URL http://www.atmos-chem-phys.net/16/8873/2016/

Nowotarski, C. J., P. M. Markowski, and Y. P. Richardson, 2011: The Characteristics of Numerically Simulated Supercell Storms Situated over Statically Stable Boundary Layers. *Monthly Weather Review*, **139**, 3139–3162, doi:10.1175/MWR-D-10-05087.1.
URL https://etda.libraries.psu.edu/paper/10701/6380

Orville, R. E., 1981: Global distribution of midnight lighting—september to november 1977. *Monthly Weather Review*, **109**, 391–395.

Parker, M. D., 2014: Composite VORTEX2 Supercell Environments from Near-Storm Soundings. *Monthly Weather Review*, **142**, 508–529, doi:10.1175/MWR-D-13-00167.1.
URL http://journals.ametsoc.org/doi/abs/10.1175/MWR-D-13-00167.1

Parrish, D. F. and J. C. Derber, 1992: The national meteorological center's spectral statistical-interpolation analysis system. *Monthly Weather Review*, **120**, 1747–1763.

Parsons, D. B., M. A. Shapiro, R. M. Hardesty, R. J. Zamora, and J. M. Intrieri, 1991: The finescale structure of a west texas dryline. *Monthly weather review*, **119**, 1242–1258.

Pearson, G., F. Davies, and C. Collier, 2009: An analysis of the performance of the UFAM pulsed Doppler lidar for observing the boundary layer. *Journal of Atmospheric and Oceanic Technology*, **26**, 240–250, doi:10.1175/2008JTECHA1128.1.
URL http://journals.ametsoc.org/doi/abs/10.1175/2008JTECHA1128.1

Purser, R. J., W.-S. Wu, D. F. Parrish, and N. M. Roberts, 2003: Numerical Aspects of the Application of Recursive Filters to Variational

Statistical Analysis. Part I: Spatially Homogeneous and Isotropic Gaussian Covariances. *Monthly Weather Review*, **131**, 1524–1535, doi:10.1175//1520-0493(2003)131¡1524:NAOTAO¿2.0.CO;2.
URL http://journals.ametsoc.org/doi/abs/10.1175//1520-0493%282003%29131%3C1524%3ANAOTAO%3E2.0.CO%3B2

Rasmussen, E. N. and D. O. Blanchard, 1998: A Baseline Climatology of Sounding-Derived Supercell andTornado Forecast Parameters. *Weather and Forecasting*, **13**, 1148–1164, doi:10.1175/1520-0434(1998)013¡1148:ABCOSD¿2.0.CO;2.
URL http://journals.ametsoc.org/doi/full/10.1175/1520-0434(1998)013%3C1148:ABCOSD%3E2.0.CO%3B2

Ratnam, M. V., Y. D. Santhi, M. Rajeevan, and S. V. B. Rao, 2013: Diurnal variability of stability indices observed using radiosonde observations over a tropical station: Comparison with microwave radiometer measurements. *Atmospheric Research*, **124**, 21–33.

Rhodes, B. C., 2011: Pyephem: Astronomical ephemeris for python, 12014–.

Ritsche, M., 2008: Surface meteorological observation system (smos) handbook. Technical report, DOE Office of Science Atmospheric Radiation Measurement (ARM) Program (United States).

Rodgers, C. D., 2000: *Inverse Methods for Atmospheric Sounding*. WORLD SCIENTIFIC.
URL http://www.worldscientific.com/worldscibooks/10.1142/3171

Scott, D. W., 2015: *Multivariate Density Estimation: Theory, Practice, and Visualization*.

Segal, M. and R. Arritt, 1992: Nonclassical mesoscale circulations caused by surface sensible heat-flux gradients. *Bulletin of the American Meteorological Society*, **73**, 1593–1604.

Segal, M., R. Avissar, M. McCumber, and R. Pielke, 1988: Evaluation of vegetation effects on the generation and modification of mesoscale circulations. *Journal of the Atmospheric Sciences*, **45**, 2268–2293.

Shapiro, A., E. Fedorovich, and S. Rahimi, 2016: A Unified Theory for the Great Plains Nocturnal Low-Level Jet. *Journal of the Atmospheric Sciences*, **73**, doi:10.1175/JAS-D-15-0307.1.

Shaw, W. J., J. K. Lundquist, and S. J. Schreck, 2009: Research needs for wind resource characterization. *Bulletin of the American Meteorological Society*, **90**, 535–538, doi:10.1175/2008BAMS2729.1.
URL http://journals.ametsoc.org/doi/abs/10.1175/2008BAMS2729.1

Sisterson, D. L., R. A. Peppler, T. S. Cress, P. J. Lamb, and D. D. Turner, 2016: The ARM Southern Great Plains (SGP) Site. *Meteorological Monographs*, **57**, 1–6, doi:10.1175/AMSMONOGRAPHS-D-16-0004.1.
URL http://journals.ametsoc.org/doi/10.1175/AMSMONOGRAPHS-D-16-0004.1

Skamarock, W. C. and J. B. Klemp, 2008: A time-split nonhydrostatic atmospheric model for weather research and forecasting applications. *Journal of Computational Physics*, **227**, 3465–3485, doi:10.1016/j.jcp.2007.01.037.
URL http://www.sciencedirect.com/science/article/pii/S0021999107000459

Smith, W. and W. Feltz, 1999: The retrieval of planetary boundary layer structure using ground-based infrared spectral radiance measurements. ... *of Atmospheric and* ....
URL http://journals.ametsoc.org/doi/abs/10.1175/1520-0426(1999)016%3C0323%3ATROPBL%3E2.0.CO%3B2

Song, J., K. Liao, R. L. Coulter, and B. M. Lesht, 2005: Climatology of the Low-Level Jet at the Southern Great Plains Atmospheric Boundary Layer Experiments Site. *Journal of Applied Meteorology*, **44**, 1593–1606, doi:10.1175/JAM2294.1.
URL http://journals.ametsoc.org/doi/abs/10.1175/JAM2294.1

Sorbjan, Z., 1997: Decay of convective turbulence revisited. *Boundary-Layer Meteorology*, doi:10.1023/A:1000231524314.

Spencer, P. L. and J. Gao, 2004: Can Gradient Information Be Used to Improve Variational Objective Analysis? *Monthly Weather Review*, **132**, 2977–2994, doi:10.1175/MWR2833.1.
URL http://journals.ametsoc.org/doi/abs/10.1175/MWR2833.1

Spencer, P. L., D. J. Stensrud, and J. M. Fritsch, 2003: A Method for Improved Analyses of Scalars and Their Derivatives. *Monthly Weather Review*, **131**, 2555–2576, doi:10.1175/1520-0493(2003)131¡2555:AMFIAO¿2.0.CO;2.
URL http://journals.ametsoc.org/doi/abs/10.1175/1520-0493%282003%29131%3C2555%3AAMFIAO%3E2.0.CO%3B2

Spuler, S. M., K. S. Repasky, B. Morley, D. Moen, M. Hayman, and A. R. Nehrir, 2015: Field-deployable diode-laser-based differential absorption lidar (DIAL) for profiling water vapor. *Atmos. Meas. Tech*, **8**, 1073–1087, doi:10.5194/amt-8-1073-2015.
URL www.atmos-meas-tech.net/8/1073/2015/

Stull, R. B., 1988: *An Introduction to Boundary Layer Meteorology*. Springer Science & Business Media, 670 pp.
URL https://books.google.com/books?id=eRRz9RNvNOkC&pgis=1

Sun, W.-Y. and C.-C. Wu, 1992: Formation and diurnal variation of the dryline. *Journal of the atmospheric sciences*, **49**, 1606–1619.

Taylor, K. E., 2001: *Summarizing multiple aspects of model performance in a single diagram*, volume 106. 7183 pp.
URL http://rainbow.llnl.gov/publications/pdf/55.pdf

Thompson, G., P. R. Field, R. M. Rasmussen, and W. D. Hall, 2008: Explicit forecasts of winter precipitation using an improved bulk microphysics scheme. part ii: Implementation of a new snow parameterization. *Monthly Weather Review*, **136**, 5095–5115.

Thompson, G., R. M. Rasmussen, and K. Manning, 2004: Explicit forecasts of winter precipitation using an improved bulk microphysics scheme. part i: Description and sensitivity analysis. *Monthly Weather Review*, **132**, 519–542.

Thompson, R. L., R. Edwards, J. a. Hart, K. L. Elmore, and P. Markowski, 2003: Close Proximity Soundings within Supercell Environments Obtained from the Rapid Update Cycle. *Weather and Forecasting*, **18**, 1243–1261, doi:10.1175/1520-0434(2003)018¡1243:CPSWSE¿2.0.CO;2.
URL http://journals.ametsoc.org/doi/abs/10.1175/1520-0434(2003)018%3C1243:CPSWSE%3E2.0.CO%3B2

Thompson, R. L., B. T. Smith, J. S. Grams, A. R. Dean, and C. Broyles, 2012a: Convective Modes for Significant Severe Thunderstorms in the Contiguous United States. Part II: Supercell and QLCS Tornado Environments. *Weather and Forecasting*, **27**, 1136–1154, doi:10.1175/WAF-D-11-00116.1.
URL http://journals.ametsoc.org/doi/abs/10.1175/WAF-D-11-00116.1

— 2012b: Convective Modes for Significant Severe Thunderstorms in the Contiguous United States. Part II: Supercell and QLCS Tornado Environments. *Weather and Forecasting*, **27**, 1136–1154, doi:10.1175/WAF-D-11-00116.1.
URL http://journals.ametsoc.org/doi/abs/10.1175/WAF-D-11-00116.1

Tobin, D. C., F. a. Best, P. D. Brown, S. a. Clough, R. G. Dedecker, R. G. Ellingson, R. K. Garcia, H. B. Howell, R. O. Knuteson, E. J. Mlawer, H. E. Revercomb, J. F. Short, P. F. W. van Delst, and V. P. Walden, 1999: Downwelling spectral radiance observations at the SHEBA ice station: Water vapor continuum measurements from 17 to 26μm. *Journal of Geophysical*

Research, **104**, 2081, doi:10.1029/1998JD200057.
URL http://onlinelibrary.wiley.com/doi/10.1029/1998JD200057/full

Trapp, R. J., N. S. Diffenbaugh, H. E. Brooks, M. E. Baldwin, E. D. Robinson, and J. S. Pal, 2007: Changes in severe thunderstorm environment frequency during the 21st century caused by anthropogenically enhanced global radiative forcing. *Proceedings of the National Academy of Sciences*, **104**, 19719–19723, doi:10.1073/pnas.0705494104.
URL http://www.pnas.org/content/104/50/19719.abstract

Trier, S. B., C. a. Davis, D. a. Ahijevych, and K. W. Manning, 2014a: Use of the Parcel Buoyancy Minimum (B min) to Diagnose Simulated Thermodynamic Destabilization. Part I: Methodology and Case Studies of MCS Initiation Environments. *Monthly Weather Review*, **142**, 945–966, doi:10.1175/MWR-D-13-00272.1.
URL http://journals.ametsoc.org/doi/abs/10.1175/MWR-D-13-00272.1

Trier, S. B., C. A. Davis, D. A. Ahijevych, and K. W. Manning, 2014b: Use of the Parcel Buoyancy Minimum (B min) to Diagnose Simulated Thermodynamic Destabilization. Part II: Composite Analysis of Mature MCS Environments. *Monthly Weather Review*, **142**, 967–990, doi:10.1175/MWR-D-13-00273.1.
URL http://journals.ametsoc.org/doi/abs/10.1175/MWR-D-13-00273.1

Trier, S. B., G. S. Romine, D. A. Ahijevych, R. J. Trapp, R. S. Schumacher, M. C. Coniglio, and D. J. Stensrud, 2015: Mesoscale Thermodynamic Influences on Convection Initiation near a Surface Dryline in a Convection-Permitting Ensemble. *Monthly Weather Review*, **143**, 3726–3753, doi:10.1175/MWR-D-15-0133.1.
URL http://journals.ametsoc.org/doi/10.1175/MWR-D-15-0133.1

Turner, D., E. Mlawer, and H. Revercomb, 2016: Water vapor observations in the arm program. *Meteorological Monographs*, **57**, 13–1.

Turner, D. D., 2007: Improved ground-based liquid water path retrievals using a combined infrared and microwave approach. *Journal of Geophysical Research*, **112**, D15204, doi:10.1029/2007JD008530.
URL http://doi.wiley.com/10.1029/2007JD008530

Turner, D. D., R. A. Ferrare, L. A. Heilman Brasseur, W. F. Feltz, and T. P. Tooman, 2002: Automated retrievals of water vapor and aerosol profiles from an operational raman lidar. *Journal of Atmospheric and Oceanic Technology*, doi:10.1175/1520-0426(2002)019¡0037:AROWVA¿2.0.CO;2.

Turner, D. D. and J. E. Goldsmith, 1999: Twenty-four-hour Raman lidar water vapor measurements during the Atmospheric Radiation Measurement program's 1996 and 1997 water vapor intensive observation periods. *Journal of Atmospheric and Oceanic Technology*, doi:10.1175/1520-0426(1999)016¡1062:TFHRLW¿2.0.CO;2.

Turner, D. D. and U. Löhnert, 2014: Information content and uncertainties in thermodynamic profiles and liquid cloud properties retrieved from the ground-based Atmospheric Emitted Radiance Interferometer (AERI). *Journal of Applied Meteorology and Climatology*, **53**, 752–771, doi:10.1175/JAMC-D-13-0126.1.
URL `http://journals.ametsoc.org/doi/abs/10.1175/JAMC-D-13-0126.1`

Turner, D. D., E. J. Mlawer, G. Bianchini, M. P. Cadeddu, S. Crewell, J. S. Delamere, R. O. Knuteson, G. Maschwitz, M. Mlynczak, S. Paine, L. Palchetti, and D. C. Tobin, 2012: Ground-based high spectral resolution observations of the entire terrestrial spectrum under extremely dry conditions. *Geophysical Research Letters*, **39**, n/a–n/a, doi:10.1029/2012GL051542.
URL `http://doi.wiley.com/10.1029/2012GL051542`

Turner, D. D., D. C. Tobin, S. a. Clough, P. D. Brown, R. G. Ellingson, E. J. Mlawer, R. O. Knuteson, H. E. Revercomb, T. R. Shippert, W. L. Smith, and M. W. Shephard, 2004: The QME AERI LBLRTM: A Closure Experiment for Downwelling High Spectral Resolution Infrared Radiance. *Journal of the Atmospheric Sciences*, **61**, 2657–2675, doi:10.1175/JAS3300.1.
URL `http://journals.ametsoc.org/doi/abs/10.1175/jas3300.1`

Turner, D. D., V. Wulfmeyer, A. Behrendt, T. Bonin, A. Choukulkar, R. Newsom, W. Brewer, and D. Cook, 2018: Response of the land-atmosphere system over north-central oklahoma during the 2017 eclipse. *Geophysical Research Letters*, **45**, 1668–1675.

Vickers, D. and L. Mahrt, 1997: Quality control and flux sampling problems for tower and aircraft data. *Journal of Atmospheric and Oceanic Technology*, **14**, 512–526.

Vogelmann, A. M., A. M. Fridlind, T. Toto, S. Endo, W. Lin, J. Wang, S. Feng, Y. Zhang, D. D. Turner, Y. Liu, et al., 2015: Racoro continental boundary layer cloud investigations: 1. case study development and ensemble large-scale forcings. *Journal of Geophysical Research: Atmospheres*, **120**, 5962–5992.

Wagner, T. J., W. F. Feltz, and S. a. Ackerman, 2008: The Temporal Evolution of Convective Indices in Storm-Producing Environments. *Weather and Forecasting*, **23**, 786–794, doi:10.1175/2008WAF2007046.1.

URL http://journals.ametsoc.org/doi/abs/10.1175/2008WAF2007046.1

Wallace, J. M., 1975: Diurnal variations in precipitation and thunderstorm frequency over the conterminous united states. *Monthly Weather Review*, **103**, 406–419.

Wang, X., P. Guo, and X. Huang, 2011: A Review of Wind Power Forecasting Models. *Energy Procedia*, **12**, 770–778, doi:10.1016/j.egypro.2011.10.103.
URL http://linkinghub.elsevier.com/retrieve/pii/S1876610211019291

Webb, E. K., G. I. Pearman, and R. Leuning, 1980: Correction of flux measurements for density effects due to heat and water vapour transfer. *Quarterly Journal of the Royal Meteorological Society*, **106**, 85–100.

Weckwerth, T. M., K. J. Weber, D. D. Turner, and S. M. Spuler, 2016: Validation of a Water Vapor Micropulse Differential Absorption Lidar (DIAL). *Journal of Atmospheric and Oceanic Technology*, **33**, 2353–2372, doi:10.1175/JTECH-D-16-0119.1.
URL http://journals.ametsoc.org/doi/10.1175/JTECH-D-16-0119.1

Wetzel, S. W. and J. E. Martin, 2001: An operational ingredients-based methodology for forecasting midlatitude winter season precipitation. *Weather and forecasting*, **16**, 156–167.

Wingo, S. M., 2015: *Characterization of the Afternoon to Evening Transition of the Planetary Boundary Layer Over North Alabama and Implication for Convective Maintenance, Enhancement, and Initiation*. The University of Alabama in Huntsville.

Wingo, S. M. and K. R. Knupp, 2015: Multi-platform Observations Characterizing the Afternoon-to-Evening Transition of the Planetary Boundary Layer in Northern Alabama, USA. *Boundary-Layer Meteorology*, **155**, 29–53, doi:10.1007/s10546-014-9988-1.
URL http://link.springer.com/10.1007/s10546-014-9988-1

Xie, S., R. T. Cederwall, and M. Zhang, 2004: Developing long-term single-column model/cloud system–resolving model forcing data using numerical weather prediction products constrained by surface and top of the atmosphere observations. *Journal of Geophysical Research: Atmospheres*, **109**.

Xie, S., R. T. Cederwall, M. Zhang, and J. J. Yio, 2003: Comparison of scm and csrm forcing data derived from the ecmwf model and from objective analysis at the arm sgp site. *Journal of Geophysical Research: Atmospheres*, **108**.

Yan, H. and R. A. Anthes, 1988: The effect of variations in surface moisture on mesoscale circulation. *Monthly Weather Review*, **116**, 192–208.

Zhang, D. and R. A. Anthes, 1982: A high-resolution model of the planetary boundary layer—sensitivity tests and comparisons with sesame-79 data. *Journal of Applied Meteorology*, **21**, 1594–1609.

Zhang, M. and J. Lin, 1997: Constrained variational analysis of sounding data based on column-integrated budgets of mass, heat, moisture, and momentum: Approach and application to arm measurements. *Journal of the atmospheric sciences*, **54**, 1503–1524.

Zhang, M., J. Lin, R. Cederwall, J. Yio, and S. Xie, 2001: Objective analysis of arm iop data: Method and sensitivity. *Monthly Weather Review*, **129**, 295–311.

Zhang, M., R. C. Somerville, and S. Xie, 2016: The scm concept and creation of arm forcing datasets. *Meteorological Monographs*, **57**, 24–1.

Zhuojia, Y. and J. Xinyuan, 1995: Mesoscale vegetation-breeze circulations and their impact on boundary layer structures at night. *Advances in Atmospheric Sciences*, **12**, 29–46.

Ziegler, C. L., E. R. Mansell, J. M. Straka, D. R. MacGorman, and D. W. Burgess, 2010: The Impact of Spatial Variations of Low-Level Stability on the Life Cycle of a Simulated Supercell Storm. *Monthly Weather Review*, **138**, 1738–1766, doi:10.1175/2009MWR3010.1.

Appendix: Glossary

AERI Atmospheric Emitted Radiance Interfereometer. xi–xiv, xvii, xviii, 23, 33, 35, 36, 42, 52–63, 66, 67, 69, 70, 72–74, 79, 110–112, 115, 120, 122, 128, 133, 139, 143, 149, 150, 162, 168

AET Afternoon to Evening Transition. xi–xvi, xviii, xxi, xxii, 3, 4, 7–16, 18–20, 22, 23, 28, 30, 31, 39, 41, 60, 69, 75, 76, 78–80, 85–90, 92, 95, 96, 99–104, 108–110, 112, 113, 116, 117, 119, 120, 128–133, 135–137, 140, 149, 151, 153, 156, 157, 160–162, 165–168

ARM Atmospheric Radiation Measurement. xi–xiv, xviii–xx, 4, 18, 20, 22, 23, 25–31, 37–41, 45–48, 50, 51, 53, 71, 109–111, 113, 119, 121, 132, 135–138, 140, 142–145, 150–155, 157, 160, 162–164, 167, 168, 170

AT afternoon transition. xvii, 3, 4, 115

CAPE convective available potential energy. xi, xiv, xvii–xix, 12, 36, 53, 64, 66–70, 72, 110, 119–121, 125, 126, 130, 131, 134, 163, 167

CBL convective boundary layer. xx, 116, 118, 131, 155, 156, 160, 161, 164, 165, 170

CIN convective inhibition. xi, xiv, xviii, 12, 36, 66–68, 72, 120, 121, 130, 131, 134

DIAL differential absorption lidar. 36–38

DLID Doppler lidar. xvii, xviii, 23, 40, 41, 117, 122–124, 133, 139, 140, 143, 149, 150, 160, 162, 168

DNS direct numerical simulation. 46

EBBR energy balance Bowen Ratio system. 22, 23, 26, 28–31

ECMWF European Center for Mid-Range Forecasts. xix, 48–50, 151–155

ECOR eddy covariance system. 22, 23, 26, 28–31

ET evening transition. xii, xiv, xvii, xviii, 3, 4, 14, 28, 54, 59, 60, 109, 111–115, 119, 130, 133, 139

GCM global circulation model. 46

LASSO LES ARM Symbiotic Simulation and Observation. xi, xix, 46–51, 135, 137, 151–155, 157, 158, 160–162, 168

LBLRTM line-by-line radiative transfer model. 35, 36

LES large eddy simulation. 13, 45, 46, 135, 168

LFC level of free convection. 6

LWP liquid water path. 34, 35

MET surface meteorological. 26, 27, 51

MODIS Moderate Resolution Imaging Spectroradiometer. xv, xviii, 89, 138, 142

MSDA multi-scale data assimilation. xii, xix, 49–51, 151–155

MWR microwave radiometer. 23, 32, 34, 42

NDVI Normalized Difference Vegetation Index. xv, xviii, 89, 138, 142

NFOV narrow field of view. 38–40

NLLJ Nocturnal Low-Level Jet. 7–9

OE Optimal estimation. 43–45

PBL planetary boundary layer. 11, 40, 55, 140, 145, 162, 165

PWV precipitable water vapor. 34, 35

RLID Raman lidar. xiii, 23, 36–40, 55, 112

RTE radiative transfer equation. 31

SAM System for Atmospheric Modeling. xii, xix, 46–49, 153, 155, 159

SBL stable boundary layer. 165

SGP Southern Great Plains. xii, xiii, xviii, xix, xxi, 4, 11, 18, 20, 22, 23, 26, 28, 30, 31, 36, 37, 45, 46, 50–53, 69, 75, 88, 102, 109–111, 117–119, 130, 132, 135, 136, 138, 142, 152, 154, 160, 165, 167–169, 171

SRT sunset relative time. xvii, 115, 117, 119, 121, 129–132, 156, 161

STD 1-σ standard deviation. xi, xiii, 39, 40, 57, 58, 66–68

TSI Total Sky Imager. 30

VAD velocity azimuth display. 41, 149, 150

WFOV wide field of view. 38–40

WRF Weather Research and Forecasting. 46–50, 129, 161, 171

WWB Winter Wheat Belt. xii, xv, xvi, xviii–xx, 89–91, 95–98, 100–104, 107, 108, 112, 136–140, 142–145, 147, 152, 154, 160–164, 167–171